Measurement of $t\bar{t}$ Forward-backward Asymmetry in Large Hadron Collider

by

Lei Feng

A dissertation submitted to The Johns Hopkins University in conformity with the requirements for the degree of Doctor of Philosophy.

Baltimore, Maryland

January, 2018

Abstract

This thesis presents a measurement of Forward-Backward Asymmetry(A_{FB}) in $\mathrm{t\bar{t}}$ production. The data sample corresponds to $19.7\,\mathrm{fb}^{-1}$ of integrated luminosity in proton-proton collisions at $\sqrt{s} = 8\,\mathrm{TeV}$ collected by the CMS experiment at the LHC. Events selected contain a single isolated muon or electron and four or five jets among which two are b-tagged. A template technique is used to extract the asymmetry from the top quark kinematic distributions. This technique is based upon an extension of the tree-level cross section for $\mathrm{q\bar{q}}$ initial states that sensitively isolates $\mathrm{q\bar{q}}$ from gg/qg initial states. The measured A_{FB} and relative aboundance of $\mathrm{q\bar{q}}$ initiated $\mathrm{t\bar{t}}$ are measured and compared to both Standard Model predictions.

Primary Reader: Morris Swartz

Secondary Reader: Andrei Gritsan

Acknowledgments

First and foremost, I would like to thank my thesis advisor, Morris Swartz, for providing invaluable guidance and support during my years in graduate school. I learned a lot from him, not only about physics and statistics, but more importantly about how to conduct original research, and how to solve problems. I am very thankful that he has always respected and encouraged me to explore my area of interest, and has given me a lot of opportunities during the years to attend conferences, visit CERN and so much more. Morris is such an always been very approachable advisor, we end up having many great conversations over the years about life, travel, and many other things. He always have great stories to tell. I am very fortunate and honored to be his student.

Next, I would like to thank faculty members in JHU high energy physics group, especially Andrei, Petar and Barry, who give me many good suggestions during my PhD study.

I want to thank my current and former colleagues in high energy physics group, including Nick, Heshey, Alice, Yongjie, Marc, Kevin, Ian, Dave and Andrew. I am

grateful for all your advice, discussions and help. I want to especially thank my teammate Nick Eminizer, who has significant contributions to my thesis project. I also thank Mike Crosley for his early contribution in this project, whose code is still used in this analysis.

I want to thank administrative staff here in Physics Department of Hopkins, especially Kelley and Mark, who help me with many issues about teaching assistant, and travel related issues, making my study here smoothly.

I am lucky enough to know many wonderful friends during my years at Hopkins: Bingxiao, Wei, Yongjie, Mike, Yaofu, Forrest, Yu, Kui, Bin, Jon, to name a few. It is the friends here that make my six and half years in grad school a lifelong memory.

Finally, I want to thank my parents. Your limitless love, support and sacrifice make me who I am today. I am thankful to my wife, Candice, for her endless understanding, sacrifice, patience, and support in the past eleven years. Without her this thesis is impossible.

Dedication

This thesis is dedicated to Ethan Yicheng Feng

Contents

List of Tables

List of Figures

Introduction

Particle physics studies the elementary particles, the fundamental building blocks of the universe, and their interactions. Since the discovery of electron in the end of nineteenth century, with the advancement of experimental apparatus, more elementary particles have been discovered. Theories, from quantum mechanics to quantum field theory, have been developed along the way and now all known elementary particles and forces can be described by a beautiful and unified model called the Standard Model (SM) of particle physics. First proposed in 1960s, the SM has been proven very successful in describing ongoing experimental measurements, highlighted by the discovery of the predicted Higgs boson at the Large Hadron Collider (LHC) in 2011.

Before the discovery of the Higgs boson, the discovery and the ensuing study of another fundamental particle, the top quark, was of critical significance. First discovered in 1995 in the Tevatron collider at Fermilab, it is the heaviest elementary particle known to date, heavier than the Higgs boson. Due to its large mass, the top quark is suspected to be different from all other quarks, and to play a special role in electroweak symmetry breaking. In addition, the large mass of the top quark

indicates that it has a large Yukawa coupling to the Higgs boson, therefore top quarks also play an important role in Higgs boson production. For these reasons and many others, it is of great interest to study many properties of the top quark, and indeed the focus of this thesis is the study of one of the property of top quark pair production process.

Since 2011, the LHC has been running successfully, delivering a huge amount of particle collision data at the highest collision energy ever registered in human history, first at 7 and 8 TeV in 2011 and 2012, in the so called LHC Run-1, then at 13 TeV from 2015 until now at LHC Run-2. A proton-proton collider, LHC is a "top factory", producing many more $t\bar{t}$ events than were produced by the Tevatron. Using advanced detectors like the Compact Muon Solenoid (CMS), the properties of the top quark such as its mass and production cross sections have been measured with the highest accuracies to date.

This thesis presents a measurement of one of the properties of the top quark called the Forward-Backward Asymmetry (A_{FB}) of $t\bar{t}$ production. Pair production of top quarks and anti-quarks is the main source of top quarks in hadron colliders. There are two major production mechanisms for $t\bar{t}$ pairs, the first is via gluon-gluon (gg process) fusion and the second is via initial quark and anti-quark annihilation ($q\bar{q}$ process). If a reference direction is chosen as the direction of initial quark, then the $q\bar{q} \to t\bar{t}$ process is predicted to be forward-backward asymmetric in the $t\bar{t}$ center of mass frame. SM theoretical calculations predict that more top quarks are produced in the

forward hemisphere than in the backward hemisphere. Equivalently, this effect can be observed as an excess of top quarks over top anti-quarks in the forward hemisphere and is therefore also called the Charge Asymmetry in many literatures as well.

The $t\bar{t}$ Forward-Backward Asymmetry initially drew considerable attention in 2011 as the CDF and D0 experiments [4, 7] at the Tevatron reported observing significant deviations from the SM prediction [38, 39, 9]. This motivated considerable theoretical work to explain the anomaly with beyond standard model (BSM) physics. At the time of the writing of this thesis, improvements in the theoretical calculations and updated measurements using the full data sets recorded at Tevatron [8, 5, 6] have reconciled the anomaly. Regardless, as A_{FB} only originated from higher order perturbative calculation using SM, it provides a precise test of SM. In addition, it is sensitive to the interference of SM process with a heavy BSM resonance that is hard to detect directly. For these reasons, it is still of great scientific interest to measure this effect in LHC.

Measuring the top quark forward-backward asymmetry at the LHC is considerably more challenging than at the Tevatron. The $t\bar{t}$ cross section at the Tevatron is dominated by the $q\bar{q}$ process and the incident quark and anti-quark directions are reasonably well defined by the proton and antiproton beams. At the LHC, the production process is dominantly gg and the the quark content of the initial state is symmetric. Since there can be no asymmetry from the gg initial state, these two effects significantly complicate the extraction of the asymmetry in $q\bar{q} \to t\bar{t}$.

Measurements [2, 33, 3] done to date have focused on the determination of the so called charge asymmetry A_C that is based upon the number of positively and negatively charged leptons observed in top pair events at large lepton rapidity. This quantity is diluted by the symmetric gg initial states and uses only a fraction of the available information.

All of the measurements done to date have been "empirical" in the sense that the measured quantity does not depend upon a model of the $t\bar{t}$ production mechanism although the interpretation of the measurements is model dependent. This thesis introduces a different approach. A simplified model for the production mechanism is adopted. This allows the use of a likelihood analysis to isolate the $q\bar{q}$ subprocess from the gg and qg subprocesses and from other backgrounds. The adopted model is a leading order description of several possible BSM processes and is a reasonable approximation of the expected NLO QCD effects.

Using the template fit method described in this thesis, a measurement of the inclusive A_{FB} in $t\bar{t}$ production using semileptonic $t\bar{t}$ events produced at the LHC is performed and described in the thesis. The full 8 TeV data recorded by the CMS Experiment is analyzed.

This thesis is organized as follows:

Chapter 1 and 2 give an overview of the theoretical and phenomenological foundation of SM, cross sections and top quark physics.

Chapter 3 introduces the experimental apparatus , including the LHC and the

sub detectors of CMS.

Chapter 5 describes the signal and background process modeling and the data sample analyzed in this thesis. An overview of Monte-Carlo (MC) simulation procedure is given first, then the specific processes and the technical set up for the MC is listed.

Chapter 4 first describes the physical objects reconstruction algorithms used in CMS and this thesis. Then, the signal event selection and the result of the selection is discussed.

Finally, Chapter 6 contains the details of the A_{FB} measurements, which is the focus of this thesis and the original work of the author of this thesis as part of the team.

Chapter 1

Theoretical Background

In this chapter, I will give a brief overview of the Standard Model (SM) of particle physics and the technical methods used to calculate experimental observables using Quantum Field Theory (QFT). First, an overview of the particle content and the interactions of the Standard Model is introduced. Then the theoretical formalism of QFT is briefly reviewed: the experimental and physical meaning of decay rates and cross sections; the connection between scattering amplitudes and cross sections; and Lagrangian densities and gauge invariance. Finally, the formalism of perturbative calculation and the Feynman Calculus is introduced. This chapter provide the context for all the discussions in following chapters.

Due to the technical complexity of this topic, I will give only important results and recipes without providing proofs or derivations. More detailed descriptions of this topic can be found in [45, 44, 31]

1.1 Standard Model

The Standard Model (SM) of particle physics is a description of nature built upon quantum field theory (QFT) and the principle of gauge symmetry that explains the fundamental building blocks of matter and their interactions. It has been proven extremely successful in explaining all observed experimental data. It has also made a number of predictions including the unseen W and Z bosons which were discovered in 1983. We will briefly summarize the particle content and the interactions of the SM, as a particle physicist's view of the universe.

Using the language of QFT, both matter and interactions are fields which are continuous in space and time, and elementary particles are the quanta of the corresponding fields. Particles are point-like, structureless objects that are fully described by their masses, spins, and various charges. The strengths of their interactions depend on the values of their charges. They are not static, but dynamic in nature, meaning that they can change into other particles, or be produced in matter-antimatter pairs from vacuum, or annihilate with their anti-partners. All these processes are described in the language of interaction vertices, where momentum, charge, spins, and some other quantities are conserved.

In the SM, the fundamental building blocks of matter are fermions, which are spin 1/2 particles. They are further divided into two groups, leptons and quarks. Both leptons and quarks are divided into three generations where each generation is similar in every way except for the masses of its members. Leptons include electrons, muons,

taus and three corresponding neutrinos of the same flavor. Charged leptons carry electric charge Q=-1, whereas their corresponding neutrinos are neutral particles. The six quarks are also categorized into the three generations, the up (u) and down (d) quarks, the charm (c) and strange (s) quarks, top (t) and bottom (b) quarks. All up-type quarks (u,c,t) carry charge $Q = +2/3$, all bottom type quarks (d,s,b) carry charge $Q = -1/3$.

There are four fundamental forces in nature: the electromagnetic (EM) force which binds electrons and nuclei together; the weak force which is responsible for the beta decay of neutrons to protons; the strong force which binds quarks together to form protons and neutrons; and finally the gravitational force. Among these forces, the SM provides a theoretical frame work in which three of the four forces, EM, weak and strong interactions emerge naturally from the requirement of local gauge symmetry of the Lagrangian.

Fig.1.1 shows the fundamental particles, arranged according to the forces that they experience as well as their generation among the three generations of fermions. It also shows their quantum numbers and experimentally measured masses.

Electromagnetic interactions are the most common interactions in our everyday life. All electrically charged particles like leptons, quarks, and W/Z bosons can interact electromagnetically. It is achieved by an exchange force carrier, the photon, which is massless and electric charge neutral. Because the photon is massless, according to QFT, the range of EM force is infinite. Fig.? shows a typical interaction vertex for

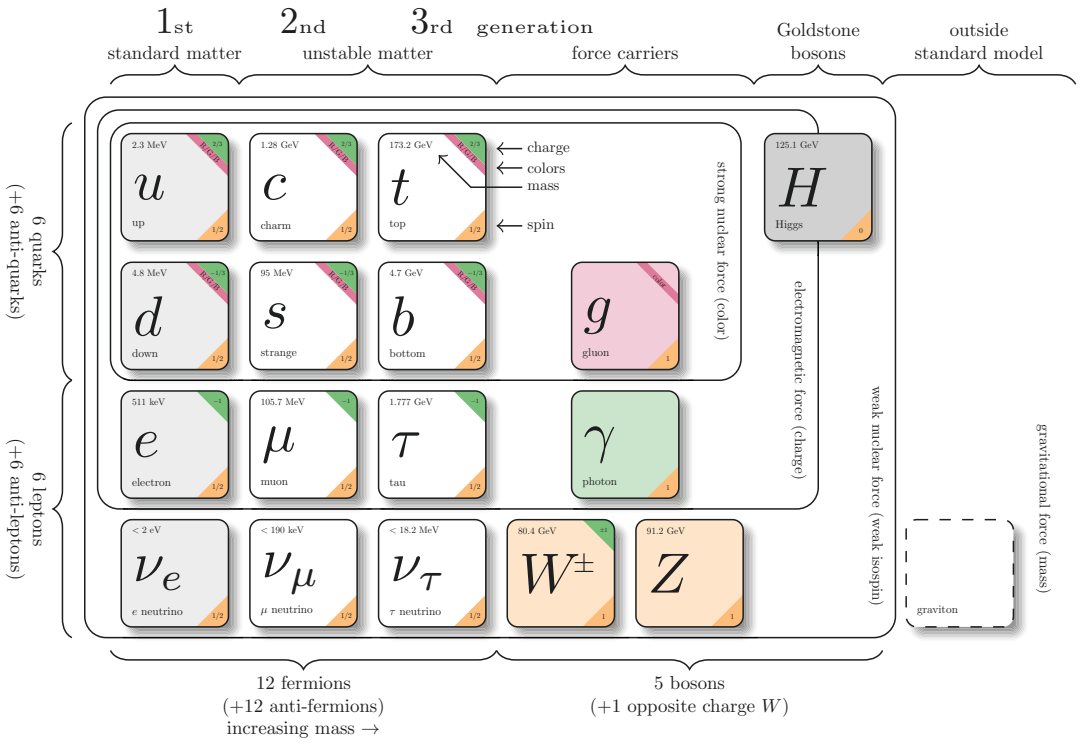

Figure 1.1: The table of all elementary particles discovered to date and their relationships in SM. [26]

EM interactions. The strength of the EM interaction is characterized by the fine structure constant $\alpha_{EM} = \frac{e^2}{4\pi} = 1/137$

The weak interaction applies to all elementary particles that carry weak charges such as leptons, quarks, and W/Z bosons. It is the underlying mechanism that enables the radiative decay of sub-atomic particles, by inducing flavor changing processes. For example, an up-type quark can become a down-type quark via weak interaction, which is the process behind beta decay.

The force carriers of the weak interaction are the electric charged W^+/W^- bosons of mass 80 GeV and the electric charge neutral Z boson of mass 91 GeV. At energy scales much less than the W mass, the large mass of the force carrier suppresses the strength of the weak interaction such that it is about 3 to 4 orders of magnitude smaller than the strength of the EM interaction and hence "weak". At energy scales comparable to masses of the W/Z bosons, which in quantum mechanics is equivalent to very short distances (10^{-18} m), it becomes comparable in strength to the EM interaction.

The weak interaction is the only interaction that mediates flavor changing processes (via the coupling to the charged W bosons). An up-type quark can change to a down-type quark, and an electron can change to a neutrino. The flavor changing coupling can happen both in the same generation and across generations. For example, a u quark can become a d or s quark via coupling to the W^+, although it is more likely to become a d quark. In the SM, the coupling strength between different flavors of quarks is described by Cabibo-Kobayashi-Maskawa (CKM), which is a 3 by 3 unitary matrix, each element of the matrix shows the coupling strength between up and down-type quarks, as shown below.

$$CKM = \begin{bmatrix} V_{ud} & V_{us} & V_{ub} \\ V_{cd} & V_{cs} & V_{cb} \\ V_{td} & V_{ts} & V_{tb} \end{bmatrix}$$

The current measured magnitudes of CKM elements are given below [ref], and we

give only the rough central value for illustrative purposes:

$$|CKM| = \begin{bmatrix} 0.97 & 0.22 & 0.003 \\ 0.22 & 0.97 & 0.04 \\ 0.008 & 0.04 & 0.9991 \end{bmatrix}$$

In the CKM matrix, the diagonal elements represent the coupling between quarks in the same generation, while the off-diagonal terms represent the flavor changing couplings between different generations. Notice that the diagonal elements are close to one, and off-diagonal elements are negligible/small between first/second and third generation quarks. This indicate top quark couples almost exclusively to the bottom quark, which is a signature of top quark decay.

Finally, the strong force acts between any particles that are color charged, namely quarks and gluons. It is mediated by massless, spin 1 gauge bosons called gluons. The strong interaction is described by a gauge theory called Quantum Chromodynamics (QCD). In QCD, there are three fields associated with each flavor of quark and we label them with different colors: red, green, blue. The names of the colors are just conventional and have nothing to do with actual colors. The theory of QCD is invariant under local SU(3) gauge transformations on the quark fields. The gauge invariance introduces a 3×3 matrix gauge field, corresponds to eight gluons, each one is associated with a color and an anti-color.

One unique property of QCD is called asymptotic freedom, which states that at sufficiently high energy, the strong interaction is no longer strong, and quarks

and gluons behave like free particles, just like leptons or photons. Another related phenomena of QCD is called quark confinement: quarks and gluons cannot exist as isolated, free particles, so called "bare" states. Both asymptotic freedom and quark confinement share the same origin, namely the running coupling constant. Because of QCD is a SU(3) gauge theory, the coupling constant of strong interaction α_s, which reflects the strength of strong interaction, increases when the exchanged momentum at interacting vertex decreases.

1.2 Decay rates and cross sections

In scattering experiments where two beams of particles collide with each other, the cross section, denoted by σ, is a quantity that characterizes the intrinsic underlying interactions of the colliding particles independently of the beam intensities.

Roughly speaking, the cross section describes the probability of observing a particular process. It has the dimensions of area, and an intuitive interpretation of cross section is that it is the area of the target particle presented to an incoming point-like beam particle in a fixed target scattering experiment.

The number of events of a process observed during a time period, can be calculated in the following way:

$$N_{\text{exp}} = \sigma_{\text{exp}} \times \int \mathcal{L}(t)dt \tag{1.1}$$

Where $\mathcal{L}(t)$ is instantaneous luminosity, which measures the intensity of colliding

beams. In the LHC, where both beams include bunches of colliding particles the instantaneous luminosity can be expressed as

$$\mathcal{L} = f_{\text{coll}} \frac{n^2}{4\pi\sigma_x\sigma_y} \tag{1.2}$$

where each bunch contains n particles, the RMS horizontal and vertical sizes of the beams are σ_x and σ_y, and each bunch is collided with frequency f_{coll}. It is common to use another quantity, integrated luminosity, $\mathcal{L}_{\text{int}} = \int \mathcal{L}(t)dt$, which represents the total number of collisions done over time, and is usually measured in the units of pb^{-1} or fb^{-1} where b is an abbreviation for barn which is defined as $10^{-28}m^2$.

It is often interesting to know not just the total number of observed events of a process, which is given by $\mathcal{L}_{\text{int}}\sigma_{\text{exp}}$, but also the distribution of the events in final state variables. To do this, we also introduce another observable, called the differential cross section usually denoted by $d\sigma$. In the special case of a two particle collision with a two particle final state (the $2 \to 2$ process), a type of differential cross section of particular interest is the angular one:

$$\mathcal{L}_{\text{int}} \frac{\text{d}\sigma}{\text{d}\Omega} = \frac{\text{d}N}{\text{d}\Omega} \tag{1.3}$$

where $\text{d}\Omega = \sin\theta \text{d}\theta\text{d}\phi$ is the solid angle of one of the outgoing final state particles. In another words, $\text{d}\sigma/\text{d}\Omega$ is the angular distribution of the final state particle.

There are two types of cross section, the inclusive (total) and exclusive ones. Inclusive means the total cross section regardless of the specific final states (some times are called channels) that are observed. Exclusive ones are the cross section of

observing a specific channel. So by definition, $\sigma_{\text{tot}} = \sum_i^n \sigma_i$.

Another observable commonly used in particle physics is the decay rate of an unstable particle, denoted by Γ, which represents the probability per unit time that the particle will decay into final states of 2 or more daughter particles. Assuming that the initial number of particles is N(0), the number of remaining particles after time t is:

$$\mathrm{N}(t) = \mathrm{N}(0) \exp^{-\Gamma t} \tag{1.4}$$

For a particle that can decay to many different decay modes, the total decay rate is the sum of the rates for all decay modes:

$$\Gamma_{tot} = \sum_{i=1}^{n} \Gamma_i \tag{1.5}$$

And the branching ratio of decay mode is defined simply as $\mathrm{Br}_i = \Gamma_i / \Gamma_{tot}$. The branching ratio is another observable that can be measured experimentally.

In scattering experiments, if the initial particles can form an intermediate bound state, then the cross section near the mass of the bound state exhibits an enhancement known as a resonance. The cross section will have a peak of the form described by Breit-Wigner formula

$$\sigma \propto \frac{1}{(E - E_0)^2 + \Gamma^2/4} \tag{1.6}$$

where the width of the resonance Γ is also the decay rate of the unstable resonance.

1.3 Lagrangian Density and Gauge Invariance

In Quantum Field Theory, both the equations of motion and the interactions between particles can be fully described by choosing a Largrangian density function (simply denoted by Lagrangian), $\mathcal{L}$.

The Lagrangian is a function of fields ($\phi(x^\mu)$) and their space time derivatives ($\partial_\mu \phi$). The fields are themselves continuous functions of space and time, $x^\mu = (t, x_1, x_2, x_3)$, which explicitly puts space and time on an equal footing as required by special relativity.

All elementary particles are the quanta of the underlying fields. Depending on the spin of the particle, different types of fields satisfy different equations of motion. Scalar fields are associated with spin-0 particles (Higgs boson in SM), denoted by ϕ. Spinor fields are associated with spin-1/2 particles (fermions, such as leptons or quarks), denoted by ψ. Vector fields are associated with spin-1 particles (all gauge bosons, such as photon or gluons), denoted by A^μ. The forms of Lagrangian in QFT is almost the same as classical field theory, the difference is that in QFT, the fields incorporate creation and annihilation operators.

The equations of motion for free fields can be derived by using the principle of least action, which states that the motion of free particles between two space-time points x_1^μ, x_2^μ,must follow the path of least action. Action is defined as the space-time

integral:

$$S = \int \mathcal{L}(\phi, \partial_\mu \phi) \mathrm{d}^4 x \tag{1.7}$$

The path of least action is equivalent to the condition $\delta S = 0$ which leads to the Euler-Lagrange equation of motion for the field,

$$\partial_\mu \left(\frac{\partial \mathcal{L}}{\partial(\partial_\mu \phi)} \right) - \frac{\mathcal{L}}{\partial \phi} = 0 \tag{1.8}$$

QFT is a local theory, which means it only has a localized Lagrangian density, where all interactions among fields happen at the a point in space-time. The interaction terms of matter fields and gauge boson fields in the Standard Model are introduced as a consequence of enforcing non-abelian local gauge invariance, which was first proposed by Yang and Mills in 1950s.

For example, electromagnetic interactions can be introduced by enforcing local U(1) abelian gauge invariance on the Lagrangian density. Starting from the Lagrangian of free fermion field:

$$\mathcal{L} = i\bar{\psi}\partial_\mu \gamma^\mu \psi - m\bar{\psi}\psi \tag{1.9}$$

where ψ is the spinor field, and γ^μ are 4×4 matrices. This Lagrangian is invariant only under global U(1) transformation $\psi \to \exp^{i\theta} \psi$. In order to promote the global U(1) transformation to local ones, where $\psi \to \exp^{i\theta(x)} \psi$, the derivative ∂_μ need to be replaced by a specially designed covariant derivative:

$$\mathcal{D}_\mu = \partial_\mu + iqA_\mu \tag{1.10}$$

such that under the local gauge transformation $\psi \rightarrow \exp^{-iq\lambda(x)}$, the newly introduced vector field A_μ transforms according to :

$$A_\mu \rightarrow A_\mu + \partial_\mu \lambda \tag{1.11}$$

Then the following Lagrangian will become invariant under local gauge transformations:

$$\mathcal{L} = i\bar{\psi}\mathcal{D}_\mu \gamma^\mu \psi - m\bar{\psi}\psi \tag{1.12}$$

Expanding the above Lagrangian:

$$\mathcal{L} = [i\bar{\psi}\partial_\mu \gamma^\mu \psi - m\bar{\psi}\psi] - (q\bar{\psi}\gamma^\mu \psi)A_\mu \tag{1.13}$$

We find that the coupling of matter field ψ with the gauge boson field A_μ, the quantization of which is photons, naturally emerge from the term $(q\bar{\psi}\gamma^\mu\psi)A_\mu$ where q is the electric charge.

The same procedure can be expanded to describe the unified electro-weak interaction, by enforcing $\mathrm{SU}(2)_L \otimes \mathrm{U}(1)$ local gauge invariance. The gauge bosons introduced in the covariant derivatives are W^+W^-,Z and photon. Eight gluons are introduced by enforcing the invariance of SU(3) color group transformations.

1.4 From Matrix Element to Cross Sections

To relate the dynamics described by Lagrangian to the experimentally observable cross section, we need to first introduce the concept of S-matrix S and its matrix element $\mathcal{M}$.

The S-matrix is a unitary operator that relates the incoming particle states (initial states) and the outgoing final states of a scattering experiment. We define the initial two particle state as $|\boldsymbol{k}_A\boldsymbol{k}_B\rangle_{in}$, and outgoing many particle final state as $|\boldsymbol{p}_1\boldsymbol{p}_2\rangle_{out}$, where $\boldsymbol{k}$ and $\boldsymbol{p}$ are 4-momentum of initial and final states. The cross section is proportional to the transition probability from incoming state to outgoing state, which can be calculated according to quantum mechanics as follows:

$$P = |_{\text{out}}\langle \boldsymbol{p}_1\boldsymbol{p}_2\cdots|\boldsymbol{k}_A\boldsymbol{k}_B\rangle_{\text{in}}|^2 \tag{1.14}$$

S matrix is defined as an operator that contains all the information about time evolution and interaction between initial and final states:

$$_{\text{out}}\langle \boldsymbol{p}_1\boldsymbol{p}_2\cdots|\boldsymbol{k}_A\boldsymbol{k}_B\rangle_{\text{in}} \equiv \langle \boldsymbol{p}_1\boldsymbol{p}_2\cdots| S |\boldsymbol{k}_A\boldsymbol{k}_B\rangle \tag{1.15}$$

Since the scattering process can be separated into the overlapping (interacting) and non-overlapping parts of two particles, it can be written as $S = 1 + iT$. And matrix element $\mathcal{M}$ can be defined to contain only the information of interaction, separate from all the kinematics, such as conservation of momentum:

$$\langle \boldsymbol{p}_1\boldsymbol{p}_2\cdots| iT |\boldsymbol{k}_A\boldsymbol{k}_B\rangle = (2\pi)^4\delta^(4)(\boldsymbol{k}_A + \boldsymbol{k}_B - \sum \pm p_f)i\mathcal{M}(\pm k_A, \pm k_B \to \boldsymbol{p}_f) \tag{1.16}$$

The matrix element can be calculated using perturbation theory based on the Lagrangian by using a set of rules called the Feynman calculus. The cross section is related to matrix element. In the simplest case of $2 \to 2$ scattering, the differential cross section in center of mass frame can be calculated with the following form:

$$\left(\frac{\mathrm{d}\sigma}{\mathrm{d}\Omega}\right)_{CM} = \frac{1}{2E_A 2E_B|v_A - v_B|}\frac{|\boldsymbol{p}_1|}{(2\pi)^2 4E_{cm}}|\mathcal{M}(p_A, p_B \to p_1, p_2)|^2 \tag{1.17}$$

1.5 Feynman Calculus and Perturbation Theory

As described in previous section, the observed cross section is related to the matrix element $\mathcal{M}$. It can be calculated perturbatively in terms of the order of the coupling constant, usually denoted by α, by following the Feynman rules which are derived from the Lagrangian of the theory.

The building blocks of this formalism, the Feynman Calculus, are the Feynman Rules, which describe the propagation of free fields and their interactions at vertices. An example of QED Feynman rules are given below in Fig.1.2,1.3

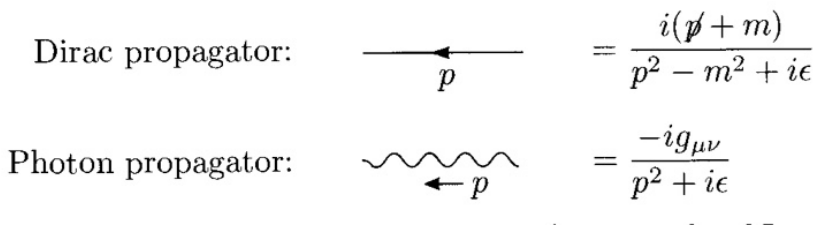

Figure 1.2: The Feynman diagram of fermion and photon propagator. [45]

It can be shown that the scattering matrix element $i\mathcal{M}$ can be calculated by summing over all connected Feynman diagrams evaluated according the Feynman rules. In the calculation of each diagram, momentum conservation is imposed at all vertices, and if there is loop in the diagram, the undetermined momentum in the loop must be integrated out.

Figure 1.3: The Feynman diagram of QED vertex, represent the electromagnetic interaction by exchanging a photon. [45]

The matrix element can be calculated perturbatively, order by order, in terms of the power of interaction coefficient. In QED, the order is represented by the power of fine structure constant defined as $\alpha_{\mathrm{EM}} = e^2/4\pi \approx 1/137$. The rationale of this approach follows from the small size of the coupling constant, which implies that the contribution of each higher order in the calculation is significantly smaller than that of the previous order.

We call the leading order (LO) diagrams the ones containing the lowest power of α_{EM} of all connected diagrams. LO diagrams are also often called tree-level diagrams. One example of an LO diagram and its corresponding matrix element, for the scattering of two fermions is shown below in Fig.[1.4]

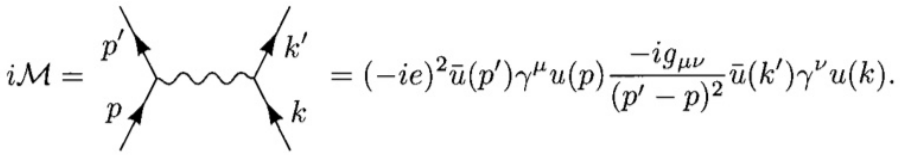

Figure 1.4: The Feynman diagram of LO scattering of two fermions. [45]

In the Feynman diagram shown in Fig.1.4, the arrows label the direction of momentum flow for the matter fields (the direction of anti-matter momentum is the reverse of the arrow). The momenta of the initial and final states are labeled as p, k and p', k'. The matrix element corresponds to this diagram can be seen as following from the individual Feynman rules mentioned above.

1.6 Higher Order Corrections and Renormalization

In higher order diagrams containing loops, the undetermined momentum in the intermediate virtual process (loop) must be integrated over all values. These integrals often become infinite as the momentum in the loop goes to infinity. One example of loop diagram of the same process of fermion scattering is shown below in Fig.1.5, which is called the vacuum polarization correction, where the virtual photon splits into a fermion/anti-fermion pair. It can be shown that this diagram is divergent as $\ln q$ where q is the momentum transfer that is carried by photon.

In order to make the matrix element from this diagram finite, a special procedure called Renormalization is applied. This procedure involves a redefinition of the coupling constant to absorb the divergent terms, and the new coupling constant that actually depends on the momentum transfer q. This is called running coupling constant, and is given in Eq.1.18 for the case of vacuum polarization correction below:

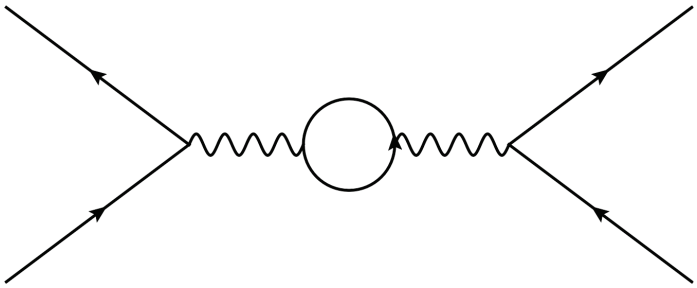

Figure 1.5: The Feynman diagram of loop correction of femion scattering.

$$\alpha(q^2) = \alpha(0)\left[1 + \frac{\alpha(0)}{3\pi} f(\frac{-q^2}{m^2})\right] \tag{1.18}$$

where $f(x)$ $\ln x$, and $q^2 < 0$ for the momentum being exchanged. The coupling constant increases at larger momentum scales, which is equivalent to smaller distances of the interaction. In another words, the effective charge of the observed particle changes with the distance being probed.

The higher order corrections to the LO calculation together with renormalization procedure, introduce a momentum scale called renormalization scale μ_R. Calculations including higher-order contributions to the matrix element are usually functions of this scale through their dependence on renormalized quantities, such as coupling constants. In practice the renormalization scale is usually chosen as the typical momentum transfer of the process, Q, or the invariant mass of the produced final state particles.

In contrast to QED, the running coupling constant of QCD, $\alpha_s\mu_R$ decreases as exchanged momentum increases. So in sufficiently high energy regimes, perturba-

tion calculations can provide accurate predictions of scattering processes involving the strong interaction, while at lower energy scales non-perturbative effects are quite important. Because the strong interaction becomes strong at the scales of hadron masses, no bare quark and gluons can be observed directly; they are observed experimentally as highly collimated group of hadrons, called "jets".

This completes our brief review of the Standard Model. The next chapter focuses on the specific phenomenology of top quark physics, which is the main topic of this thesis.

Chapter 2

Top physics Phenomenology at the LHC

In the Standard Model of particle physics, top quark is the up-type quark in the third generation of fermions. It has spin 1/2, electric charge $Q = 2/3$ and forms a weak isospin doublet with the bottom quark. It is also charged under the SU(3) group, being a color triplet with three colors.

As a result, top quark is affected by all three SM forces: the electromagnetic force, the weak force and the strong force. It couples to the respective gauge bosons via the following vertices described in Fig. 2.1-Fig. 2.4 .

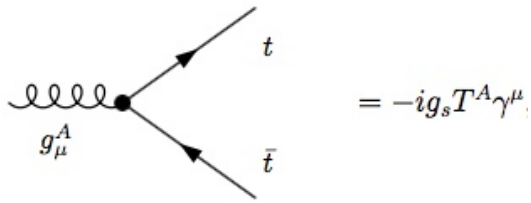

Figure 2.1: Top quark coupling to gluon via strong interaction.[47]

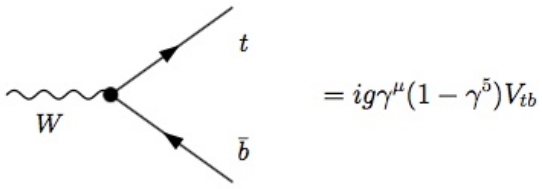

Figure 2.2: Top quark coupling to W boson and bottom quark via weak interaction.[47]

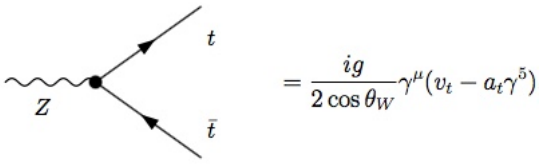

Figure 2.3: Top quark coupling to Z boson, via weak interaction.[47]

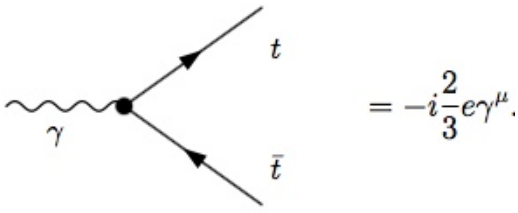

Figure 2.4: Top quark coupling to photon via electromagnetic interaction.[47]

Top quark is special among all known six quarks due to its large mass. First discovered at the Fermilab Tevatron collider in 1995, it has a mass that is presently measured to be about 173 GeV, almost as heavy as tungsten atom. It is the only fundamental fermion that is heavier than W boson, which has a mass of about 80 GeV. Due to the large mass difference between top quark and W boson, the phase space for top decay is very large, causing the top quark to decay before being able to form any hadronic bound state. This provide an opportunity for the careful study of QCD as the top quark can be treated as a quasi-free quark during the production and decay processes.

Another reason for the importance of top quark physics is due to the large coupling of top quarks and the newly discovered Higgs boson. As the Yukawa coupling between fermions and Higgs bosons is proportional to the mass of fermion, the top quark has the largest coupling to the Higgs boson. The production of Higgs bosons at the LHC often involves $t\bar{t}H$ coupling, in both the dominant production mechanism of gluon-gluon fusion process and in the associated production of Higgs and $t\bar{t}$ shown in Fig. 2.5. Therefore the study of top quark mass and its coupling to the Higgs are critical in testing the validity of Higgs mechanism, which is thought be be responsible for origin of mass via spontaneous symmetry breaking.

The Large Hadron Collider, which combines a much higher center of mass energy and a much higher luminosity than the Tevatron, is indeed a top factory, opening the door to more precise measurements of the properties of top quarks.

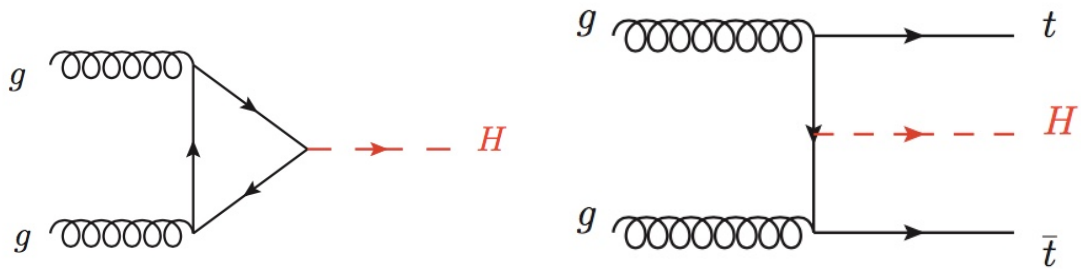

Figure 2.5: Major higgs production mechanism in LHC, via gluon gluon fusion (left) or associated production of $t\bar{t}$ and Higgs (right).[47]

Many properties of top quark have been carefully studied at the LHC, including the mass of top quark, the cross section of top anti-top pair production, and the spin correlations of top anti-top pair production. A good summary of techniques and latest results of top property measurements can be found in the literature [32, 37].

Of many properties of top quark, in this thesis we exclusively focus on one particular property of top pair production, namely the "Forward-Backward Asymmetry" (A_{FB}). It is the spatial asymmetry of top quark pair production with respect to the direction of incoming initial quark, as shown in Fig. 2.6. At parton level it is defined as:

$$A_{\mathrm{FB}} = \frac{N_{t\bar{t}}(c* > 0) - N_{t\bar{t}}(c* < 0)}{N_{t\bar{t}}(c* > 0) + N_{t\bar{t}}(c* < 0)} \tag{2.1}$$

where $c* \equiv \cos(\theta*)$ and $\theta*$ is the production angle of top quark in $t\bar{t}$ center of mass frame. This quantity is interesting because according to the SM, A_{FB} is zero at LO of in perturbative QCD calculation, and becomes non-zero from NLO contributions.

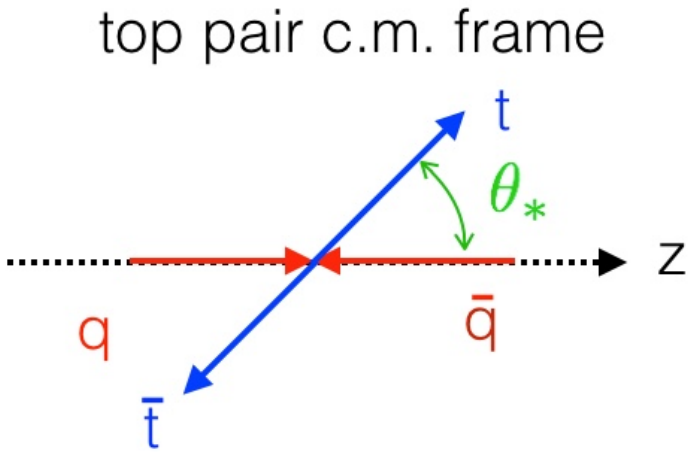

Figure 2.6: Geometric definition of $t\bar{t}$ production angle. Assuming zero $t\bar{t}$ system transverse momentum, in their center of mass frame, both $t\bar{t}$ and $q\bar{q}$ are back to back. The top production angle is defined as the polar angle between the direction of top quark and direction of initial quark, shown in the Figure.

A good measurement of A_{FB} provides a precision test of the SM and is sensitive to contributions from possible non Standard Model contributions.

2.1 Top Quark Pair Production

2.1.1 Leading Order

In hadron colliders, top anti-top pairs are mostly produced via strong interactions. In the leading order of perturbative QCD (order of α_s^2), there are two production

mechanisms. The first one is via quark anti-quark annihilation, which we denote as $q\bar{q}$ initiated top pair production. (we use $q\bar{q}$ process for simplicity sometime in the later chapters of this thesis). The Feynman diagram of this process is shown in Fig.?. The differential cross section is,

$$\frac{d\sigma}{dc_*}(q\bar{q}; M^2) = \frac{\pi\alpha_s^2}{9M^2}\beta\left[1 + \beta^2 c_*^2 + \left(1 - \beta^2\right)\right] \tag{2.2}$$

where: M is the invariant mass of $t\bar{t}$ pair, $\beta = \sqrt{1 - 4m_t^2/M^2}$ is the top quark velocity in the t$\bar{\text{t}}$ center of mass (cm) frame, θ^* is the production angle between the initial state quark direction and the top quark direction in the $t\bar{t}$ cm frame, $c_* \equiv \cos\theta^*$, and $\alpha_s \equiv g_s^2/4\pi$ is the strong interaction strength constant which is about 0.12 at the scale of Z boson mass.

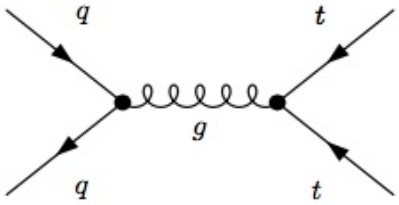

Figure 2.7: Feynman diagram for leading order parton level $q\bar{q} \to t\bar{t}$ process via strong interaction.[47]

The second process of top pair production combines the s, t, u channels of the gluon-gluon initiated process (simply denoted as gg process in this thesis), as described by the Feynman diagram in Fig. 2.8. The parton level differential cross section of this process in LO reads:

$$\frac{d\sigma}{dc_*}(gg; M^2) = \frac{\pi\alpha_s^2}{48M^2}\beta\left[\frac{16}{1-\beta^2c_*^2} - 9\right]\left\{\frac{1+\beta^2c_*^2}{2} + (1-\beta^2) - \frac{(1-\beta^2)^2}{1-\beta^2c_*^2}\right\} \quad (2.3)$$

The t and u channel dominated gg process has a distribution that is more peaked in the forward and backward directions, i.e. more likely in the phase space with higher $c*$, compare with $q\bar{q}$ process. This feature is crucial to motivate our template fit based measurement that is described in Chapter.6.1, which relies on the discrimination of the $q\bar{q}$ and gg production mechanisms.

Note that according to Eq.2.2, the LO calculation of the $q\bar{q} \to t\bar{t}$ process does not produce a non-zero A_{FB}, as the differential cross section is even in $c*$. The same is true for the LO calculation of $gg \to t\bar{t}$

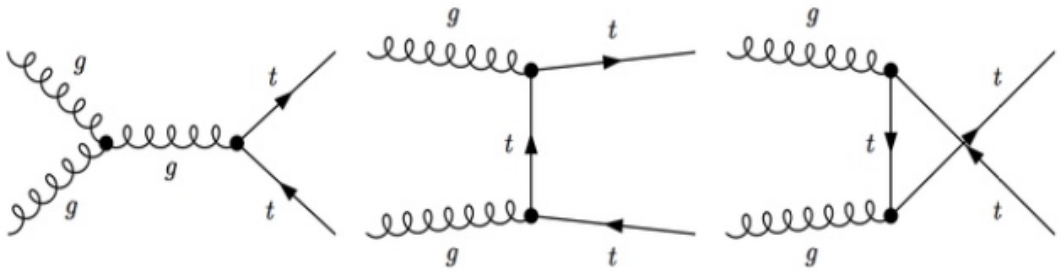

Figure 2.8: Feynman diagram for leading order parton level $gg \to t\bar{t}$ process via strong interaction. The s,t,u channels are shown in left,middle,right figures respectively.[47]

2.1.2 Next to Leading Order Corrections

The higher order corrections to top pair production are important due to the sizable value of strong interaction coefficient $\alpha_s \sim 0.1$ at the energy scale of this process. As the energy scale of top pair production is set by the large mass of top quark (173 GeV) the perturbative QCD calculation is able to give accurate predictions.

Currently, Next-to-Leading-Order calculations are regarded as the standard for event generation and simulation of top-quark production by the LHC experiments. These are implemented in several event generators. The generators used in this thesis are POWHEG-BOX[10] and aMC@NLO[11]. The impact of the NLO contributions to the total cross section compared with the LO contributions can be as large as 30% [39, 9]. The NLO corrections also have sizable effects on the shapes of many top quark kinematic distributions.

More importantly, NLO processes are the lowest higher-order processes that generate a non-zero forward-backward asymmetry via the SM. As a result, we will limit our discussion of higher-order QCD effects in top quark pair production to the NLO processes that contribute to A_{FB}.

At parton level, the dominant sources of non-zero A_{FB} are the NLO corrections to the process of $q\bar{q} \to t\bar{t}$. The asymmetry originates from the interference of virtual radiation of gluon (box diagram) in Fig. 2.9(c) and Born process (LO) of $q\bar{q} \to t\bar{t}$ in Fig. 2.9(d) [38]. In order to avoid the infrared divergences when the momenta of the virtually radiated gluon in Fig. 2.9(c) go to zero, it has to be summed with the

interference between initial state and final state real gluon emission of $q\bar{q} \to t\bar{t}$, which are described by Fig. 2.9(a) and Fig. 2.9(b) . The inclusive asymmetry from this source is positive, between 6% and 8% in most of the kinematic regions that can be probed in Tevatron or LHC.[39]

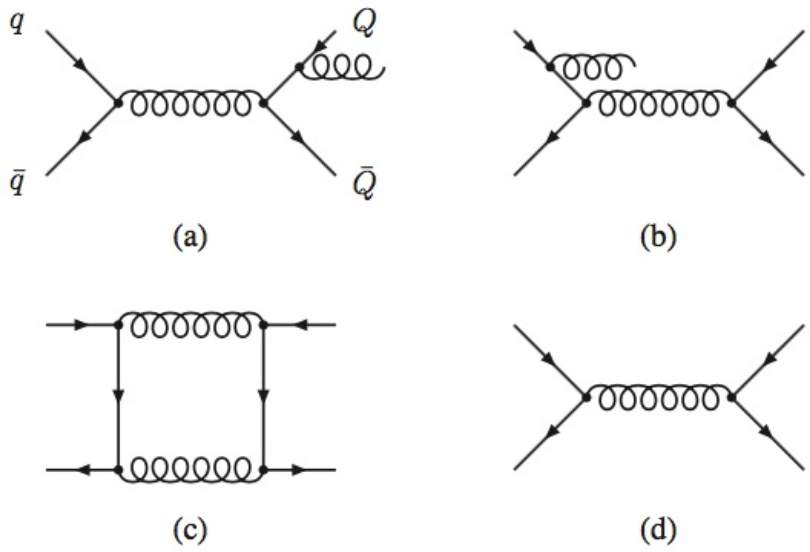

Figure 2.9: Feynman diagram of next-to-leading order $t\bar{t}$ production that contributes to A_{FB}. In the figure, q indicates light quark, Q represent heavy flavor quark, in our case, top quark.[38]

Another non-negligible source of A_{FB} is from the interference of QCD induced $t\bar{t}$ production and electroweak induced $t\bar{t}$ production. The color singlet configuration of QCD box diagram, Fig. 2.9(c), interferes with the s-channel $t\bar{t}$ production via photon, which is also color singlet.

Because some of the QCD contributions to $A_{\rm FB}$ originate from NLO terms involving real gluon radiation, this thesis actually studies the $A_{\rm FB}$ observed in $t\bar{t}+$jet production, where jet refers to the hadronized products of an extra quark or gluon. As a consequence of the additional jet allowed, another process that is predicted to produce non-zero $A_{\rm FB}$ should be mentioned, the so-called "flavor excitation" in the $g+q \to t+\bar{t}+q$ channel. It originates from the interference terms of the amplitudes for the quark-gluon scattering. Like radiative corrections for $q\bar{q} \to t\bar{t}$, the matrix element of this calculation has the order of α_s^3, and the relevant Feynman diagrams are shown in Fig. 2.10. The parton level $A_{\rm FB}$ originating from $g+q \to t+\bar{t}+q$ is much smaller than that from $q\bar{q} \to t\bar{t}$ process.

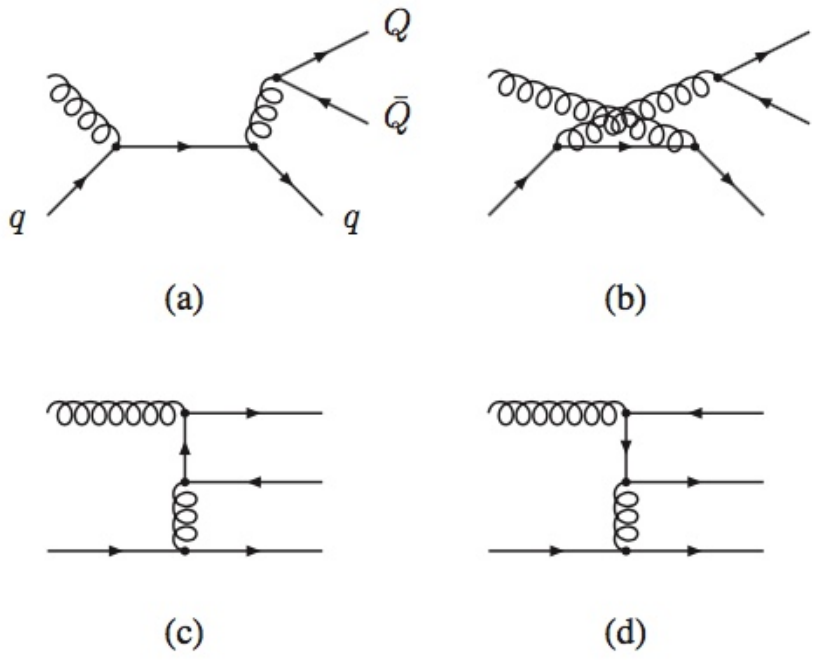

Figure 2.10: Feynman diagram of next-to-leading order $t\bar{t}+q$ production via quark gluon initial states, that contributes to $A_{\rm FB}$. In the figure, q indicates light quark, Q represent heavy flavor quark, in our case, top quark.[39]

In the energy scale studied in this thesis, where the partonic center of mass energy $\sqrt{\hat{s}}$ is below 1 TeV, the contributions of the order α^3 corrections to the $q\bar{q}$ process, the interference of QCD-QED, and the $g+q \to t+\bar{t}+q$ process to the partonic level $A_{\rm FB}$ are about 7%, 1% and 0.1%, respectively. In addition, the differential asymmetry is approximately a linear function of $\cos\theta_*$ for both $q\bar{q}$ and QCD-QED interference terms, while it is approximately quadratic for $g + q \to t + \bar{t} + q$ terms. For both reasons, we attempt to measure the $A_{\rm FB}$ originating from the $q\bar{q} \to t\bar{t}$ process from our data and correct the measured value for the $g+q \to t+\bar{t}+q$ contributions using MC simulation.

There is one subtlety when we use NLO MC simulated events to estimate the $A_{\rm FB}$ and compare that value with the analytic calculations of [38, 39, 14]. In those references the symmetric part of the cross section is calculated at LO (α_s^2), while the prediction from the direct counting of NLO Monte-Carlo simulations assumes NLO cross section. Given that the NLO corrections increase the total cross section of this process by up to 30%, this means the $A_{\rm FB}$ derived by direct counting from the NLO MCs is only 0.7 times the value from theoretical prediction given in [39].

In this thesis, the SM prediction of $A_{\rm FB}$ is chosen as the the value suggested by NLO MCs at parton level, before any parton-showering, detector simulation and

selection is performed.

2.1.3 Top Quark Production in Hadron Colliders

In previous sections, we have described the parton level production of top anti-top pairs according to the SM. In reality, quarks are never observed as isolated free particles. Because of the strong interaction, it is the colorless bound states of quarks: mesons (quark-antiquark pairs) such as pions and bayons (three quarks) that are actually observed in both the initial and final states of any scattering experiments. Because of the coupling constant of the strong interaction is very large at the low mass scales of the hadrons, detailed calculations of particle processes are not possible using perturbation theory. However, because of the asymptotic freedom property of QCD, it can be shown that the phase space and kinematic distributions of scattering involve strong interactions can be described by a hard process in which large momentum transfer happens. An intuitive understanding is during the hadronization any process with large momentum transfer is suppressed as it corresponds to small coupling constant, so the hadronization products are are produced only at small center-of-mass energies with respect to each other and they are nearly collinear with the original quasi-free particles involved in the hard scattering process.

Another result of asymptotic freedom in QCD is the factorization theorem, which says the cross section for the scattering of hadrons can be calculated by convolving the parton distribution functions (PDF) that describe the distributions of momentum

fractions carried by the partons that form the scattered hadron, with the cross section for hard scattering process. We some times call the hard scattering process the parton level process. So the total cross sections for $t\bar{t}$ production in proton-proton or proton anti-proton collider can be represented in the following way:

$$\sigma_{p_1 p_2 \to t\bar{t}} = \sum_{(i,j)\in(q,\bar{q},g)} \int_0^1 \int_0^1 (\sigma_{ij\to t\bar{t}}) D_i^{p_1}(x_1, Q) D_j^{p_2}(x_2, Q) dx_1 dx_2 \tag{2.4}$$

where p_1, p_2 can be either proton or anti-proton depending on the type of collider. $D_i^{p_1}(x, Q)$ is the PDF, which gives the differential probability that a parton, such as an up-quark, shares the fraction x of the momentum of its parent hadron of type p_1 (proton or anti-proton). Note that the PDF also depends on the energy scale Q of the hard process. Similarly, differential cross sections in hadron collisions can also be factorized by the convolution of the PDFs and parton level differential cross sections.

The PDF are determined experimentally by fitting data from hadron scattering experiments and deep inelastic scattering experiments[27]. One example of a proton PDF at the energy scale of $t\bar{t}$ production is shown in Fig. 2.11. It shows that the valence quarks in the proton (consisting of two up-quarks and one down-quark), the up- and down-quarks, tend to carry larger fractions of the proton momentum than the fractions carried by sea quarks, such as $\bar{u}$ and $\bar{d}$ quarks, and gluons.

The parton distribution functions have major consequences for the dominant production mechanisms of top quarks at the LHC and the Tevatron. The kinematic constraint of $t\bar{t}$ production requires that the center-of-mass energy of the initial par-

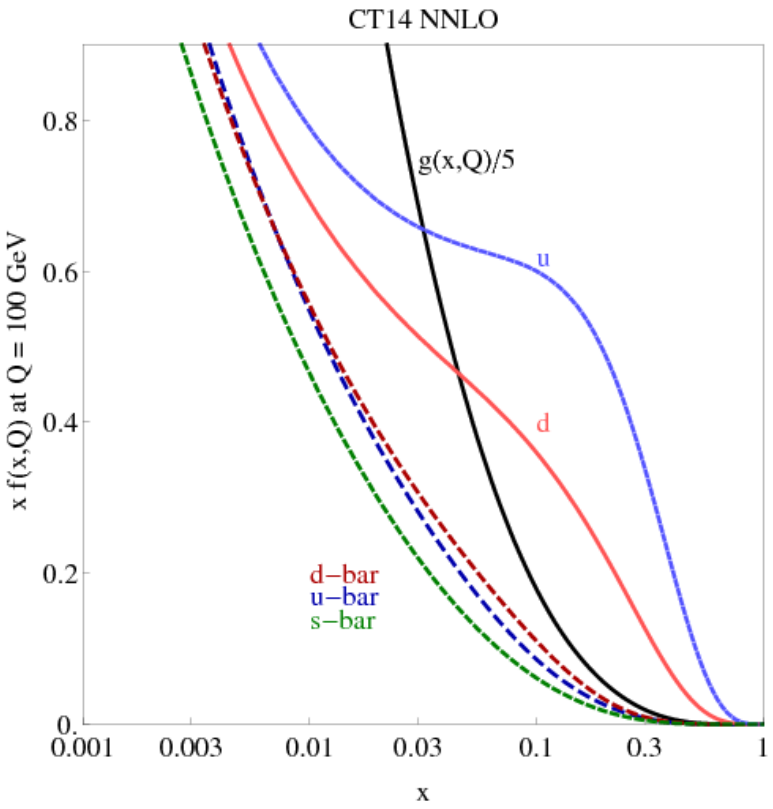

Figure 2.11: The CT14 NNLO parton distribution functions at Q = 100 GeV for u,$\bar{u}$,d,$\bar{d}$,s,$\bar{s}$ and g.[27]

tons (which is also the invariant mass of produced $t\bar{t}$ pairs) $\sqrt{\hat{s}} = M_{t\bar{t}} = \sqrt{x_1 x_2 s}$ (s is the proton-proton or proton-antiproton center-of-mass energy), to be at least two times the mass of top quarks, which is about 345 GeV. Such a large energy requirement indicate that both partons need to carry sufficiently large fractions of the energies of the collided hadrons to produce $t\bar{t}$ pairs.

In Tevatron which is a proton anti-proton collider, the dominant parton level production mechanism of $t\bar{t}$ is via $q\bar{q}$ initial states (about 90%). This is because both the initial quark and anti-quark could be valence quarks from proton or anti-proton in the collision, thus are more likely than initial state gluons to carry sufficient momentum for $t\bar{t}$ production. In contrast, the majority of $t\bar{t}$ pairs in LHC is produced via gg fusion process, as LHC is a proton-proton collider and it is unlikely for an anti-quark to carry sufficient momentum. Therefore, the $q\bar{q} \to t\bar{t}$ subprocess is only about 10% of the total $t\bar{t}$ cross section at the LHC at 8 TeV.

The consequence is that the $t\bar{t}$ A_{FB} at the LHC is much smaller than that at the Tevatron due to the dilution by the forward-backward symmetric $gg \to t\bar{t}$ process. Another challenge is that at the Tevatron because of the valence antiquarks in antiproton beam, initial quark is almost always along the same direction of initial proton, so we can choose the direction of initial proton as the positive direction when we determine the production angle $\cos\theta_*$. In contrast, in LHC the initial beam configuration is forward-backward symmetric. This makes the inference of quark direction at parton level more difficult. The solution for this problem follows from the

observation that the quark in the $q\bar{q} \rightarrow t\bar{t}$ process likely carries more momentum than anti-quark. So the direction of direction of $q\bar{q}$ c.m system is usually the initial quark direction, especially in the case where the difference of momentum fraction of initial quarks, $|x_f| = |x_1 - x_2|$ is larger, i.e. the $t\bar{t}$ c.m. system has higher boost in longitudinal direction.

2.2 Top Decay

The top quark decays via weak interaction almost exclusively to a W boson and a bottom quark due to the form of CKM matrix, where $|v_{tb} \sim 1$. In addition, because of the mass of top quark 173 GeV is much larger than the mass of W boson, the top quark decay width is so large that the top quark decays happens in a shorter time than the hadronization time. Therefore, top quark decay can be calculated with perturbative QCD very accurately.

The final states of $t\bar{t}$ events can be categorized based on the decay mode of the two W bosons. W bosons decay weakly to a quark anti-quark pair (u,d,c,s type),which is called hadronic decay, or to a lepton-neutrino pair (leptonic decay). Therefore, there are three different experimental decay topologies for $t\bar{t}$ pairs:

- All-hadronic: Both W bosons decay hadronically, $t\bar{t} \rightarrow b\bar{b}jjjj$

  The most abundant decay mode, which is about 44% of all $t\bar{t}$ events, as shown in Fig. 2.12. It is not as clean as the other two channels, with large

W+jets and QCD multijet backgrounds.

- Semileptonic: One of the W bosons decays leptonically and the other decays hadronically, $t\bar{t} \to b\bar{b}l\nu jj$. The Feynman diagram is shown in Fig. 2.13

  We only consider the case where lepton is electron or muon, and ignore the case where lepton is tau, because tau will quickly decay which is complicated to reconstruct.

  This channel is optimal for studying A_{FB} for several reasons: It is relatively clean due to the requirement of a electron or muon and two bottom quarks; it is relatively abundant, about 30% of all $t\bar{t}$ events, providing sufficient statistics for the measurement; It has only one neutrino, making it relatively easy to correctly reconstruct the momentum of top and anti-top from their decay products.

- Dileptonic: Both W bosons decay leptonically, $t\bar{t} \to b\bar{b}ll\nu\nu$

  This is the cleanest channel, due to the requirement of two leptons. The problem is the relative small abundance (about 4%), and existence of two neutrinos makes reconstruction of top anti-top momentum challenging, thus not suitable for our purpose.

As mentioned in Section.2.1.2, we allow an extra hard gluon from the ISR or FSR radiation processes associated with $t\bar{t}$ production. As a result, the final state studied in this thesis is l+4/5jets+MET, where MET means missing transverse energy which corresponds to the transverse momentum of the unobserved neutrino.

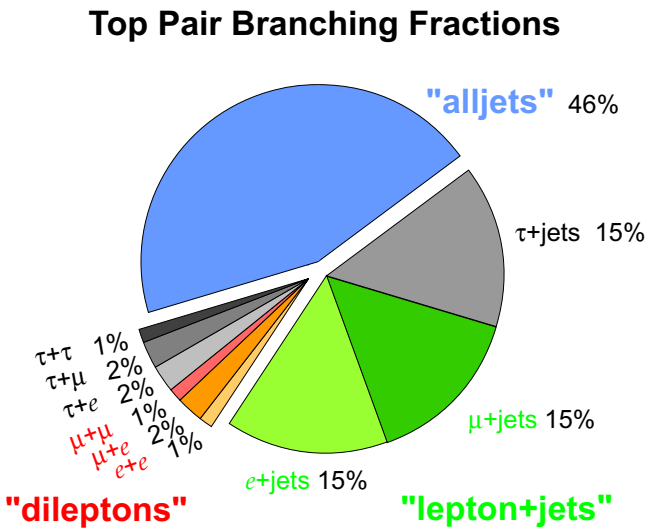

Figure 2.12: The branching fractions of all channels of $t\bar{t}$ productions.

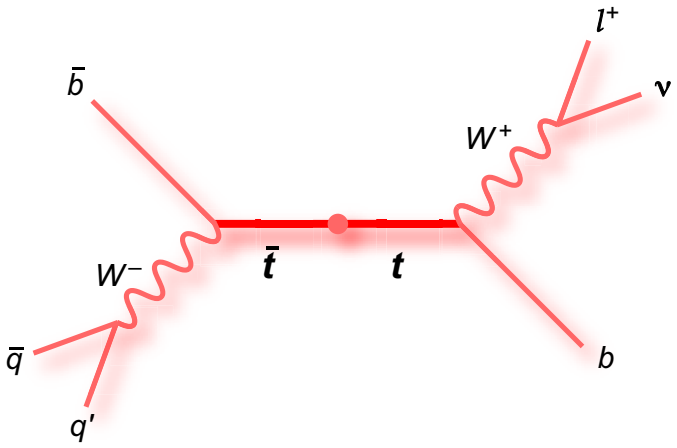

Figure 2.13: The diagram of semileptonic decay of $t\bar{t}$ pairs. There is another decay process with $W^- \to l^- \bar{\nu}$ not shown here.

Chapter 3

Experimental Setup

3.1 The Large Hadron Collider

The Large Hadron Collider (LHC) [15] is the world's largest and most powerful particle accelerator. It is located in a tunnel on the France-Switzerland border. The tunnel is 50-175m underground and has a circumference of about 27km. Two particle beams are kept in separate beam pipes, in ultrahigh vacuum, and travel in opposite directions. The beams are guided by 1232 dipole magnets, focused by 392 quadruple magnets, and accelerated by 16 radio frequency (RF) cavities. The high energy beams are made to collide at four points, where the four major detectors CMS, ATLAS, ALICE and LHCb are located. CMS and ATLAS are general purpose detectors with a wide range of research topics. LHCb is designed to study the physics of the b quark, and ALICE is an experiment that is dedicated to the study of heavy ion collisions.

The LHC primarily collides proton beams. The protons are extracted from hydrogen gas inside a Duoplasmatron. Before entering the main LHC ring, the proton energies are increased in several steps. First, a linear accelerator (LINAC2) increases their energies to 50 MeV. Next, they enter the Proton Synchrotron Booster (PSB), where they are accelerated to 1.4 GeV. The Proton Synchrotron (PS) and Super Proton Synchrotron (SPS) further increase their energies to 26 GeV and 450 GeV respectively, before they finally enter the main LHC ring for acceleration to the collision energy.

In addition to collision energy, the most important factor that characterizes the collider performance is luminosity. Luminosity is the proportionality factor between event rate and cross section. It depends on a number of beam parameters and can be calculated as [13]:

$$\mathcal{L} = \frac{\gamma f k_B N_p^2}{4\pi\epsilon_n \beta^*} F \tag{3.1}$$

where: γ is the Lorentz factor, f is the revolution frequency, k_B is the number of bunches per beam, N_p is the number of particles per bunch, ϵ_n is the normalized transverse emittance, β^* is the betatron function at the interaction point, and F is the reduction factor due to the crossing angle. The design values of the beam parameters are summarized in Table 3.1. The design luminosity is 10^{34} $\mathrm{cm}^{-2}\mathrm{s}^{-1}$, leading to around 1 billion proton-proton interactions per second.

Parameter	Symbol	Design Value
Energy per nucleon	E	7 TeV
Design luminosity	$\mathcal{L}$	10^{34} cm^{-2}s^{-1}
Bunch separation		25 ns
Number of bunches	k_B	2808
Number of particles per bunch	N_p	1.15×10^{11}
β-value at IP	β^*	0.55 m
Normalized transverse emittance	ϵ_n	3.75 μm
Number of collisions per bunch crossing	n_c	20

Table 3.1: LHC operational parameters and their design values.

3.2 Compact Muon Solenoid

The Compact Muon Solenoid (CMS) is a general purpose detector, designed to study a wide range of processes in particle physics [13]. The CMS detector is made of nested subdetectors. Closest to the beam pipe is the all-silicon inner tracker, which register the tracks of all charged particles with high resolution. The electromagnetic calorimeter (ECAL) consists of lead tungstate crystals is located outside of the inner tracking system, and is used to measure the energies of electrons and photons. The brass/scintillator sampling hadron calorimeter (HCAL) surrounds the ECAL and is used to measure the energies of charged and neutral hadrons. Outside the HCAL is the superconducting solenoid that generates a magnetic field of 3.8T. The strong magnetic field bends the tracks of charged particles and helps to measure their momentum with high resolution. The Muon system is the outmost layer of the CMS, because muons can penetrate all of the previous subdetectors. The muon system, combined with the inner tracker, provides precise measurements for muons. The overall layout of the CMS detector is shown in Figure 3.1

3.2.1 Coordinate System

The CMS detector adopts a combination of Cartesian and cylindrical coordinates. The origin of the coordinate is at the nominal collision point. The x-axis is directed radially inward toward the center of the main LHC ring, and the y-axis is pointing

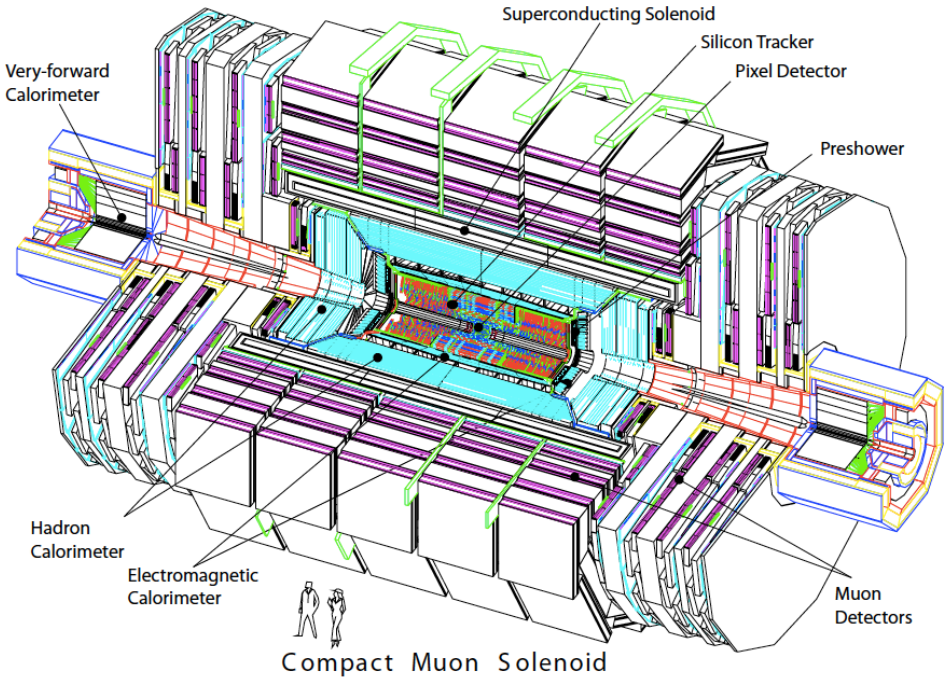

Figure 3.1: Layout of the CMS detector.

vertically upward. The z-axis is along the counterclockwise beam direction.

In the transverse plane, the azimuthal angle ϕ is defined as the angle measured from x-axis. The polar angle θ is defined as the angle measured from the z-axis in the y-z plane. The pseudorapidity η is defined as $-\ln\tan(\theta/2)$. The pseudorapidty converges to the definition of rapidity when the particle is traveling close to the speed of light. The rapidity difference $\Delta\eta$ is Lorentz invariant under boost along the beam direction, so the particle production is approximately uniform in η.

3.2.2 The Magnet

The curvature of a charged particle track in a magnetic field is inversely related to the momentum of the particle. CMS uses a large superconducting solenoid to measure the momenta of charged particles to high resolution. The solenoid is 13 m in length, 5.9 m in inner diameter and weights 1,2000 tons. It has 2168 turns that carry a current of 19.5kA and store an energy of 2.7 GJ. The superconducting solenoid is cooled to $-268.5°$C by liquid helium. A uniform magnetic field of 3.8T is generated inside the solenoid, where the inner tracker, ECAL and HCAL are located. The return yoke is interleaved with the muon system chambers and provides magnetic field for a second momentum analysis of transiting muons.

3.2.3 Inner Tracking System

The inner tracking system is used to measure the trajectories of charged particles and reconstruct interaction vertices to high precision. It consists of 3 layers of silicon pixel detectors and 10 layers silicon strip detectors, as shown in Figure 3.2 [23]. The hits (energy deposits) in the layers are used for reconstructing tracks.

Three cylindrical layers of pixel detectors (BPIX) are located in the barrel region, at the radii of 4.4, 7.3 and 10.2cm. Two endcap disks (FPIX) are arranged in each side of the forward region, at |z| = 24.5cm and 46.5cm. There are 1440 silicon pixel modules made with 66 million pixels of size $100 \times 150 \mu\text{m}^2$. The precision of position measurement is about 10μm in transverse plane, and 20μm in z direction.

The strip detector is subdivided into 4 layers in the Tracker Inner Barrel (TIB), 6 layers in the Tracker Outer Barrel (TOB), 3 disks in the Tracker Inner Disk (TID) and 9 disks in the Tracker End Cap (TEC). One third of the layers are made of double-sided "stereo" modules, providing two dimensional measurements. The 15128 modules consist of 9.6 million microstrips, with thicknesses ranging from 320 μm to 500 μm.

3.2.4 Electromagnetic Calorimeter

The Electromagnetic Calorimeter (ECAL) is placed outside of the inner tracking system, and is responsible for electron and photon measurements. It is made of

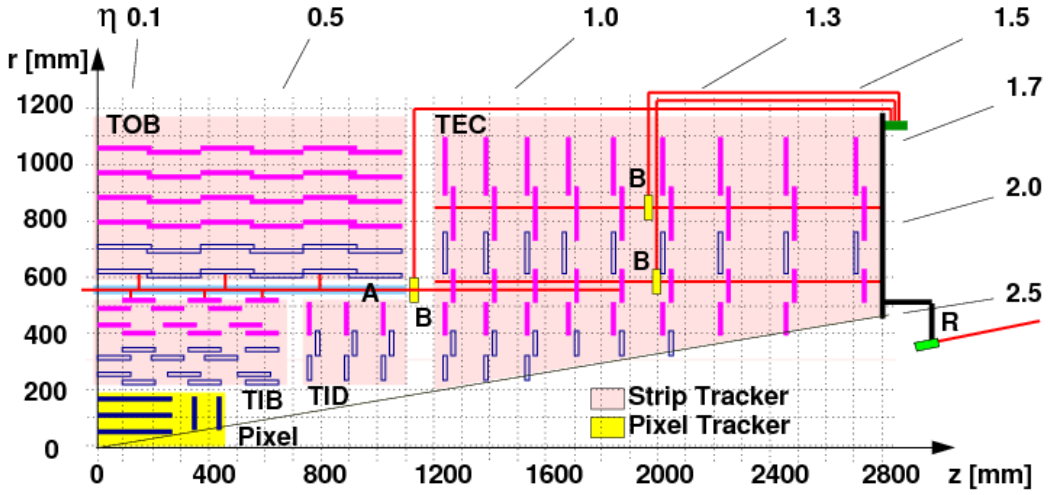

Figure 3.2: Layout of a quarter of CMS inner tracking system. The blue lines represent double-sided modules and the pink lines represent the single-sided modules.

scintillating lead tungstate ($PbWO_4$) crystals which fully contain the electromagnetic showers produced by incident electrons or photons, and emit light in proportion to the incident particle's energy. Lead tungstate has a short Moliere radius of 21.9 mm and a short radiation length of 8.9 mm. It also has fast response time and is radiation hard. Each piece of crystal has a square cross-section with sides of $22 - 25$ mm, and length of 220-230 mm.

The barrel section (EB) of ECAL is made of 61,200 crystals, structured into 36 "supermodules". The EB has an inner radius of 129cm, and covers the pseudorapidity range of $0 < |\eta| < 1.48$. The two endcaps (EE) are each made of 7,324 crystals, and cover the pseudorapidity range of $1.48 < |\eta| < 3$. The ECAL preshower detectors

(PS) are positioned in front of the endcaps, and cover a pseudorapidity range from $|\eta| = 1.65$ to 2.61. The finer granularity in PS provides better $\pi^0 - \gamma$ separation.

The scintillation light from $PbWO_4$ crystals is detected by photodetectors and converted into amplified electrical signals. Silicon avalanche photodiodes (APDs), with a gain of 50-100, are used in barrel region. Vacuum phototriodes (VPTs), with a gain of 10, are used in the endcaps.

3.2.5 Hadronic Calorimeter

The Hadronic Calorimeter (HCAL) measures the energies of charged and neutral hadrons. It is a sampling calorimeter, with alternating layers of brass absorber and plastic scintillator. The brass in the absorber layers has a short radiation length and is non-magnetic. Transiting hadrons shower the in denser absorber layers. The charged particles in the showers produce scintillation light in the plastic scintillator layers. The plastic scintillator tiles pass the light to readout system through wave-length shifting fibres.

HCAL consists of four parts: hadron barrel (HB), hadron outer barrel (HO), hadron endcap (HE), and hadron forward (HF). The HB covers the pseudorapidity range $|\eta| < 1.4$, and the HE covers $1.3 < |\eta| < 3$. HF covers the high-radiation forward region of pseudorapidity $3 < |\eta| < 5$. Steel absorbers are used in the HF. The HO is the only component located outside the solenoid magnet and is responsible for collecting any energy from hadronic showers that leak through the hadron barrel

region.

3.2.6 Muon System

Muons are the only particles that are likely to penetrate the ECAL, HCAL and several meters of iron. Therefore, the muon chambers are located outside of all the other CMS subdetectors. There are four muon stations interleaved within the iron return yoke. Hits from multiple muon stations, combined with hits from the inner tracker, are fitted to muon track hypotheses, and provide improved momentum measurement. For low momentum muons, the inner tracker resolution dominates, while at high momentum, the muon chamber resolution dominates.

Three types of gaseous muon detectors are used in the muon system: the muon drift tubes (DT) in the barrel region, the cathode strip chambers (CSC) in the endcaps, and the resistive plate chambers (RPC) in both the barrel and endcap regions.

Each rectangular aluminum DT is filled with $Ar/CO_2(85/15\%)$ gas and contains a 50 μm diameter anode wire. When charged particles pass through the volume, the gas atoms are ionized and electrons are released. The electrons travel to the anode and produce electrical signals. The locations of the anode and the travel times give the coordinates of the particles.

Each CSC consists of an array of anode wires, perpendicular to cathode strips, in an Ar/CO_2 gas volume. When charged particles pass through, the gas atoms are ionized. The electrons travel to the anode wires, while the positive ions move to the

cathode strips, creating charge pulses in the both. The closely spaced anode wires and cathode strips give precise coordinates of the particles.

Each RPC consists of two parallel Bakelite electrodes separated by a gas gap. It has a less precise space resolution but a good time resolution. Charged particles ionize the gas atoms and induce avalanche in the electromagnetic field. The electrons and ions then travel to the electrodes and produce the signals. The fast momentum measurement is used by the trigger.

Chapter 4

Physical Object Reconstruction and Definition

In this thesis, the fundamental building blocks of $t\bar{t}$ events are physics objects, such as electrons, muons, jets and missing transverse energy (MET) which represents neutrinos. In CMS, these objects are reconstructed from digital signals from all relevant sub detectors, including trackers, calorimeters and muon trackers, using the Particle-Flow (PF) algorithm [1] together with jet clustering algorithms.

A list of these reconstructed objects, called PF candidates, is the starting point for further event selection, that applies specific criteria to the quality and the kinematic properties of the PF candidates, to keep as many signal events as possible while reducing the number of background events. The PF candidates after the selection are used to reconstruct the top and anti-top quarks by performing a kinematic recon-

struction that chooses the best combinations to make a plausible pair of top quarks. As the sensitivity of the measurement on A_{FB} depends on an accurate reconstruction of the $\mathrm{t\bar{t}}$ pairs, it is critical to understand the reconstruction of each individual pieces in this picture.

In this chapter, the reconstruction of physical objects such as leptons and jets from reconstructed sub-detector data is introduced, followed by the specific definitions of the physical objects used in the analysis of this thesis.

4.1 Overview of event reconstruction

The particle-flow algorithm first reconstructs all stable particles, including electrons, muons, photons, charged hadrons and neutral hadrons, by combing the information of CMS sub-detectors optimally according to carefully designed metrics. The list of reconstructed particles is then used to construct jets, which result from the hadronisation of partons, and the MET, which is the imbalance of transverse momentum of all PF candidates. In addition, the PF candidates are also used to calculate the relative isolation (RelIso) of leptons, which is the ratio of the momentum of PF candidates outside of a certain distance from the lepton to the momentum of candidates within the distance. This isolation variable is an important discriminating variable for rejecting fake leptons.

Fundamental Elements

The fundamental building blocks of particle reconstruction are charged particle tracks, calorimeter clusters and muon tracks. A brief overview of the techniques for the reconstruction of these elements is given below.

Tracks are reconstructed from the hits in the layers of innermost pixel tracker and the silicon strip tracker outside the pixel tracker, using an iterative algorithm [19]. The tracking software is called Combinatorial Track Finder (CTF), based on a combinatorial Kalman Filter, that allows pattern recognition and track fitting at the same time.

Starting from a collection of hits in the tracker systems, as many as six iteration of track finding are performed. The initial iterations reconstruct tracks that are easiest to find, and with very tight criteria, leading to reconstruction of high p_T tracks from the primary interaction vertex. In each iteration, hits that belong to previously reconstructed tracks are removed. The later iterations start with looser seeding criteria, and reconstruct the tracks that are more often from secondary vertices. The efficiency for finding charged hadron tracks in central region of the detector is above 90%, with a resolution in measured p_T of about 1.5%.

Calorimeter clusters are used for measuring the energy deposits of charged particles, such as electrons and charged hadrons, and neutral particles, such as photon and neutral hadrons. They crucial for detecting the energies and directions of neutral particles which don't leave any tracks in tracker system. In addition, they are

used to identify and reconstruct electrons which are accompanied by bremsstrahlung photons. Calorimeter information is a key part of the PF clustering algorithm which must separate the energy deposited by neutral particles from that due to charged particles.

The clustering algorithm first identifies cluster seeds which are calorimeter cells with maximal energy. Then, topological clusters are formed around the seed by aggregating the adjacent cells that have energy deposits beyond a certain threshold. The clustering algorithm is performed separately in all sub-detectors, including the ECAL, HCAL and PS calorimeters. The reconstructed energy clusters are later used for charged PF particle reconstruction by incorporating tracking information.

Particle-Flow Algortithms

After the input elements are collected, the PF algorithm is applied to reconstruct particles. The PF algorithm can be separated into two stages. The first stage links several elements in various CMS sub-detectors, called a block, and treats the block as the detector response from one single particle. This process avoids double counting the same particle in several detectors, as well as improves the accuracy of the particle identification. For example, a charged hadron, like a pion, leaves hits in tracker which are reconstructed as a track, and creates energy deposits in the ECAL and HCAL, which are individually grouped as clusters. The link algorithm is performed for each pair of detector elements, and if the pair of elements are marginally consistent

with the hypothesis of coming from the same stable particle, the link is established. For example, a link between a track and ECAL or HCAL clusters is established if the extrapolated position of the track in the corresponding calorimetry is within the boundary the linked cluster. In addition to forming links, a link distance between the extrapolated track position and the cluster position is computed to quantify the consistency of the link.

The second stage is particle reconstruction and identification from the linked blocks. Different types of particles are reconstructed and identified as part of the block in the order of muon, electron, neutral hadron, charged hadron, and photon. The successful reconstruction of each particle relies on consistency of the combination of elements in the block. If more than one combination of elements is possible, the optimal combination is selected based on the distance computed in the linking stage. Any element, such as a track and calorimeters cluster, once associated with the reconstruction of a particle, is removed and remaining elements in a block are used for reconstruction of other particles.

Lepton Isolation

Among the discriminating variables used for lepton identification, the relative isolation RelIso of the lepton is of critical importance especially for electrons. The requirement of isolation is very effective in reducing the background from jets misidentified as electrons and from electrons embedded within jets that are produced from

the decay of b or c quarks. In both cases, there are a significant number of charged particles near the electron candidate. Therefore,$\mathrm{RelIso_{PF}}$ that quantifies the total energy surrounding the electron candidate, is defined as follows, based on the PF candidates:

$$\mathrm{RelIso_{PF}} = \frac{\sum p_{\mathrm{T}}^{\mathrm{charged}} + \max\left[0, \sum p_{\mathrm{T}}^{\mathrm{neutralhad}} + \sum p_{\mathrm{T}}^{\gamma} - p_{\mathrm{T}}^{\mathrm{PU}}\right]}{p_{\mathrm{T}}^{\mathrm{electron}}} \tag{4.1}$$

In the above the definition is designed to remove the noise due to presence of neutral hadrons and extra charged hadrons due to additional interactions (called Pile Up), the detail of which is beyond the scope of the discussion here.

4.2 Object reconstruction and definition

4.2.1 Muons

Muon Reconstruction

Muons are the particles that are reconstructed best in CMS due to the superior inner tracker, muon system and the strong magnetic field from the superconducting solenoid. Muons are reconstructed based on the tracker tracks in the inner tracker and muon tracks in the muon system. There are two types of muons depending on reconstruction algorithm: tracker muons and global muons.[18]

Global muons are reconstructed by first finding matching tracker and muon tracks

by propagating both tracks into a common region. Once matching tracks are found, the hits belonging to both tracks are fit again using a Kalman-filter technique to establish a global muon that has better momentum resolution than either of the matched tracks.

Tracker muons are reconstructed inside-out, meaning that the tracker tracks are propagated all the way to the muon system, taking account of the curvature caused by the magnetic field, and the energy loss and scattering caused by intervening material. Any tracks with matching muon system hits in at least one segment of muon system are considered as tracker muons.

The muon reconstruction efficiency in CMS is very high, with 99% of muons within muon system geometric acceptance and having sufficient high p_T reconstructed as either tracker muons or global muons. Most of the track muons and global muons are reconstructed from the same tracks, and are merged into a single muon candidate. Once muon candidates are reconstructed, in actual down stream physics analysis, a further selection on the muon candidates is applied to achieve a balance of efficiency of low fake muon or cosmic muon rate.

Muon Selection

For the muon+jets channel, both data and simulation are required to pass additional offline high level trigger `HLT_IsoMu24_eta2p1_v*`. This trigger selects events with at least one isolated muon of $p_T > 24$ GeV and $|\eta| < 2.1$. Additionally, real

and simulated events are required to have exactly one global muon candidate with $p_T > 26$ GeV and $|\eta| < 2.1$. In order to improve the quality of selected muon, it is also required to satisfy the set of quality cuts defined by muon Physics Object Group in CMS, call "tight" muon selection criteria. The selected muon must have global track fit quality $\chi^2/ndf < 10$. It must have at least one muon chamber hit included in the global-muon track fit, with muon segments in at least two muon stations. In addition, the muons must have at least one hit in pixel detector and have at least 5 hits in the inner tracker. In order to assure the muons are from primary collisions, the tracker tracks must have transverse and longitudinal impact parameters with respect to the primary vertex smaller than 2 mm and 5 mm, respectively. Additionally, each muon candidate is required to satisfy a particle flow based isolation (`RelIso`) requirement $\mathrm{PF_{iso}}/p_T < 0.12$ where the isolation is of the "combined relative" type with $\Delta\beta$ corrections applied to reduce pileup effects and is computed within a cone size of 0.4.

4.2.2 Electrons

Electron Reconstruction

Unlike muons, electrons are reconstructed by combining tracks from the inner tracker and clusters from the ECAL.

Because electrons lose energy via radiative processes in their interactions with the

materials in tracking system, the standard Kalman filter fitting used in PF is not sufficient to reconstruct electron tracks. Electron tracks are reconstructed by first using the same tracking algorithm that is used for all charged PF particles as described in Section 4.1. This first pass usually works for the case of small bremsstrahlung. For the case of non-negligible bremsstrahlung, the KF will fail to reconstruct the correct track due to missing hits or or will reconstruct tracks with bad quality (large χ_{KF}). In this case, a second pass of fitting is performed, using a dedicated Gaussian sum fitter (GSF).

As part of the PF algorithm, ECAL clusters are reconstructed based on GSF tracks. The goal of clustering algorithm is to cluster all the crystals in ECAL that have energy deposit from the electron and the its bremsstrahlung photons, so the energy of electron can be accurately measured. The clusters from the electron itself are identified by extrapolating the GSF tracks to the ECAL and by finding matching ECAL crystals. The clusters from the photons are identified by drawing tangent lines from the GSF track in each layer of the tracker, and extending the lines to the ECAL to find the matching crystals. The reason is that bremsstrahlung happens mostly in the material dense regions of the detector before the electron reaches the ECAL and these are the tracker layers.

Finally electron candidates are reconstructed by associating the tracks and ECAL clusters, so both momentum and energy are measured. The charge of a PF electron is determined mostly from the curvature of the track.

Electron Identification

In order to identify signal electrons that are produced in the prompt decays of particles originating from the primary interaction vertex, and to separate them from background sources, an additional selection procedure is used to identify good quality electrons. The main sources of background are the following: electron pairs from photon conversion, jets misidentified as electrons, and electrons from semileptonic decay of b and c quarks. Two different type of electron ID algorithms are widely used in physics analysis. The first is is cut-based in which criteria are applied sequentially to a set of discriminants. The second is based upon a Multi-Variate Analysis (MVA), which uses a boosted decision tree to combine many variables to maximize the discriminating power in the separation of signal and background electron candidates. In this thesis, we use the cut-based selection, which is simpler, more transparent, and more robust.

Electron Selection

For the electron+jets channel, both data and simulation events are required to pass the offline trigger `HLT_Ele27_WP80`. This trigger selects events with at least one electron having $p_T > 27$ GeV. To further select top pair events, it is required to have exactly one particle flow electron with $p_T > 30$ GeV and $|\eta| < 2.5$. Electrons with a cluster in the eta range of 1.4442 and 1.5660, which corresponds to the transition region between barrel and end-cap calorimeter, are not selected. To ensure that the

selected electron is from a primary collision, it is required that the associated track has impact parameter with respect to beam spot smaller than 0.02 cm, and has a longitudinal distance from primary vertex smaller than 0.1 cm. In addition, a cut based electron ID is applied and the selected electron is required to satisfy "tight" selection criteria defined by electron/photon (EGamma) Physics Object Group (POG) in CMS. Additionally, each electron candidate is required to satisfy a particle flow isolation smaller than 0.1 within a cone size of 0.3.

In order to reject electrons originating from the conversion of photons, a vertex fit conversion method is used and the electron selected is required to pass this conversion veto. In addition, the GSF track associated with the selected electron is required to have no missing hits in the inner tracking system.

4.2.3 Veto Leptons

Finally, to suppress signal from dileptonic top events, any event with a second muon (veto muon) or second electron (veto electron) is not selected.

A veto muon is defined as having particle flow muon ID, being a global muon, with $p_T > 10$ GeV, $|\eta| < 2.5$ and $RelIso(R = 0.4) < 0.2$.

A veto electron is defined as an electron with $p_T > 20$ GeV, $|\eta| < 2.5$ and $RelIso(R = 0.3) < 0.15$. In addition, the veto electron is required to pass the cut based electron ID with "Loose" working point as defined in EGamma POG.

4.2.4 Jets

Jets are observable objects in hadron colliders that are formed by grouping collimated bunches of stable hadrons originating from the hadronization of partons (quarks and gluons). As a direct result of QCD and asymptotic freedom discussed previously, no isolated, "bare" quarks or gluons exist. Rather, they undergo the hadronization process, forming stable particles, and they are observed as localized particle showers in the tracker and calorimeters. The showers of stable particles are clustered using jet clustering algorithms to form jets with a certain cone size. These jets are the product of reverse engineering of the hadronization process, and are studied using the parton level calculations, as demonstrated in the Fig.4.1.

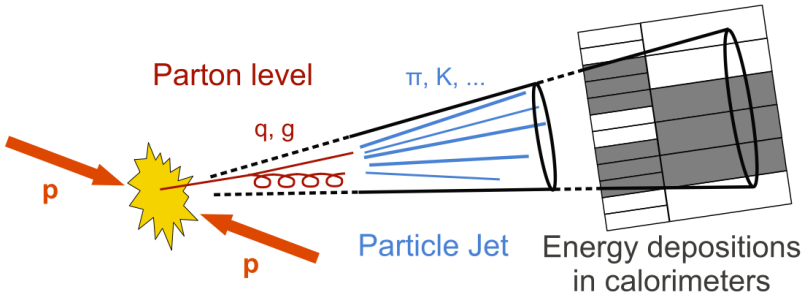

Figure 4.1: A Schematic over view of jets, and the relationship to partons in hadron colliders.[36]

Jet Reconstruction

The jets used in this analysis are reconstructed from stable PF hadrons. Due to the complexity of this topic, only a very brief summary is provided below, more details are provided in [16, 22].

There are many different jet clustering algorithms, but they should all satisfy the following requirements:

- Collinear-safe: the clustered jets should be stable under the splitting a single particle into several particles of low angular separation. This is required by the common process of collinear gluon radiation.

- Infrared-safe: clustering algorithm should be stable by adding or removing low energy radiation. It means that detector noise or additional hadrons from other pp collisions will not significantly alter the result of the jet clustering.

In this thesis, and in most CMS analyses, the anti-kT (AK) algorithm is used for jet clustering. This algorithm clusters jet from stable particles by recursively combining soft (carrying small transverse momentum) particles with hard ones. It belongs to a general type of clustering algorithms called sequential recombination algorithms, including kT algorithm and Cambridge-Aachen Algorithms.

The AK algorithms starts from defining a momentum weighted distance measure between any pair of particles (or intermediate jet, called pseudo-jet) defined as follows,

$$d_{ij} = \min(1/k_{T,i}^2, 1/k_{T,j}^2)\frac{\Delta R_{ij}^2}{R^2}, \tag{4.2}$$

$$d_{iB} = 1/k_{T,i}^2 \tag{4.3}$$

where: i,j label the particles or pseudo-jets; $k_{T,i}$ is the transverse momentum of i^{th} particle, $\Delta R_{ij}^2 = (y_i - y_j)^2 + (\phi_i - \phi_j)^2$ is the commonly used distance measure

hadron collider experiments, and R is the desired cone size of the clustered jet. In this thesis, we use the jets clustered with $R = 0.5$, and denote them as $AK5$ jets.

In each iteration, all pairwise distances d_{ij}, and beam distances d_{iB} are calculated. If the smallest of all of the distances is a pairwise distance d_{ij}, the pair of particles are merged by summing their four momenta. If the smallest one is of the beam distances d_{iB}, then the i'th particle (or pseudo-jet) is called a new jet, and it is removed from the list of particles/pseudo-jets. This combination process is repeated until all jets are identified.

What this algorithm actually does is to merge soft particles into a hard particle/pseudo-jet that is within the cone centered around the hard pseudo-jet of size R. Two hard jets will be merged into a new jet only when their separation is within R, otherwise they are kept as separate jets, per the construction of d_iB. One example of the result of AK algorithm is shown in Fig.4.2, using a cone size of $R = 1$, on the parton level simulated event. It shows that the jets are indeed clustered per the design of the algorithm.

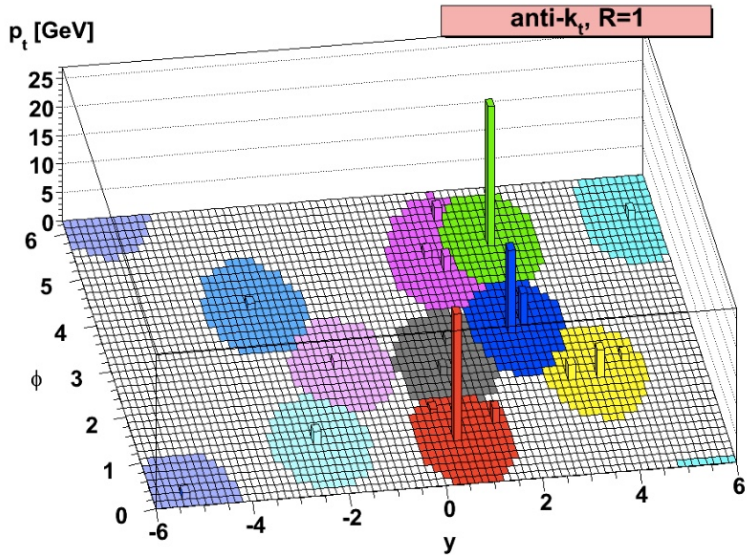

Figure 4.2: An example of AK clustering algorithm, based on simulation, taken from [16]. Cone size is $R = 1$. Each colored cone is a clustered jet. The histogram shows the p_T of underlying partons.

Jet Selection

The hadronic jets used in this analysis are reconstructed using the anti-kT algorithm with cone size 0.5. Jet energy corrections, explained in detail in Sec.6.5.1.1, have being applied following the recipe recommended by Jet and Missing Energy (JetMET) Physics Object Group [22].

All jets are required to have reconstructed pseudorapidities in the region $|\eta| < 2.5$. The selected jets in each event are required to have transverse momenta larger than 30GeV.

In addition to these kinematic requirements, we also require that at least two jets

be identified as a b-jet. The b-jet identification is based upon the Combined Secondary Vertex (CSV) tagging algorithm [49] and requires that the CSV discriminator be larger than 0.679.

Chapter 5

Process Modeling and Event Selection

At full luminosity, the LHC produces about 800 million inelastic proton-proton collisions per second. Among those, only a very small fraction of events are of interest for most physics analysis. The majority of events produced in LHC are the result of soft QCD processes. As shown in Fig.5.1, at the LHC operating at 8 TeV, the cross section for the $t\bar{t}$ production process, which is the signal process in this thesis, is about 10 orders of magnitudes smaller than the total production cross section.

This thesis measures the A_{FB} originated from $q\bar{q} \to t\bar{t}$ process, as well as the fraction of $q\bar{q} \to t\bar{t}$ production among all production mechanisms for $t\bar{t}$ in LHC. In order to achieve accurate measurements with low statistical uncertainties, we must apply selection criteria to the collected events that strike a balance between increasing signal to background ratio and while still maintaining a reasonable signal efficiency so there are a sufficient number of events left after the selection.

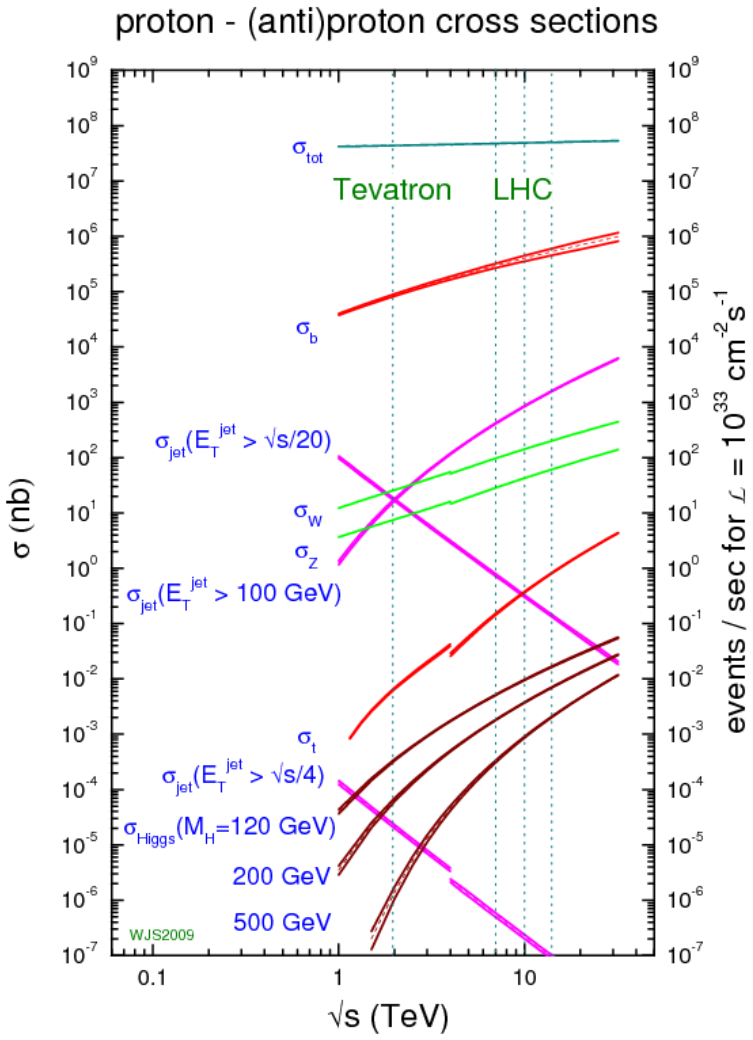

Figure 5.1: Cross sections for various physcis processes in hadron coliders, corresponding to collision energy, taken from [46]. Three different energy for LHC marked in the figure corresponds to 7,10 and 14 TeV.

The selection criteria are based on the topology of our signal events, as well as the features of the major background processes. Our signal consists of semileptonic $t\bar{t}$ events, described in Fig.5.2, with a final state of one high p_T electron or muon plus four or five energetic jets where two have originated from bottom quarks. The detailed selection criteria are given in Section.5.3.

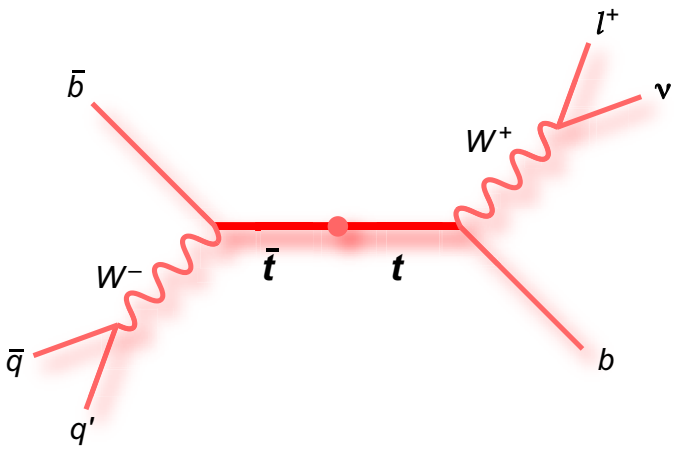

Figure 5.2: The diagram of semileptonic decay of $t\bar{t}$ pairs. There is another decay process with $W^- \to l^-\bar{\nu}$ not shown here.

Even after selection, there are still various processes that form irreducible backgrounds to the signal. In this chapter, the origin and modeling of the signal and irreducible background processes are discussed. Then the MC and Data samples are described and listed. Finally the $t\bar{t}$ event selection criteria and result is discussed.

5.1 Signal and background process modeling

5.1.1 Monte-Carlo Simulation

Most of the signal and background processes are modeled by MC simulation. The simulation process is usually performed in several steps.

The first step is to generate events based on the hard scattering process at parton level, using a dedicated Monte-Carlo event generator. The generation of hard process is based on the Matrix Element calculated using QFT, as described in Section.1.4. The ME generator can generate events with up to a few hard radiated partons due to computational complexities. The products of this step are referred to the parton-level or generator-level particles, and the information about these particles, such as particle type, charge, momentum is referred as generator truth in later chapters of the thesis.

Additional initial state/ final state radiated quarks and gluons are produced using a different event generator in the second step, which is denoted as Parton Showering (PS) process. A special matching procedure is performed between the particles generated in ME step and particles in PS step to avoid duplicates.

The third step is the fragmentation/hadronization step, which takes the partons generated in PS step and forms stable hadrons. As hadronization is non-perturbative, a phenomenological model called Lund String Model is adopted for this purpose. The decays of unstable hadrons are simulated using well-known branching ratios.

The last step of the simulation chain is to simulate the propagation of all the stable particles in the CMS detector, and the detector response in all subdetectors of CMS. This step is performed using dedicated detector simulation software.

The entire simulation chain is shown in Fig.5.3. All the signal and background process simulations follow the same procedures described in this section, with different choices of generators in ME or PS steps.

All MC simulated events are produced by the SUMMER12 central MC production campaign by CMS.

5.1.2 Signal process modeling

The signal process for this thesis is semileptonic $t\bar{t}$ production. Specifically, we look at the $t\bar{t}$ production processes in which one of the W bosons decays to electron or muon, and the other W decays to a pair of light flavor jets. The process in which one of the W decays to tau lepton is not treated as a signal process due to the complexity of tau further decay process and poor reconstruction of taus in CMS.

The signal process is modeled using the inclusive $t\bar{t}$ events generated with the aMC@NLO ME generator [11], which is an NLO event generator. The parton showering is done using the Pythia PS generator [48]. Due to the matching scheme used in aMC@NLO, the generated events are weighted, with some events having negative weights to account for the duplication of Pythia generated events [28].

An alternative signal simulation is also considered, generated using the POWHEG

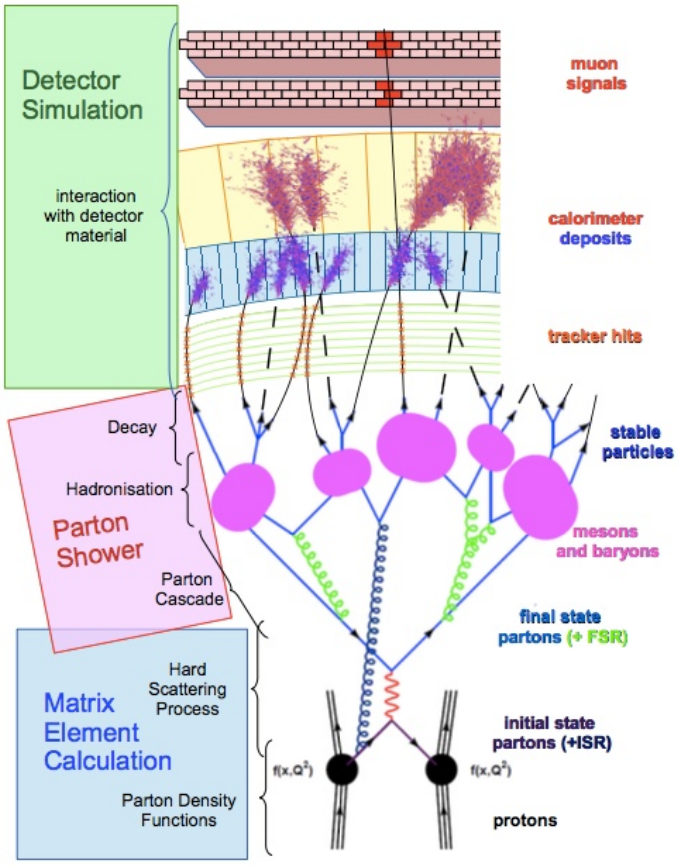

Figure 5.3: An illustration of entire Monte-Carlo Simulation chain in CMS. [29]

ME generator and use Pythia for parton showering. POWHEG is another NLO generator [10] that is designed to be interfaced with Pythia for parton showering and produces only positive weights. We use the Powheg generated signal sample to study the sensitivity of measurement to the choice of signal model in this thesis. Another relevance of the POWHEG sample in this thesis is that we used the generator level information of POWHEG generated $t\bar{t}$ events in the feasibility studies of the analysis method.

In order to get the semileptonic $t\bar{t}$ events from the inclusive $t\bar{t}$ MC sample, the generator truth information is used to select true semileptonic decay events, where one of the W boson decays leptonically, another decays hadronically.

5.1.3 Background process modeling

The requirement of a high quality lepton and two b-jets, together with requirements on the minimum transverse momenta for all the final state particles, can effectively reduce the vast majority of background events, especially those produced by the dominant QCD multijet process. Still, there are several processes have non-negligible contributions to the final event sample that is used for the analysis. These processes are called irreducible backgrounds, and need detailed and careful modeling. In most cases, the background processes are modeled by dedicated MC simulations. In the case of QCD multijet background, a data driven approach is taken as it is unfeasible to model this process purely with MC.

Non-semileptonic $t\bar{t}$ events

Two of the major irreducible backgrounds are caused by fully hadronic and fully leptonic $t\bar{t}$ events. The hadronic $t\bar{t}$ final states have two b-jets and four light flavor jets. When one of the light flavor jets is mis-identified as an electron (or muon, though less likely), some of these events can pass all selections. Fully leptonic $t\bar{t}$ events consist of two high p_{T} leptons and two b-jets and large missing energy from the two neutrinos of W decays. If one of the leptons is not identified and the event contains additional high p_{T} jets from ISR/FSR radiation, this process can fake signal events too. Another process that can fake signal is the case where one of W bosons decays to a tau lepton that further decays to hadrons, and the other W decays to an electron or a muon.

The reason why we categorize these processes as background instead of signal despite the fact that they are true $t\bar{t}$ processes is that the later top quark kinematic reconstruction procedure is designed for semileptonic $t\bar{t}$ only. As the result, any non-semileptonic $t\bar{t}$ event will be poorly reconstructed and important information like the top direction will be unreliable.

The modeling of non-semileptonic $t\bar{t}$ background is performed with the same inclusive $t\bar{t}$ sample used in the signal process modeling by selecting events that are not semi-leptonic decays of $t\bar{t}$ using the generator level information embedded in the simulation information.

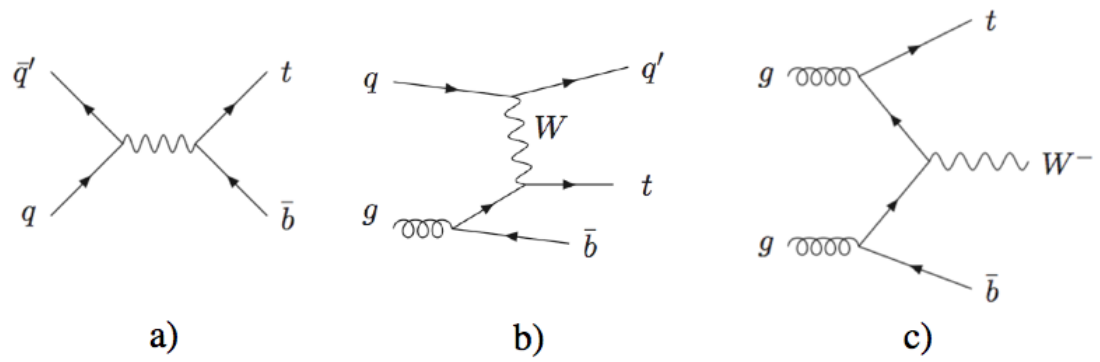

Figure 5.4: The Feynman diagrams of s,t and tW channel of single top production, from left to right.[40]

Single top production

Singly-produced top events can be very similar topologically to the signal process and are a major background in this analysis,. Representative Feynman diagrams for single top production in s,t and tW channels are shown in Fig.5.4.

The modeling of this background is via MC simulation using POWHEG as ME generator and interface with Pythia for parton showering.

W+Jets

The production of W bosons with several associated jets is another non-negligible background. Although the kinematic distribution and final states from W+Jets process is very different from the $t\bar{t}$ process, due to the large production cross section for this process, it is still possible for some events to pass all selections.

This process is modeled by using MadGraph event generator [12], a popular leading order ME event generator, interfaced with Pythia for parton showering. Note that the ME generator can handle W production with up to 4 additional jets. Events with W bosons and and more than 4 jets are simulated in the PS step, due to the computational complexities introduced by the large combinatorics by adding more jets. For this reason, as well as for other known limitations of the simulation of W+Jets process, the normalization and (possibly) the kinematic distributions predicted by the simulation are not as reliable as the other simulated processes.

Two measures are taken in order to mitigate the (possibly) poor modeling of the W+Jets process. First in the event selection, two b-tagged jets are required, which significantly reduces the fraction of W+Jets background to the 1% level. The second measure is to determine the normalization of this process via a template fit, together with the measurement of A_{FB} that is described in Section.6.1.2.

5.1.4 Data Driven QCD Multijet Background

The QCD Multijet processes (sometimes denote as QCD process in the later section for simplicity) has enormous an total cross section and extremely low selection efficiency in our analysis. As a result, we cannot rely on MC simulated events to produce background templates for this process. Instead, we use a data driven approach by selecting the data events that are kinematically and topologically very similar to real $t\bar{t}$ events, but are determined to be fake $t\bar{t}$ events by key features. These

events are called in the side-band region, because they are in the phase space that is orthogonal to the phase space of the signal events.

Definition of Side-band Region

In this thesis, the side band region is defined by inverting one of the key criteria for electrons identification (ID). In electron ID, as defined in detail in Section.4.2.2, a key step is to require the electron candidate isolated from other charged hadrons in the cone surrounds the electron. An electron that is not from prompt decay of W bosons, for example originated from jets misidentified as electrons or from the decay of b or c quarks, are not isolated. A quantity called relative isolation (RelIso) is defined to describe this effect, by calculating the fraction of momentum carried by charged hadrons surrounding the electron:

$$\mathrm{RelIso_{PF}} = \frac{\sum p_{\mathrm{T}}^{\mathrm{charged}} + \max\left[0, \sum p_{\mathrm{T}}^{\mathrm{neutralhad}} + \sum p_{\mathrm{T}}^{\gamma} - p_{\mathrm{T}}^{\mathrm{PU}}\right]}{p_{\mathrm{T}}^{\mathrm{electron}}} \tag{5.1}$$

The better the electron is isolated, the smaller RelIso it has. In the signal selection, the electron candidate is require to have RelIso < 0.1. The side band region is defined as electron candidates that satisfy all other electron ID criteria, except for the RelIso. Instead, it is require to have $0.2 <$ RelIso < 1.2. Therefore the side band region is completely orthogonal to signal region and supposed to be mostly dominated by QCD Multijet events.

Because the events in side-band region defined above satisfy almost all requirement of signal selection, the kinematic distribution of these events are expected to be very

similar to the real QCD background events in the signal region. Therefore, we use the distribution, i.e the "shape", of these events for the modeling of QCD Multijet background process. However, the number of events in the side-band region is not the same as the expected number of events of QCD background in signal region, due to different selection criteria on electrons.

Note here there remains some events in the sideband region not originated from QCD Multijet processes, but rather from other background and signal processes. As the result, the purity of the side-band region events is affected. The solution is to subtract the expected contamination of non-QCD processes modeled by MC simulations.

Estimation of QCD background Normalization

Unlike other background modeling, the event yield (number of events selected) from QCD background can not be estimated from the MC because of insufficient MC simulated events. This is not a significant issue because our measurement based on the shape of various processes and the yield of QCD background is estimated during the template fit. Still, an estimation of event yield of this background can be estimated purely from data, and used as the starting point of the event yield in the fit.

Estimation of the normalization of QCD process in signal region follows another data driven approach, called ABCD method. The idea of the method is as follows: we

denote the signal selection as the D region, and side-band selection as the C region. If we somehow knows the ratio of number of QCD events in both C and D region, denoted as conversion factor $R = \mathrm{N_D}/\mathrm{N_C}$, then it is obvious that number of QCD events in signal region can be calculated give both number of QCD events in C region and the converting factor. Apparently, we cannot know this ratio from C and D region along, because otherwise we don't know the number of QCD events in signal region in the first place. The key idea of this method is that we can estimate this factor by using the observed events in a newly defined A and B region that are suppose to be QCD enriched, and are correlated in the same fashion as the C and D region.

The additional side-band regions that are orthogonal to both signal and the original side-band region (C region) are defined by inverting another electron ID criteria, and denoted by the name of the flag: "Tight ID", "Loose ID". Our choice of selection criteria for the ABCD(EF) regions are defined in Fig.[5.1]. Control plots are shown in Fig.[5.5]. Using this method, we compute conversion factor as defined in Table.[5.2], and apply it to get an estimate of number of events for QCD Multijet process in signal region.

Based on the conversion factor calculated from ABCD method, and the number of observed events in C region, we expect 547 events from QCD multijet process, and we assigned a conservative uncertainty of 20% in the nuisance parameter R_{QCD} in our template fit.

Definition	Loose ID: fail	Loose ID: pass, Tight ID: fail	Tight ID: pass
$0.2 <$ RelIso < 1.2	A	E	C
RelIso < 0.1	B	F	D

Table 5.1: C Region is the side band region used for QCD background modeling. D region is the signal region. A/B and E/F regions are corresponding side-band regions for conversion factor calculation.

Method	predicted QCD events	$\sigma_{N_{QCD}}$	R_{QCD}	$\sigma_{R_{QCD}}$
N_{QCD} in D = B/A*C	547	52	1.3%	0.12%
N_{QCD} in D = F/E*C	435	129	0.98%	0.293%

Table 5.2: Expected number of QCD events in signal region based on the observed data events in side band C region and the conversion factor calculated from A/B and/or E/F regions. $\sigma_{N_{QCD}}$ and $\sigma_{R_{QCD}}$ are corresponding uncertainties assuming the number of observed events in each region follows Poisson distributions.

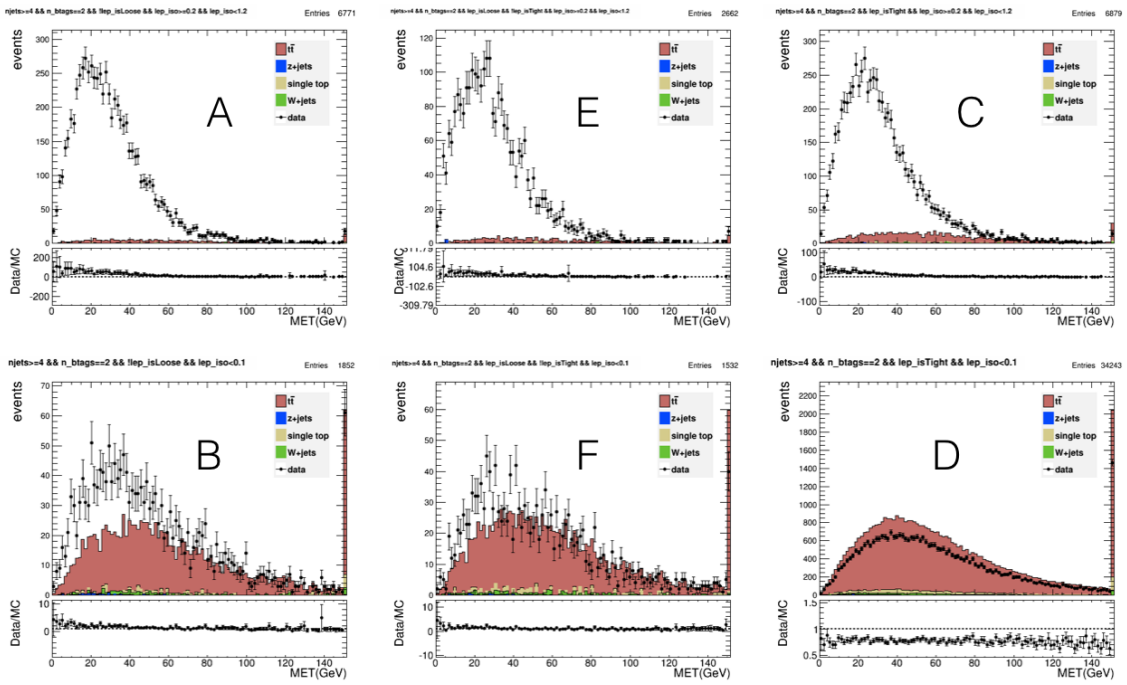

Figure 5.5: The missing transverse energy for $e+jets$ events in ABCD(EF) regions. The MC events are in solid color, and data events are in solid dots with error bars. The number of data events in each region is labeled as number of entries in upper right corner of each individual figure.

5.2 Data and MC Samples

5.2.1 Analysis Workflow

The reconstruction and the analysis of the data can be divided into three stages. The first stage selects and stores event candidates from samples satisfying single lepton triggers. Reconstructed lepton and b-jet identification information is added at the second stage. In the third stage, the final event selection, top quark reconstruction, and template fit are performed.

5.2.2 Data

The full 2012 LHC run dataset recorded by CMS detector is used. It represents proton proton collision at center of mass energy of 8 TeV with integrated luminosity of 19.7 ± 0.5 fb^{-1}. Only the data events that are recorded during the LHC runs that pass basic data quality monitoring (DQM) conditions are selected for the analysis. The list of DQM certified runs are provided by CMS, labeled by "lumi sections", which are the index of chunks of runs. The lumi-sections included in list of certified good runs provided in the following JSON file are included in the analysis.

- `Cert_190456-208686_8TeV_22Jan2013ReReco_Collisions12_JSON.txt`

To synchronize the trigger efficiency for Data and MC simulations, the following offline High Level Trigger (HLT) requirements are applied to both Data and MC.

- electron+jets channel: `HLT_Ele27_WP80_v*`
- muon+jets channel: `HLT_IsoMu24_eta2p1_v*`

The HLT filters the recorded data and only keep the data events that contains an isolated electron or muon that has pass basic lepton ID requirements.

5.2.3 Monte Carlo Simulation

This analysis requires large samples of fully simulated events to generate the different parts of the likelihood functions. Because the likelihood functions are built by reweighting Standard Model $t\bar{t}$ events, no special simulated samples are required. The samples used to model the signal and background functions, including the choice of generator and parton distribution functions, are listed in Table 5.3. All MC samples were generated in the official CMS Summer12 MC production campaign. In addition, all MC events are corrected using various scale factors to account for known discrepancies between data and simulation, as discussed in Section 6.5.

In order to build templates of likelihood functions all MC samples are normalized to the corresponding integrated luminosity of data. This is done given the number of simulated events generated and total cross sections of each individual process listed in Table 5.4. The expected number of events $\mathrm{N_{exp}}$ for each process following the equation:

$$\mathrm{N_{exp}} = \frac{\mathrm{N_{sel}}}{\mathrm{N_{gen}}} \mathcal{L}_{\mathrm{int}} \sigma \tag{5.2}$$

Where N_{sel} is number of selected MC events, N_{gen} is number of generated MC events, σ is the total cross section, and integrated luminosity $\mathcal{L}_{int} = 19.7$ fb^{-1}.

Table 5.3: Monte Carlo Simulation Information

Simulated Process	**MC Dataset**
$t\bar{t}$	`TT_8TeV-mcatnlo`
$t\bar{t}$ (alternative)	`TT_CT10_TuneZ2star_8TeV-powheg-tauola`
W+1 Jet	`W1JetsToLNu_TuneZ2Star_8TeV-madgraph`
W+2 Jets	`W2JetsToLNu_TuneZ2Star_8TeV-madgraph`
W+3 Jets	`W3JetsToLNu_TuneZ2Star_8TeV-madgraph`
W+4 Jets	`W4JetsToLNu_TuneZ2Star_8TeV-madgraph`
Z/γ+1 Jet	`DY1JetsToLL_M-50_TuneZ2Star_8TeV-madgraph`
Z/γ+2 Jets	`DY2JetsToLL_M-50_TuneZ2Star_8TeV-madgraph`
Z/γ+3 Jets	`DY3JetsToLL_M-50_TuneZ2Star_8TeV-madgraph`
Z/γ+4 Jets	`DY4JetsToLL_M-50_TuneZ2Star_8TeV-madgraph`
t (s-channel)	`T_s-channel_TuneZ2star_8TeV-powheg-tauola`
t (t-channel)	`T_t-channel_TuneZ2star_8TeV-powheg-tauola`
t (tW-channel)	`T_tW-channel-DR_TuneZ2star_8TeV-powheg-tauola`
$\bar{t}$ (s-channel)	`Tbar_s-channel_TuneZ2star_8TeV-powheg-tauola`
$\bar{t}$ (t-channel)	`Tbar_t-channel_TuneZ2star_8TeV-powheg-tauola`
$\bar{t}$ (tW-channel)	`Tbar_tW-channel-DR_TuneZ2star_8TeV-powheg-tauola`

Simulated Process	**Matrix Element Generator**	$N^{Events}_{Generated}$	σ (pb)
$t\bar{t}$	aMC@NLO	32852589	245.8
$t\bar{t}$ (alternative)	POWHEG	21560109	245.8
W+1 Jet	MADGRAPH	23038253	6662.8
W+2 Jets	MADGRAPH	33993463	2159.2
W+3 Jets	MADGRAPH	15507852	640.4
W+4 Jets	MADGRAPH	13326400	264.0
Z/γ+1 Jet	MADGRAPH	23994669	660.6
Z/γ+2 Jets	MADGRAPH	2345857	215.1
Z/γ+3 Jets	MADGRAPH	10655325	65.79
Z/γ+4 Jets	MADGRAPH	5843425	28.59
Z/γ+4 Jets	MADGRAPH	5843425	28.59
t (s-channel)	POWHEG	259176	3.79
t (t-channel)	POWHEG	3748155	56.4
t (tW-channel)	POWHEG	495559	11.1
$\bar{t}$ (s-channel)	POWHEG	139604	1.76
$\bar{t}$ (t-channel)	POWHEG	1930185	30.7
$\bar{t}$ (tW-channel)	POWHEG	491463	11.1

Table 5.4: Generator information and number of simulated events from Summer12 production of CMS.

5.3 Event Selection

The event selection for this analysis follows the Top PAG Run-1 selection recommendations [20]. To select top pair events in the lepton+jets channel, the candidate event is required to have a high p_T electron or muon and four or five high p_T jets. In order to reduce background events such as `W+jets` two of the jets must be tagged as b-jets. This analysis is based upon the particle flow objects defined in Section.4.1, and the selection of each individual physical object is described in the same chapter.

5.3.1 Cut-flow

The selection criteria are applied sequentially to both data and MC. The numbers of real and simulated events passing each step are summarized in Table 5.5. The final entry in the table lists the number selected events for which the kinematic reconstruction [as described in section 6.2.1] is successful. Only in the last step, the MC event rates have been corrected using scale factors to account for efficiency differences between data and MC for the lepton ID, trigger, and btagging requirements. Total number of events in simulation has been normalized to the integrated luminosity corresponding to the data using the total cross sections for each individual process as listed in Table 5.4.

The effectiveness of the selection criteria is illustrated in Figs. 5.6. The plot shows the normalized abundances of simulated $t\bar{t}$ and background events as functions of

	e+jets		μ+jets	
Selection Step	N_{Data}	N_{MC}	N_{Data}	N_{MC}
trigger	268293848	29318762	123122494	32845362
lepton	64361692	20186742	32845362	25208917
dilepton veto	62447916	19446044	74041500	24085598
$N_{jets} \geqslant 4$	254892	227859	222279	246025
$N_{btags} \geqslant 2$	56015	62788	55730	67974
$N_{jets} \leqslant 5$ and kin Reco	42923	47199	45321	51061

Table 5.5: Event yields after HLT trigger applied, contains one good lepton, not containing another lepton, has at least four selected jets, has at least two of the jets tagged as b jets, has no more than 5 selected jets while successfully being reconstructed. MC corrections such as trigger efficiency, pileup re-weighting etc have been applied in the last step of the cut flow. All MC events have been normalized to the same integrated luminosity as Data.

reconstructed $t\bar{t}$ mass before the application of the criteria. The sample is dominated by background from W+jets production. The plot on the right shows the same distributions after the application of the selection criteria. Clearly the signal $t\bar{t}$ is greatly enhanced with respect to the backgrounds.

Note that in the last step, we merged several background processes into a single template called *other backgrounds*, which includes single top production, Drell-Yan, and $t\bar{t}$ events that are not e+jets or mu+jets. On the other hand, we separate the W+Jets and QCD processes from the other backgrounds. The motivation is

that the processes included in the "other backgrounds" category are well modeled by MC simulations. By merging them together into one template we essentially fix the relative compositions among those processes according to the expected values given by MC. In contrast, according to many existing analysis, the W+Jets process is not very well modeled in the leading-order MC simulation used to generate the MC samples. For data driven QCD background estimate, the uncertainty of normalization is fairly large as discussed in Section 5.1.4. So we separate W+Jets process and QCD process from other backgrounds in the templates and later simultaneously fit for the normalization during the template fit.

After applying the selection criteria and reconstruction algorithm to the simulated data sets, semi-leptonic top pair events comprise 90% of the resulting sample. The relative fractions of events from signal and various backgrounds are listed in Table 5.6. The dominant background is “other backgrounds”.

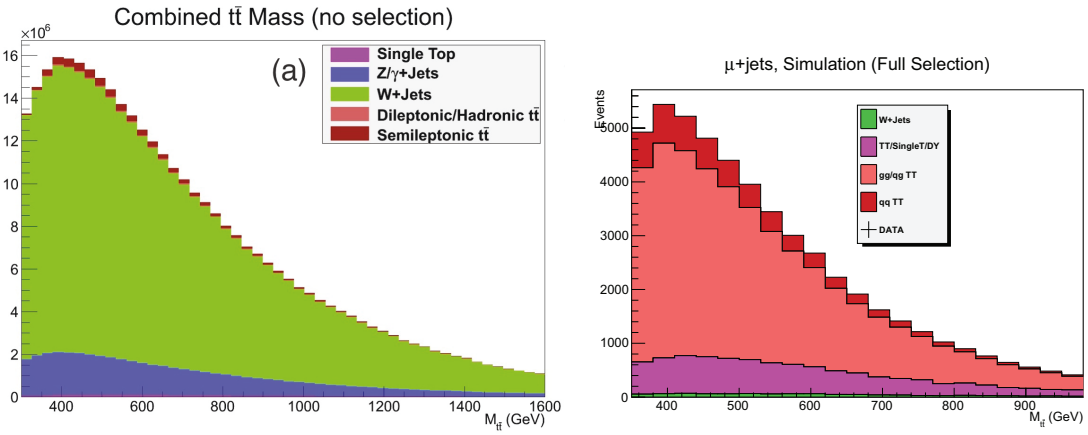

Figure 5.6: The $t\bar{t}$ invariant mass distributions of normalized signal and background Monte Carlo samples before event selection (top) and after event selection (bottom).

	e+jets		μ+jets	
Process	N_{MC}	Fraction	N_{MC}	Fraction
$q\bar{q} \to t\bar{t}$	5173	11.0	5510	10.8
$gg/qg \to t\bar{t}$	33824	71.7	36126	70.8
other backgrounds	6914	14.7	8530	16.7
W+Jets	764	1.6	894	1.8
QCD	522	1.1	NA	NA
Total	47199	100	51061	100

Table 5.6: Expected number of events and relative event composition after event selection and reconstruction, by counting of MC templates. Fractions are in terms of percent. Data driven QCD process is included in e+jets channel only. The normalization of QCD follows the discussion of Section.5.1.4

5.3.2 Control Plots

A set of control plots that compare MC and data distributions of several kinematic observables are shown in this section. All the plots are from events that passed all selection cuts, but before any further reconstruction quality cuts are made. It shows that the MC models the data distribution faily well.

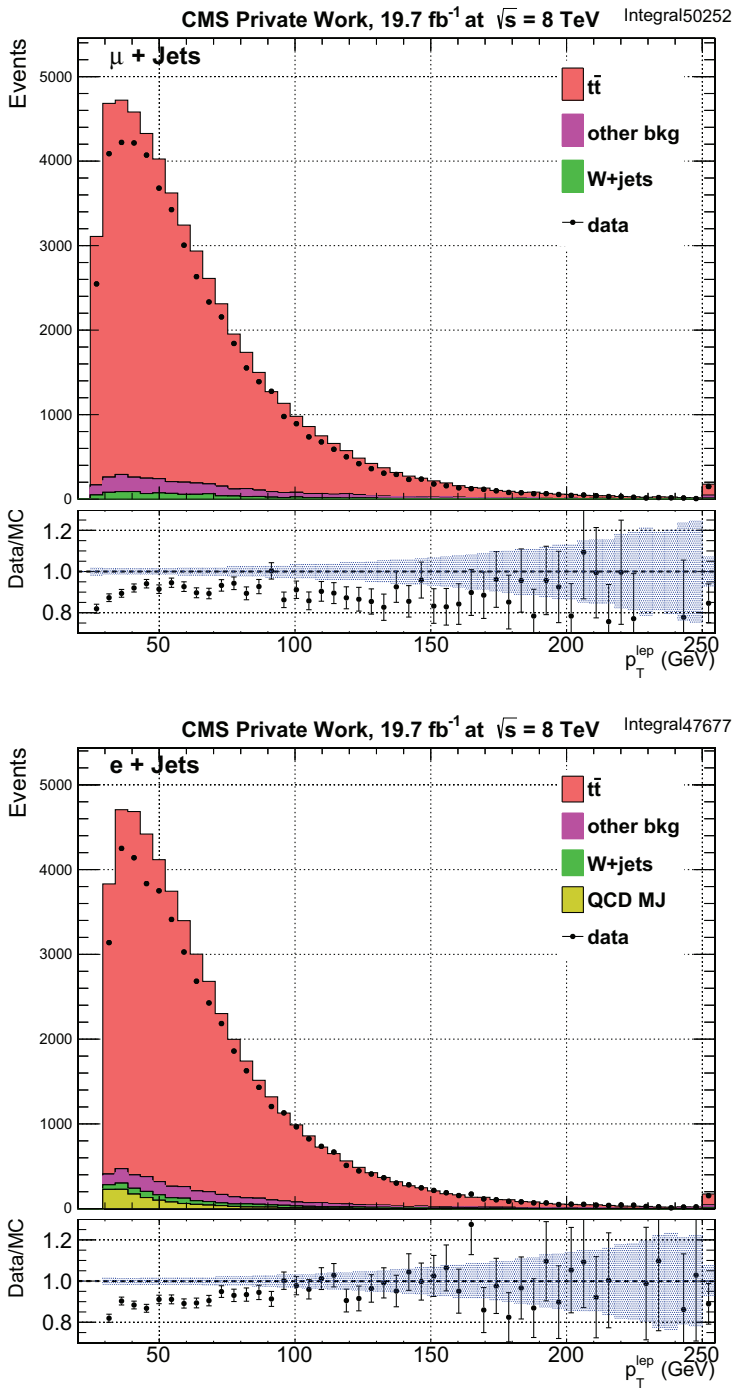

Figure 5.7: The e/μ p_T distributions of normalized signal and background Monte Carlo samples after event selection, for mu+jets channel (top) and e+jets(bottom).

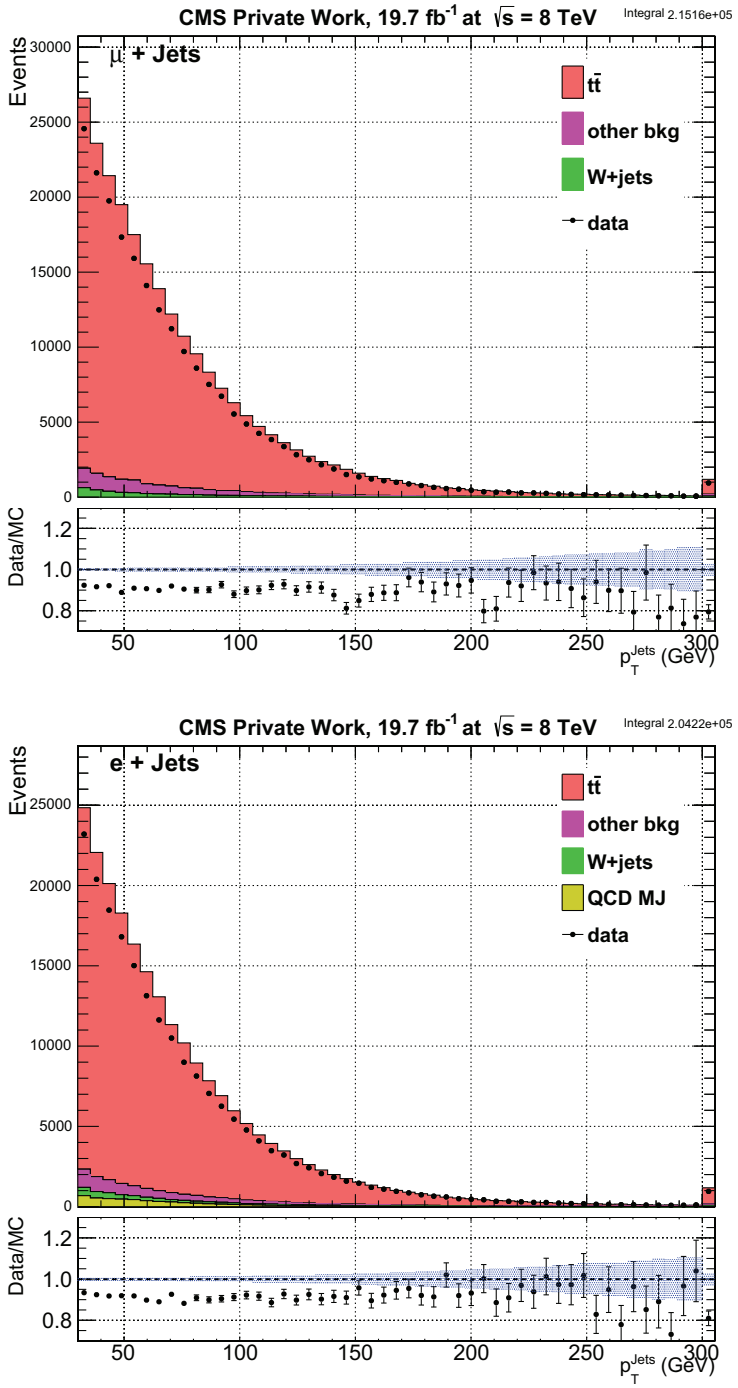

Figure 5.8: The jets p_T distributions of normalized signal and background Monte Carlo samples after event selection, for mu+jets channel (top) and e+jets(bottom).

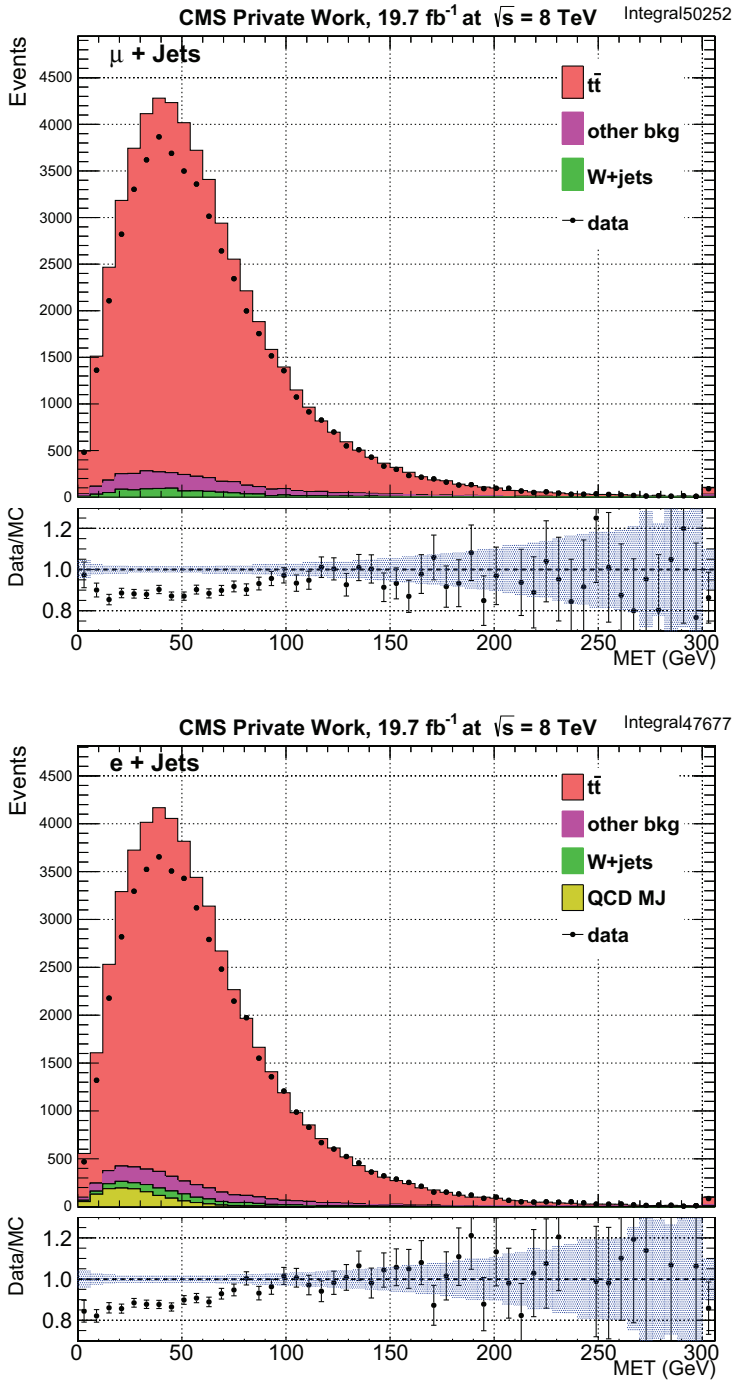

Figure 5.9: The MET distributions of normalized signal and background Monte Carlo samples after event selection, for *mu*+jets channel (top) and e+jets(bottom).

Chapter 6

Measurement of $\mathrm{t\bar{t}}$ Forawd-backward Asymmetry

In this chapter, we first introduce the empirical motivation and theoretical formulation of the template based A_{FB} measurement. Next, the method and result of kinematic reconstruction of $\mathrm{t\bar{t}}$ pairs from the momentum of observed final states is provided. Then, the details of the implementation of the template fit based on the maximal likelihood method is described. Afterwards, the systematic uncertainties in this measurement as well as the study of the sensitivity is described. Finally, the measurement results and discussion is provided.

6.1 Analysis Method for Template Based AFB Measurement

6.1.1 Motivation

The likelihood approach is based upon the observation that the angular distributions resulting from the s-channel dominated $q\bar{q}$ subprocess and from the t-channel dominated gg subprocess are quite distinct. Additionally, the gluon structure functions are "softer", more peaked a low x, than are the quark structure functions. Therefore, highly boosted $t\bar{t}$ pairs, those produced at large $x_{\rm F}$ or rapidity, are more likely to be $q\bar{q}$-produced and the boost direction is most likely to be the direction of the incident quark. To define the variables, we let x_1 and x_2 be the momentum fractions of the incident partons ordered so that the net boost is positive, $x_{\rm F} = x_1 - x_2 > 0$. The invariant mass of the $t\bar{t}$ pair, M, is then related to the momentum fractions, $M^2 = x_1 x_2 s$, where s is the square of the pp center-of-mass energy. The differential cross section for $t\bar{t}$ production is composed of three parts,

$$\frac{d^3\sigma}{dx_{\rm F} dM dc_*} = \frac{2M}{s\sqrt{x_{\rm F}^2 + 4M^2/s}} \left\{ \frac{d\sigma}{dc_*}(q\bar{q}; M^2) \left[D_q(x_1) D_{\bar{q}}(x_2) + D_q(x_2) D_{\bar{q}}(x_1) \right] + \frac{d\sigma}{dc_*}(gg; M^2) D_g(x_1) D_g(x_2) \right\} + \frac{d^3\sigma}{dx_{\rm F} dM dc_*}(\text{background}) \qquad (6.1)$$

where $x_{1,2} = \pm x_{\rm F} + \sqrt{x_{\rm F}^2 + 4M^2/s}$, $c_* \equiv \cos\theta^*$ and θ^* is angle between the initial state quark direction and the top direction in the $t\bar{t}$ cm frame , and where the tree-level

cross sections for $q\bar{q},\ gg \to t\bar{t}$ are

$$\frac{d\sigma}{dc_*}(q\bar{q}; M^2) = \frac{\pi\alpha_s^2}{9M^2}\beta\left[1 + \beta^2 c_*^2 + \left(1-\beta^2\right)\right] \tag{6.2}$$

and

$$\frac{d\sigma}{dc_*}(gg; M^2) = \frac{\pi\alpha_s^2}{48M^2}\beta\left[\frac{16}{1-\beta^2 c_*^2} - 9\right]\left\{\frac{1+\beta^2 c_*^2}{2} + (1-\beta^2) - \frac{(1-\beta^2)^2}{1-\beta^2 c_*^2}\right\} \tag{6.3}$$

and where the top quark velocity in the cm-frame is $\beta = \sqrt{1-4m_t^2/M^2}$. The gg subprocess produces a more forward-peaked cross section which provides the primary discriminant in the separation of the gg and qq subprocesses.

This study will consider events that can have extra jets which implies that the $t\bar{t}$ pairs can have non-zero transverse momenta . This is accommodated in NLO descriptions by using the Collins-Soper (CS) definition [24] of the production angle and by allowing the cross section to develop a (CS frame dependent) term corresponding to longitudinal gluon polarization,

$$\frac{d\sigma}{dc_*}(q\bar{q}; M^2) = K\frac{\pi\alpha_s^2}{9M^2}\beta\left[1 + \beta^2 c_*^2 + \left(1-\beta^2\right) + \alpha\left(1-\beta^2 c_*^2\right)\right] \tag{6.4}$$

where K is a normalization parameter and the average longitudinal polarization α is determined from a fit to a sample of generated events.

An asymmetric $q\bar{q}$ subprocess could be caused by several kinds of new physics that interfere with or augment the tree-level process [17, 30]. Most of these can be

characterized in leading order by a small generalization of the tree-level cross section,

$$\frac{d\sigma}{dc_*}(q\bar{q};M^2) = R\frac{\pi\alpha_s^2}{9M^2}\beta\Big\{1+\beta^2c_*^2+\left(1-\beta^2\right)+\alpha\left(1-\beta^2c_*^2\right) + 2\left[1+\frac{1}{3}\beta^2+(1-\beta^2)+\alpha\left(1-\frac{1}{3}\beta^2\right)\right]A_{\mathrm{FB}}^{(1)}c_*\Big\} \quad (6.5)$$

Note that the asymmetry is characterized by the slope of the linear term in c_* and is labelled with the superscript (1). Next-to-leading-order QCD corrections are expected [38] to produce an asymmetry of approximately 8%. A comparison of the ratio of the c_*-odd and even terms for the full NLO calculation and for the simple linear model given in Equation 6.5 with $A_{\mathrm{FB}}^{(1)} = 0.08$ is shown in Fig. 6.1. The black curves show the NLO calculation for three different values of M. The red curves show the linear model for the same values of M. It is clear that the linear model is fairly accurate at lower masses and is still a reasonable approximation at larger masses. A test of this hypothesis was performed by fitting the full NLO angular distribution generated by Powheg to the form given in equation 6.5 and by comparing the resulting linearized asymmetry with the asymmetry determined from counting the forward and backward top events. The results are listed in Table 6.1 for the full sample and for the 4-jet and 5-jet subsamples. Excellent agreement is observed.

The distributions in (M, c_*, x_F) for the gg and $q\bar{q}$ initial states can be visualized by considering a sample of $t\bar{t}(j)$ events generated with Powheg for pp collisions at $\sqrt{s} = 8$ TeV. Because an extra jet is allowed, there is also a substantial contribution from the process $qg \to t\bar{t}q$ which is larger in magnitude than the $q\bar{q}$ subprocess. The

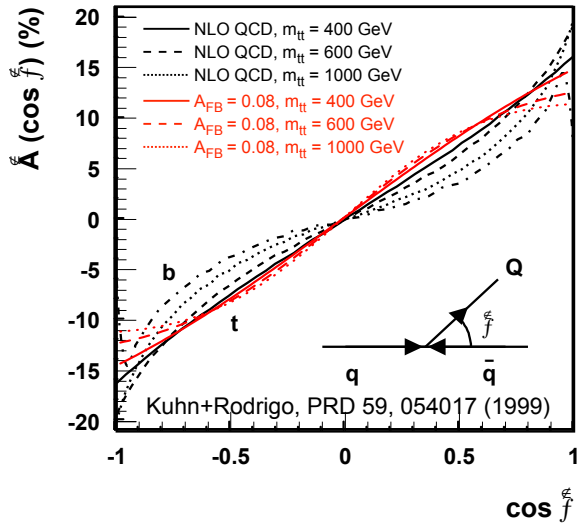

Figure 6.1: The ratio of the c_*-odd and even terms for the full NLO calculation and for the simple linear model given in equation 6.5 with $A_{\rm FB}^{(1)} = 0.08$. The black curves show the NLO calculation for three different values of M: 400 GeV (solid), 600 GeV (dashes), and 1000 GeV (dots). The black dash-dot curve corresponds to b quarks and should be ignored. The red curves show the linear model with $A_{\rm FB}^{(1)} = 0.08$ for the same masses.

mass, $\cos\theta^*$, and x_F distributions for the three subprocesses are shown in Fig. 6.2. Note that the gg and qg distributions are quite similar. Because the asymmetry for qg events is expected to be smaller than for $q\bar{q}$ events [38] (see also Table 6.4), the gg and qg subprocesses are combined into a single distribution function for the purpose of this work. The $q\bar{q}$ mass distribution is somewhat narrower than the others. The $q\bar{q}$ angular distribution is much flatter than the others due to t-channel pole that dominates the gg and qg cross sections. Of key importance, the x_F distribution of the $q\bar{q}$ events has a longer tail that helps to discriminate them and to correctly identify

Sample	A_{FB} (counting)	$A_{FB}^{(1)}$ (fitting)
All events	$+0.0356 \pm 0.0015$	$+0.0352 \pm 0.0013$
4 jets only	$+0.0903 \pm 0.0018$	$+0.0900 \pm 0.0016$
5 jets only	-0.0698 ± 0.0026	-0.0720 ± 0.0023

Table 6.1: The $q\bar{q} \to t\bar{t}$ forward-backward asymmetry as determined from a sample of Powheg NLO generated events by counting and by fitting to the linearized function.

the incident quark direction.

The result of taking the longitudinal direction of the $t\bar{t}$ pair in the lab frame as the quark direction is shown in Fig. 6.2(d). Defining N_C as the number of correct assignments and N_I as the number of incorrect assignments, the dilution factor D is plotted vs x_{F}, as defined below: $D = (N_C - N_I)/(N_C + N_I)$ The larger value of D means a higher accuracy of estimating initial quark direction. Note that it becomes large in the $q\bar{q}$ enriched region at large x_{F}. This is expected, as initial quark is more likely to carry more energy than anti quark in the case where the energy difference of them are large.

Because there can be "feed-down" from QCD processes that produce $t\bar{t}$ with more than one extra jet, we define the gg label to include events produced from the gg, qg, qq, $\bar{q}\bar{q}$, and $q_i\bar{q}_j$ (flavor $i \neq$ flavor j) subprocesses.

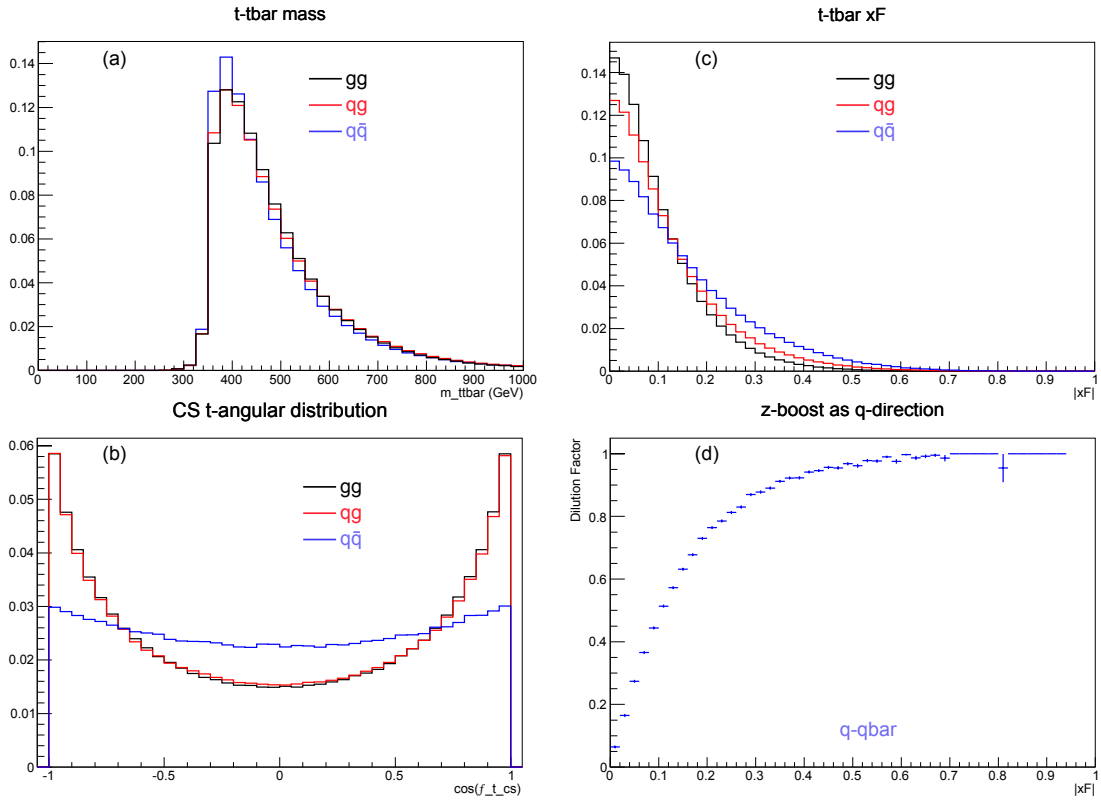

Figure 6.2: The mass (a), $\cos\theta^*$ (b), and $|x_F|$ (c) distributions for the subprocesses $gg/qg/q\bar{q} \to t\bar{t}(j)$. The result of taking the longitudinal direction of the $t\bar{t}$ pair in the lab frame as the quark direction is shown in panel (d). Defining N_C as the number of correct assignments and N_I as the number of incorrect assignments, the dilution factor $D = (N_C - N_I)/(N_C + N_I)$ is plotted vs x_F. Note that it becomes large in the $q\bar{q}$ enriched region at large $|x_F|$.

6.1.2 Analysis Scheme

It is possible to reconstruct the three key variables $x_{\rm r}$, $M_{\rm r}$, and $c_{\rm r}$ from lepton and 4(5)-jet final states. The sign of the lepton tags the top vs antitop direction. The direction of the pair along the beam axis can be taken as the likely quark direction for $q\bar{q}$. Integrating over the pair $p_{\rm T}$ (necessary only for the 5-jet cases), the data can be represented as a set of triplets in the reconstructed variables. The distribution function of the reconstructed variables can be expressed as a convolution of the cross section defined in equation 6.1 (where the $q\bar{q}$ cross section given by equation 6.5) with resolution and efficiency functions,

$$f(x_{\rm r}, M_{\rm r}, c_{\rm r}) = C \int dx_{\rm F} dM dc_* R(x_{\rm r}, M_{\rm r}, c_{\rm r}; x_{\rm F}, M, c_*) \varepsilon(x_{\rm F}, M, c_*) \frac{d^3\sigma}{dx_{\rm F} dM dc_*} \quad (6.6)$$

where C is a normalization constant, R is a "resolution function" that incorporates real detector resolution and parton shower effects, and ε is an efficiency function. The key point is that the linearity of the c_*-odd term in Equation 6.5 is not disturbed by the convolution and the linear coefficient $A_{FB}^{(1)}$ is unaffected. The linearity of the problem also allows the fitting function to be represented by a set of **parameter-independent** 3D histograms (also called "templates"). These histograms can be constructed by appropriate weighting and re-weighting of a large sample of fully digitized and reconstructed events from a simulation. The $gg(qg) \to t\bar{t}(X)$ and background distributions $f_{gg}(x_{\rm r}, M_{\rm r}, c_{\rm r})$ and $f_{\rm bk}^{j}(x_{\rm r}, M_{\rm r}, c_{\rm r})$ can be extracted directly from fully

simulated samples by binning in the reconstructed variables. The various parts of the $q\bar{q}$ distribution can be constructed by re-weighting simulated events using generator-level variables to generate the weights and binning in reconstructed variables.

To illustrate the re-weighting procedure, let's assume that we have a sample of fully simulated and reconstructed $q\bar{q} \to t\bar{t}$ events. If the simulation is tree-level, it generates the symmetric cross section [1] given in equation 6.4 and we can create one 3D histogram or template simply by binning the events in the reconstructed variables. We call this symmetric distribution $f_{\rm qs}(x_{\rm r}, M_{\rm r}, c_{\rm r}, Q)$ and normalize it by the total number of events. We can generate the asymmetric distribution by applying the following weight to each simulated event using generator-level quantities,

$$w_{\rm a}(M^2, c_*) = 2\frac{1 + \frac{1}{3}\beta^2 + (1-\beta^2) + \alpha(1 - \frac{1}{3}\beta^2)}{1 + \beta^2 c_*^2 + (1-\beta^2) + \alpha\,(1 - \beta^2 c_*^2)} c_* \tag{6.7}$$

and then binning the weighted events in the reconstructed quantities to produce the asymmetric distribution $f_{\rm qa}(x_{\rm r}, M_{\rm r}, c_{\rm r}, Q)$ with the same normalization as used for the symmetric distribution. A simple three parameter likelihood fit to the real data would follow from the following four histograms,

$$\begin{aligned} f(x_{\rm r}, M_{\rm r}, c_{\rm r}) = &\sum_j R^j_{\rm bk} f^j_{\rm bk}(x_{\rm r}, M_{\rm r}, c_{\rm r}) + \left(1 - \sum_j R^j_{\rm bk}\right)\Big\{(1 - R_{q\bar{q}})\, f_{gg}(x_{\rm r}, M_{\rm r}, c_{\rm r}) \\ &+ R_{q\bar{q}}\left[f_{\rm qs}(x_{\rm r}, M_{\rm r}, c_{\rm r}) + A^{(1)}_{\rm FB} f_{\rm qa}(x_{\rm r}, M_{\rm r}, c_{\rm r})\right]\Big\} \end{aligned} \tag{6.8}$$

[1] Due to the symmetrized weighting described below, NLO simulations generating asymmetric distributions can also be used.

where the background fractions $R^j_{\rm bk}$, $q\bar{q}$ fraction $R_{q\bar{q}}$, and asymmetry $A^{(1)}_{\rm FB}$ are allowed to float. Note that the backgrounds can be summed into a single distribution and represented by a single parameter or they can be subdivided into several parts represented by several fraction parameters. This analysis should be done in bins or slices of $M_{\rm r}$ so that it is really a series of 3-parameter fits and extracts $A^{(1)}_{\rm FB}(M)$. Due to the limited statistics available in the 2012 data, mass binning of the parameters has not yet been implemented. Note that this technique automatically accounts for resolution, dilution, migration, and acceptance effects so long as they are correctly modeled in the simulation.

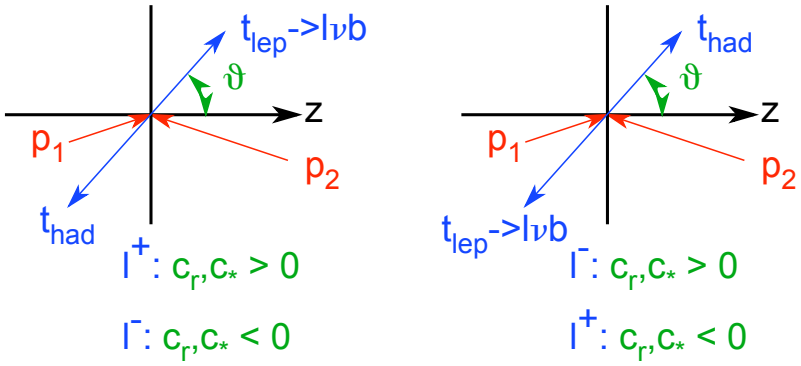

Figure 6.3: The $t\bar{t}$ center-of-mass frame where system is presumed to be boosted in the direction of the proton with momentum vector $\vec{p}_1$ which determines the positive direction using the Collins-Soper definition of the production angle.

The acceptance for the moving $t\bar{t}$ pairs has a small subtlety that can be exploited to help distinguish the signal from the backgrounds. The $t\bar{t}$ center-of-mass frame is shown in Fig. 6.3. The system is presumed to be boosted in the direction of the

proton with momentum vector $\vec{p}_1$ and it determines the positive direction using the Collins-Soper definition of the production angle. It is possible that the leptonically decaying t or $\bar{t}$ is produced in the "forward" direction as shown on the left-hand side of the figure. If the leptonic top decays to a positively (negatively) charged lepton, the sign of c_* and c_r are positive (negative). Assuming that the detector locally accepts and reconstructs positive and negative charges with the same efficiency and resolution, the acceptance and resolution for the two cases are the same. Similarly, the leptonically decaying t or $\bar{t}$ can be produced in the "backward" direction as shown on the right-hand side of the figure. Again, the sign of the lepton determines two cases that have the same efficiency and resolution. However, the efficiency and resolution for the left and right cases are not in general the same. A non-zero value of $A_{\rm FB}^{(1)}$ when combined with the acceptance difference would produce an asymmetry in the number of positively and negatively charged leptons observed in the sample. The approach described above merges the two $c > 0$ and the two $c < 0$ cases to create truly symmetric and antisymmetric functions and cannot describe this effect. It is, however, possible to split the problem by lepton charge instead. This modifies equation 6.8 as follows,

$$f(x_{\rm r}, M_{\rm r}, c_{\rm r}, Q) = \sum_j R_{\rm bk}^j f_{\rm bk}^j(x_{\rm r}, M_{\rm r}, c_{\rm r}, Q) + \left(1 - \sum_j R_{\rm bk}^j\right)\Big\{(1 - R_{q\bar{q}})\, f_{gg}(x_{\rm r}, M_{\rm r}, c_{\rm r}, Q) + R_{q\bar{q}}\left[f_{\rm qs}(x_{\rm r}, M_{\rm r}, c_{\rm r}, Q) + A_{\rm FB}^{(1)} f_{\rm qa}(x_{\rm r}, M_{\rm r}, c_{\rm r}, Q)\right]\Big\} \tag{6.9}$$

where the functions are built using the lepton charge Q information. Because we

desire to symmetrize and anti-symmetrize the $q\bar{q}$ fitting functions, the CP symmetries shown in Fig. 6.3 can be exploited to use each simulated event twice. For each simulated event with lepton charge Q, generated angle c_*, and reconstructed angle c_r, the distribution functions for the coordinate $(x_\mathrm{r}, M_\mathrm{r}, c_\mathrm{r}, Q)$ and $(x_\mathrm{r}, M_\mathrm{r}, -c_\mathrm{r}, -Q)$ can be accumulated where the weights for the latter point assume a generated angle of $-c_*$. The new distributions functions don't have definite symmetry until they are combined over lepton charge Q. Due to the double-weighting, **the charge-summed distribution functions have definite symmetry (or antisymmetry) even if the original unweighted simulation was not c_*-symmetric.** The function f_{gg} describes the distribution of gg and qg events. The gg events are used symmetrically with 0.5 event accumulated in each of the $(c_\mathrm{r}, Q)/(-c_\mathrm{r}, -Q)$ bin pairs. The qg events are not symmetrized so that the final distribution function reflects their expected FB asymmetry. The advantage of this formulation is that it can describe a charge asymmetry arising from the combination of a non-zero $A_\mathrm{FB}^{(1)}$ and an asymmetric acceptance. More importantly, it accommodates the charge-asymmetric background which has significant contributions from W+jet events and single top events. The accepted charge ratios of fully simulated and reconstructed semi-muonic top pair candidates from various signal and background processes are listed in Table 6.2. It is clear that including charge information increases the background discrimination power of the fitting procedure.

Table 6.2: The sample fractions and lepton charge ratios for various signal and background processes from samples of fully simulated and reconstructed Powheg and MadGraph5 semi-muonic events. The samples and selection criteria are described in Sections 5.2-5.3.

Process	Generator	Sample Fraction	$N(\mu^+)/N(\mu^-)$
$q\bar{q} \to t\bar{t}(\mathrm{j}) \to \mu + 4(5)\mathrm{j}$	Powheg	0.062	1.000±0.014
$gg(qg) \to t\bar{t}(\mathrm{j}) \to \mu + 4(5)\mathrm{j}$	Powheg	0.731	0.998±0.004
$pp \to t\bar{t}(\mathrm{j}) \to$ hadronic/dileptonic	Powheg	0.106	1.018±0.011
$W +$ jets	Madgraph5	0.037	1.408±0.026
single top	Powheg	0.056	1.260±0.019
$Z/\gamma +$ jets	MadGraph5	0.009	1.045±0.039

6.2 Kinematic Reconstruction of t-tbar events

Top quarks (anti-quarks) are not directly observable, as they decay to a W+(W-) boson and a bottom quark (anti-quark) almost instantly. In this thesis, the events of l+4/5 jets are analyzed. In order to apply the analysis method described in previous section, the momentum of top quarks and anti-quarks are required to be reconstructed accurately from the observed final states. Two challenges arise in this process: first is to determine the correct combination of final states into two parent top quarks; second is to determine the un-measured longitudinal momentum of neutrino from top quark decay. A kinematic reconstruction algorithm is applied to find the optimal combination of final states and to adjust the momentum of final states for improving the reconstruction resolution.

6.2.1 Method

Real and simulated events containing a charged lepton and four or five jets are reconstructed by minimizing a likelihood estimator that is a function of the neutrino longitudinal momentum p_ν^z and five momentum scaling factors λ_j. For each final state particle assignment hypothesis, the 4-vectors of the charged particles are momentum-scaled as bellow,

$$\begin{aligned} \boldsymbol{p_{\ell}} &= (\lambda_1|\vec{p}_\ell|, \lambda_1\vec{p}_\ell) & \boldsymbol{p_{b\ell}} &= \left(\sqrt{m_b^2 + \lambda_2^2|\vec{p}_{b\ell}|^2}, \lambda_2\vec{p}_{b\ell}\right) \\ \boldsymbol{p_{h1}} &= (\lambda_3|\vec{p}_{h1}|, \lambda_3\vec{p}_{h1}) \quad \boldsymbol{p_{h2}} = (\lambda_4|\vec{p}_{h2}|, \lambda_4\vec{p}_{h2}) & \boldsymbol{p_{bh}} &= \left(\sqrt{m_b^2 + \lambda_5^2|\vec{p}_{bh}|^2}, \lambda_5\vec{p}_{bh}\right) \end{aligned} \tag{6.10}$$

The neutrino is constructed from the missing transverse momentum after scaling,

$$\begin{aligned}\vec{p}_{\nu}^{\perp} &= -\left[\lambda_1\vec{p}_{\ell}^{\perp} + \lambda_2\vec{p}_{b\ell}^{\perp} + \lambda_3\vec{p}_{h1}^{\perp} + \lambda_4\vec{p}_{h2}^{\perp} + \lambda_5\vec{p}_{bh}^{\perp} + \vec{p}_{\text{recoil}}^{\perp}\right] \\ \boldsymbol{p_{\nu}} &= \left(\sqrt{(p_{\nu}^{z})^2 + |p_{\nu}^{\perp}|^2}, \vec{p}^{\perp}\nu, p_{\nu}^{z}\right)\end{aligned} \tag{6.11}$$

where $\vec{p}_{\text{recoil}}^{\perp}$ is the total transverse momentum of the event after the removal of the five particles. The six scaled and reconstructed four-vectors are used to calculate the following four invariant masses to be used in the likelihood function,

$$\begin{aligned} q_W^2[\ell] &= (\boldsymbol{p_{\ell}} + \boldsymbol{p_{\nu}})^2 \qquad q_t^2[\ell] = (\boldsymbol{p_{\ell}} + \boldsymbol{p_{\nu}} + \boldsymbol{p_{b\ell}})^2 \\ q_W^2[h] &= (\boldsymbol{p_{h1}} + \boldsymbol{p_{h2}})^2 \quad q_t^2[h] = (\boldsymbol{p_{h1}} + \boldsymbol{p_{h2}} + \boldsymbol{p_{bh}})^2 \end{aligned} \tag{6.12}$$

where the invariant masses of the hadronic W boson (top quark) are functions of the parameters $\lambda_3, \lambda_4(, \lambda_5)$, and the invariant masses of the leptonic states depend upon all six parameters. These are combined in a likelihood function that constrains and tests the consistency of the masses with the hypothesis, the consistency of the momentum scaling factors with unity, and the consistency of the b-jet identification with the measured b-tag discriminators d_j,

$$\begin{aligned}\chi^2 = &-2\sum_{i=\ell,\text{h}} \ln\left\{\frac{C}{(q_t^2[i]-m_t^2)^2 + m_t^2\Gamma_t^2} \cdot \frac{(m_t^2 - q_W^2[i])^2(2m_t^2 + q_W^2[i])}{(q_W^2[i]-m_W^2)^2 + m_W^2\Gamma_W^2}\right\} + \sum_{j=1}^{5}\frac{(\lambda_j - 1)^2}{\sigma_j^2} \\ &- 2\ln\left\{g_b(d_{b\ell})g_b(d_{bh})g_q(d_{h1})g_q(d_{h2})\right\}\end{aligned} \tag{6.13}$$

where C is a constant normalization parameter, σ_j is the fractional momentum resolution for particle j (assumed to be 0.1 for jets and 0.03 for muons), $g_b(d)$ are discriminator distribution functions for b-jets from t decays, and $g_q(d)$ are the discriminator

distribution function for light quark jets from W decays. In events with an extra jet, a discriminator distribution function $g_{\text{other}}(d)$ for jets produced in association with $t\bar{t}$ pairs is also used. These discriminator distribution functions are pictured in Fig. 6.4 to illustrate the distinction they provide.

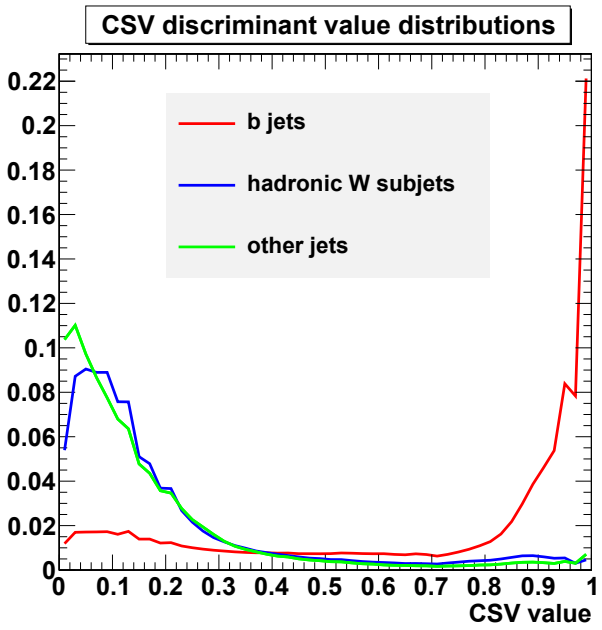

Figure 6.4: The CSV discriminator distribution functions used in the kinematic fit to distinguish b jets [red] from hadronic W subjets [blue] and incidental extra jets [green].

The minimization procedure is started assuming that all momentum scaling factors are unity, $\lambda_j = 1$. With this assumption, the leptonic W mass constraint has, in general, two solutions for p_ν^z. To avoid local minima, both solutions are used as starting points for the minimization procedure, and the resulting fit with the smallest χ^2 is kept. This function was designed to constrain the top masses with simple

Lorentzian functions that include widths and the W masses to the slightly modified and correlated Lorentzian shapes expected for $t \to Wb$ decays. In actual fact, the presence of the momentum scaling factors allows the best fit masses to converge to m_t and m_W in all cases. In both data and simulation, we use the accepted value of the W mass, $m_W = 80.4$ GeV. We assume $m_t = 172.5$ GeV () and $m_t = 173.3$ GeV in simulation and data respectively.

The fitting procedure is performed on all possible jet orderings for each of the topologies used in the analysis and the configuration with the smallest value of χ^2 is retained.

6.2.2 Performance of kinematic reconstruction

Based on the reconstructed top and anti-top momenta, the kinematic observables that are used for the $A_{\rm FB}$ measurement, ($x_{\rm r}$, $M_{\rm r}$, $c_{\rm r}$), can be constructed. The same set of variables can be constructed from the momenta of generated $\rm t\bar{t}$ pairs, using the generator truth information. To evaluate the performance of the kinematic reconstruction, we compare the distribution of reconstructed kinematic variables with the generated ones, using the full set of simulated $\rm t\bar{t}$ events. Note that generated $x_{\rm F}$, M are defined for all $\rm t\bar{t}$ process regardless of its production mechanism, whereas generated c_* is only well defined for $q\bar{q} \to t\bar{t}$ process. As a result, the comparison of generated c_* and reconstructed c_r is based on $q\bar{q} \to t\bar{t}$ simulated events, while $x_{\rm F}$, M is based on all semileptonic $\rm t\bar{t}$ events.

The sensitivity and correctness of A_{FB} measurement in this thesis rely on two performance metrics of kinematic reconstruction. The first metric is the resolution of reconstructed kinematic observables, which can be evaluated by plotting the residual such as $c_{\mathrm{r}} - c_{*}$. A smaller variance of residual indicates a more accurate reconstruction of $\mathrm{t\bar{t}}$ momentums. The second metric is the linearity of reconstructed versus generated observables. This can be checked by either the mean of the residuals, or the 2D plot.

The reconstruction of the kinematic variables works reasonably well. The correlations between the generated variables (x_{F}, M, c_{*}) and the reconstructed variables (x_{r}, M_{r}, c_{r}) are shown in Fig. 6.5. Linear behavior with unit slopes is observed over the range of available statistics. The 2D plot also shows evidence of quark direction sign error as expected from Fig. 6.5(d).

We also further check the effectiveness of top quark pairs reconstruction by plotting the residuals of x_F, $M_{t\bar{t}}$, c_{*}, shown in Fig. 6.6. It shows that the reconstruction has small bias for all three variables and reasonably good reconstruction resolution.

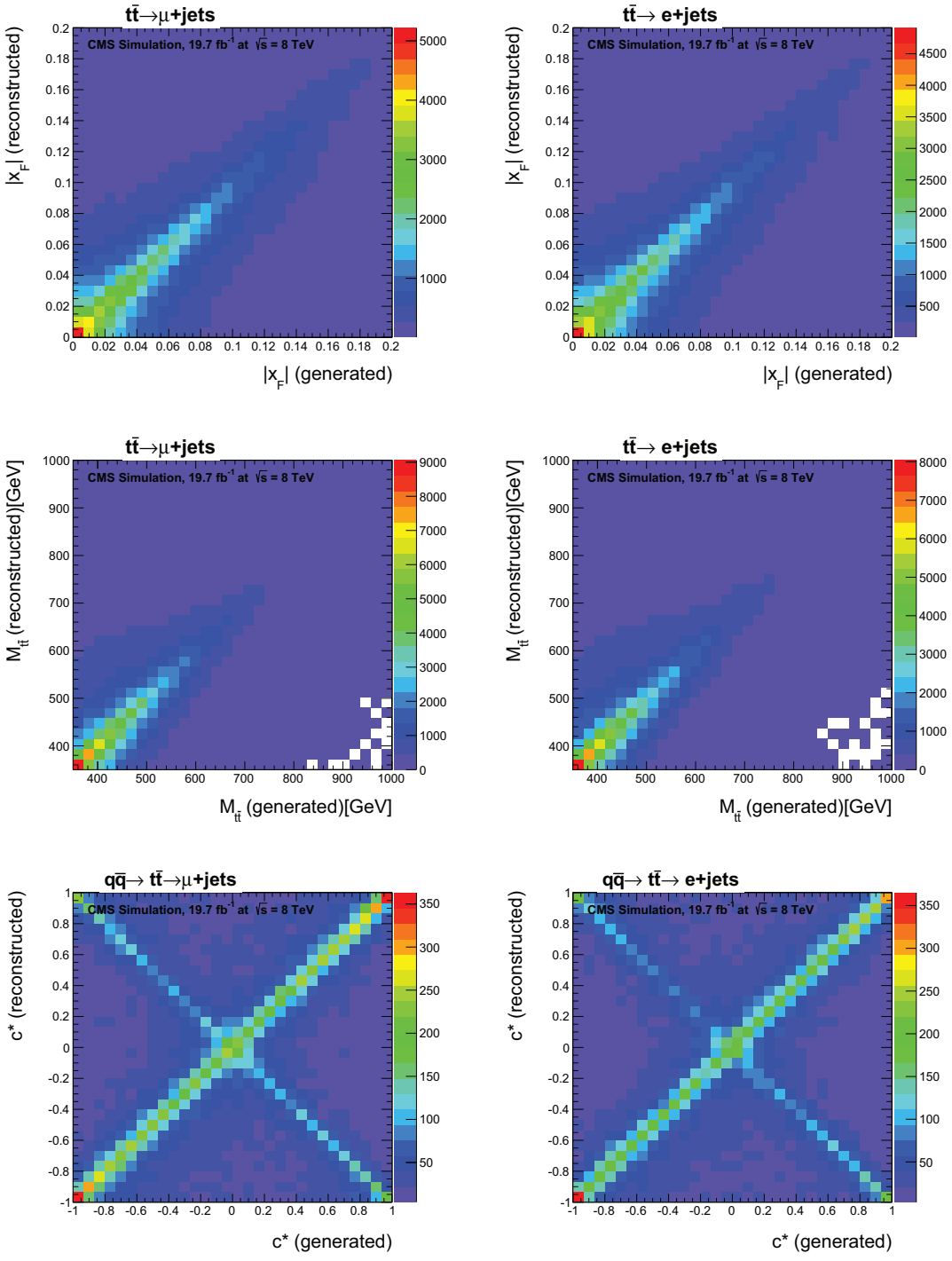

Figure 6.5: The correlations of the generated/reconstructed variable pairs x_F/x_{r}, M/M_{r} and c_*/c_{r} for a sample of simulated $t\bar{t}$ events. The figures at the left are from μ+jets channel, at right are e+jets channel.

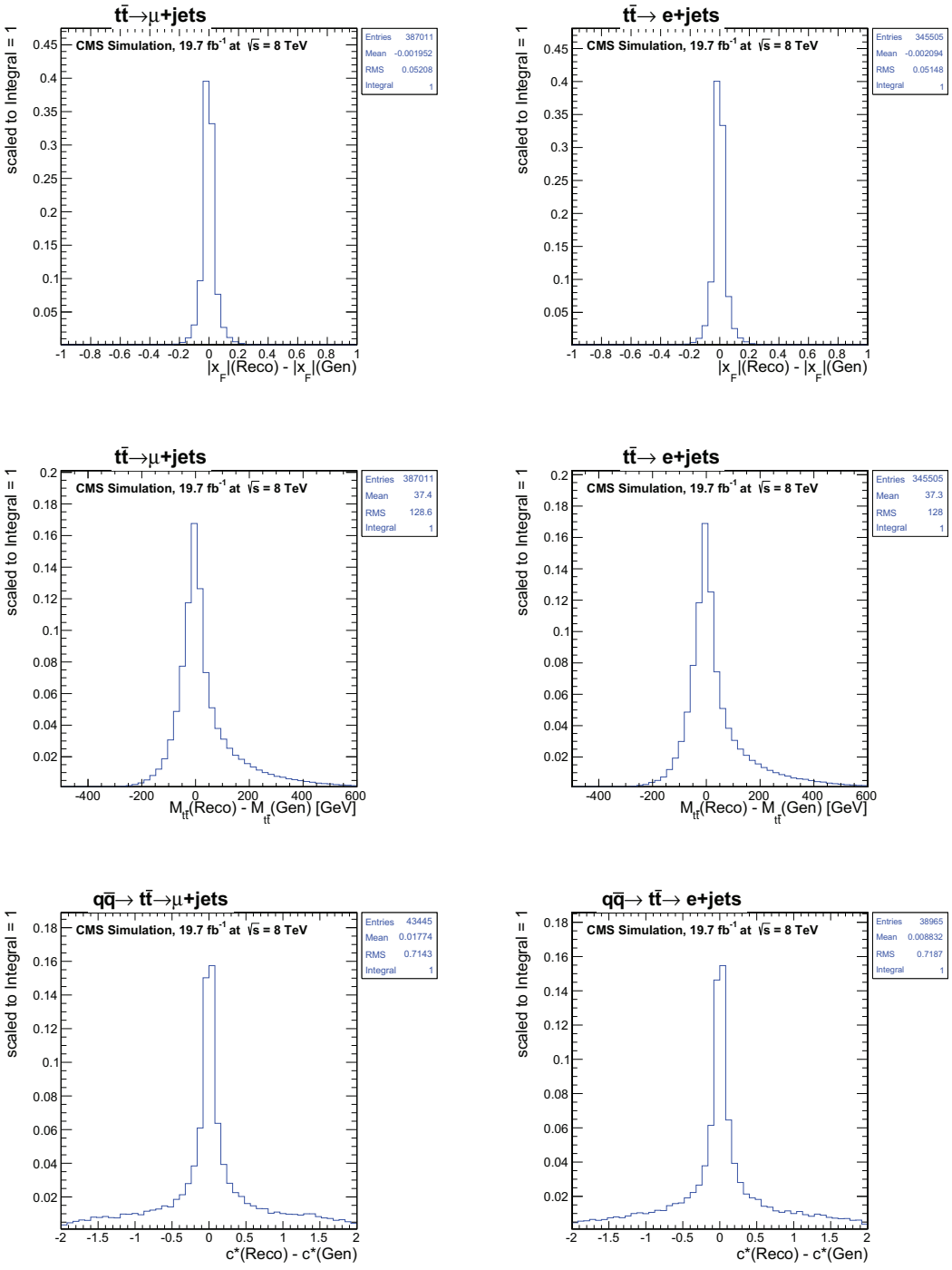

Figure 6.6: The residuals of the generated/reconstructed variable pairs x_F/x_{r}, M/M_{r} and c_*/c_{r} for a sample of simulated $t\bar{t}$ events. The left figures are from μ+jets channel, and right ones are e+jets channel.

6.3 Template Fitter

The goals of this analysis are to simultaneously measure Forward-backward asymmetry ($A_{\rm FB}$) and the fraction of $q\bar{q}$ initiated $t\bar{t}$ events, $R_{q\bar{q}}$. We perform the parameter estimation by doing a binned maximum likelihood fit using the 3 dimensional templates adapted from Eq. [6.8].

6.3.1 THETA Package

We use the THETA Package for the template fit[42]. The main idea is assuming that the event populations in every bin of (c_r,M_r and $|x_r|$) are described by Poisson distributions. The likelihood function is then the product of the independent Poisson distributions:

$$p(\boldsymbol{n}^{Data}|\boldsymbol{\theta}) = \prod_i Poisson(n_i^{Data}|\lambda_i(\boldsymbol{\theta})) \tag{6.14}$$

where $\boldsymbol{n}^{Data} = (n_1, n_2, ..., n_i)$ represent the number of events in each bin. λ_i is the expected number of events in bin i, which is given by the sum of signal and background events in that bin:

$$\lambda_i(\boldsymbol{\theta}) = n(x_{\rm r}, M_{\rm r}, c_{\rm r}|\boldsymbol{\theta}) = \sum_j n^j_{\rm bk}(x_{\rm r}, M_{\rm r}, c_{\rm r}|\boldsymbol{\theta}) + n_{gg}(x_{\rm r}, M_{\rm r}, c_{\rm r}|\boldsymbol{\theta}) + n_{\rm q\bar{q}}(x_{\rm r}, M_{\rm r}, c_{\rm r}|\boldsymbol{\theta}) \tag{6.15}$$

Here $\boldsymbol{\theta}$ represents all parameters, including the parameters of interest and additional nuisance parameters.

There are two types of nuisance parameters in the fit. First type is the one that controls relative compositions of individual background processes, including R_{WJets},R_{other} and R_{QCD} as defined in Equation. 6.9. The second type of nuisance parameters are introduced for the evaluation of systematic uncertainties, summarized in Section. 6.5.

We measure the parameters of interest together with the nuisance parameters by maximizing the total likelihood for the measured data distribution. In Eq. 6.16, the expected number of events for bin i is the sum of signal and background templates. Depending on the choice of $\boldsymbol{\theta}$, the templates have different shapes and normalizations. The parameter dependence is modeled by template morphing. For every parameter, for instance A_{FB}, three versions of templates are provided, corresponding to $A_{\mathrm{FB}} = -1, 0, +1$. Note for this parameter, A_{FB} templates are only provided for $n_{q\bar{q}}$ as it is the only process that depend on A_{FB} in our model. Then during the fit, for each value of A_{FB}, the corresponding likelihood which is a function of A_{FB} is calculated given expected number of events for every bin. For simplicity, let's focus on the i'th bin, denote as $n_{q\bar{q}}(A_{\mathrm{FB}})$. This number is derived from interpolation of three set of numbers for the same bin, $n_{q\bar{q}}(A_{\mathrm{FB}}) = -1, 0, +1)$. In Theta, the cubic spline is used for interpolation with $|\theta| < 1$ and linear spline for $|\theta| > 1$.

There is another way to model the change of expected number of events by introducing a parameter representing event rate. In our case, we introduce a nuisance parameter c_{lumi} for the integrated luminosity. This parameter models the global nor-

malization for all processes. Now the expected number of events for every bin looks like this:

$$\lambda_i(\boldsymbol{\theta}) = n(x_{\mathrm{r}}, M_{\mathrm{r}}, c_{\mathrm{r}}|\boldsymbol{\theta}) = c_{lumi}\left[\sum_j n_{\mathrm{bkg_j}}(x_{\mathrm{r}}, M_{\mathrm{r}}, c_{\mathrm{r}}|\boldsymbol{\theta}) + n_{gg}(x_{\mathrm{r}}, M_{\mathrm{r}}, c_{\mathrm{r}}|\boldsymbol{\theta}) + n_{\mathrm{q\bar{q}}}(x_{\mathrm{r}}, M_{\mathrm{r}}, c_{\mathrm{r}}|\boldsymbol{\theta})\right] \tag{6.16}$$

Finally, the likelihood also includes the proper prior distribution for all parameters. Denote the prior distribution for parameter θ_j to be $\pi(\theta_j)$, the likelihood given data distribution become:

$$L(\boldsymbol{n}^{Data}|\boldsymbol{\theta}) = \prod_i Poisson(n_i^{Data}|\lambda_i(\boldsymbol{\theta}))\prod_j \pi(\theta_j) \tag{6.17}$$

And the measured parameter values $\hat{\boldsymbol{\theta}}$ are taken as the maximal likelihood estimator.

$$\hat{\boldsymbol{\theta}} = argmax_{\boldsymbol{\theta}} L(\boldsymbol{n}^{Data}|\boldsymbol{\theta}) \tag{6.18}$$

In practice we choose to minimize the negative log-likelihood (NLL) below:

$$NLL(\boldsymbol{n}^{Data}|\boldsymbol{\theta}) = -\left[\sum_i Poisson(n_i^{Data}|\lambda_i(\boldsymbol{\theta}) + \sum_j \pi(\theta_j)\right] \tag{6.19}$$

6.3.2 Template binning

Since we perform a binned likelihood fit based on 3 dimensional templates, we studied the optimal binning for our templates. On one hand we chose the binning such that every bin has a sufficient number of events, on the other hand there are

more bins in regions of phase space where signal and background distributions are more statistically distinguishable.

In addition, we choose to limit the phase space of events to the region where $M_{t\bar{t}} < 980\,\text{GeV}$ for two reasons. The first reason is the MC templates beyond this kinematic region have many fewer events passing all selections which results in poor modeling of expected data distributions. The second reason is that the top and anti-top quarks in events with $M_{t\bar{t}} > 980\,\text{GeV}$ tend to be boosted, causing their decay products, especially on the hadronic decay side, to be merged into fewer jets. Because our kinematic re-construction algorithm assumes a fully resolved event topology, this causes poorly reconstructed $t/\bar{t}$ momenta.

In the end, the templates are constructed from un-binned simulated events with the following binning:

- $c*$: [-1.0,1.0], every 0.1
- $M_{t\bar{t}}$: [350,980], every 30 GeV
- $|x_F|$: [0,0.02,0.04,0.06,0.08,0.1,0.12,0.14,0.16,0.18,0.2,0.22,0.26,0.3,0.6]

The Fig.[6.7] and Fig.[6.8] shows the projections of templates in all three dimensions for signal and background processes. The clear distinction of various process can be seen which suggest the potential statistical power of the template fit.

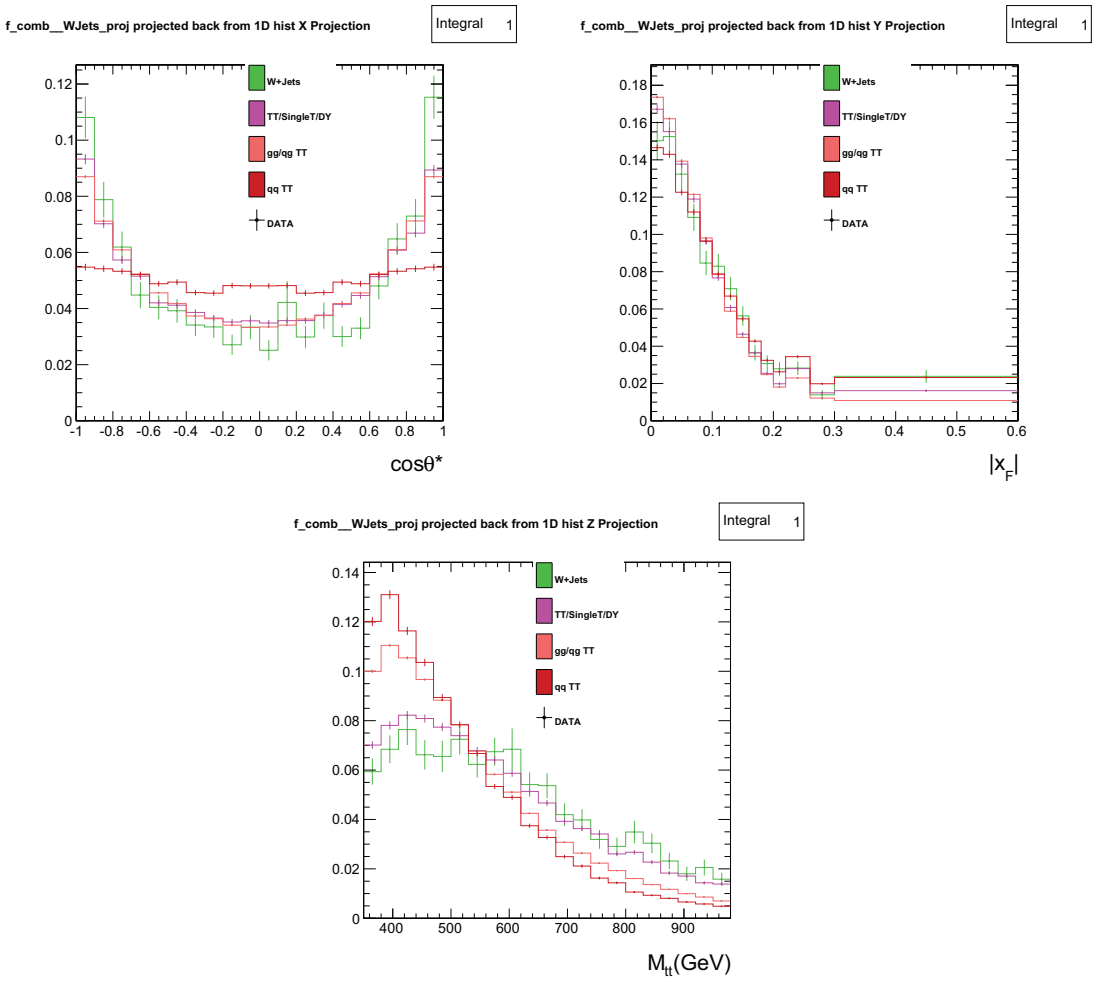

Figure 6.7: The profile of templates of all processes projected to each of the three dimensions for $\mu + jets$ channel.

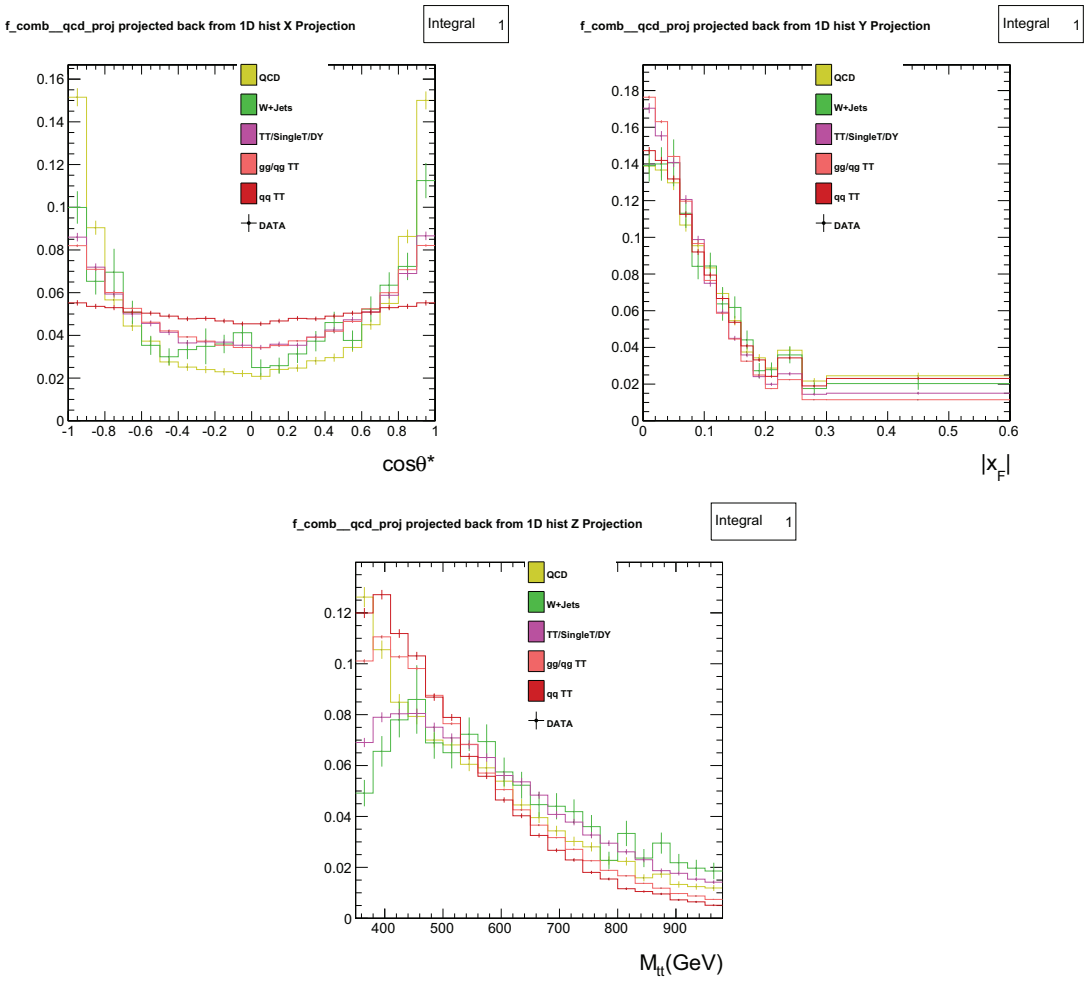

Figure 6.8: The profile of templates of all processes projected to each of the three dimensions for $e + jets$ channel.

Although the original templates are 3 dimensional and all three kinematic variables are fully correlated, we unrolled the templates into 1 dimension with arbitrary ordering of the bins so we can use Theta to do the template fit for us. The Fig.[6.9] shows the unrolled 1D distribution for the combined simulated events for $\mu + jets$ with $Q > 0$ for illustration purpose. Note this 1-D template is the one that is ac-

tually used by the fitter, and the number of events in each bin corresponds to λ_i in Eq. [6.17], which is the expected number of observations.

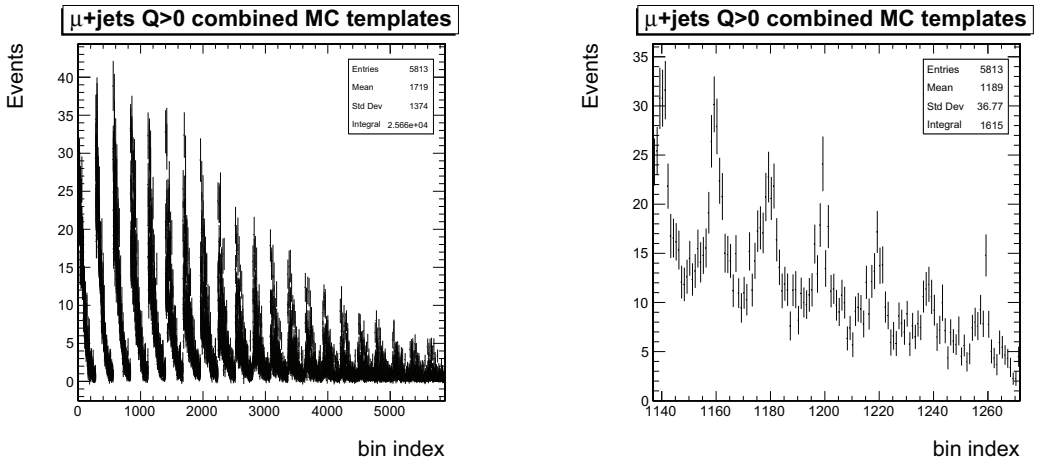

Figure 6.9: The unrolled 1D distribution of all simulated process combined together according to their cross sections and normalized to the same integrated luminosity as collected data. Showing $\mu + jets$ with $Q > 0$ only for simplicity. Left:entire distribution. Right: a zoom in of the figure in the left

6.3.3 Template building

The key ingredients in the template fit method is to produce up and down templates, which are histograms that contain information about expected number of events in every bin, corresponding to θ_j^{up} and θ_j^{down}. Together with the nominal templates, $\lambda_i(\theta)$ can be inferred by interpolating from these three sets of templates.

In order to build templates that are consistent with the fitting framework described above, we reformulate our statistical model from a probability distribution to

a distribution of expected number of events. So we change Eq. [6.9] to the following:

$$F(\boldsymbol{x}; Q|\boldsymbol{\theta}) = \sum_j F_{bkg_j}(\boldsymbol{x}; Q|\boldsymbol{\theta}) + F_{gg}(\boldsymbol{x}; Q|\boldsymbol{\theta}) + F_{q\bar{q}}(\boldsymbol{x}; Q|\boldsymbol{\theta}) \tag{6.20}$$

Here $\boldsymbol{x} = (|x_r|, M_r, c_r)$ is the triplet of top pair reconstructed kinematic variables, and Q is the charge of the lepton in the event as we fit $Q = \pm 1$ events separately. All $F(\boldsymbol{x}; Q|\boldsymbol{\theta})$ are created from fully selected and reconstructed events from MC simulation (except for data driven templates) and are normalized to the same integrated luminosity as the data.

We describe here all relevant information for the production of the up/down templates for all parameters. We start from our parameters of interest, $A_{\rm FB}$ and $R_{q\bar{q}}$. The $A_{\rm FB}$ templates are built from $q\bar{q} \to t\bar{t}$ events by first symmetrizing over the production angle c_r and then re-weight based on the value of $A_{\rm FB}$.

$$F_{q\bar{q}}(\boldsymbol{x}; Q|A_{\rm FB}) = F_{qs}(\boldsymbol{x}; Q) + A_{\rm FB} F_{qa}(\boldsymbol{x}; Q) \tag{6.21}$$

Where F_{qs} is the symmetrized $q\bar{q}$ template which is produced from the original $q\bar{q}$ MC templates, $F_{q\bar{q}}$, following the description of Section. 6.1.2

$$F_{qs}(|x_F|, M_{t\bar{t}}, c*; Q) = \frac{1}{2}\left[F_{q\bar{q}}(|x_F|, M_{t\bar{t}}, c_*; Q) + F_{q\bar{q}}(|x_F|, M_{t\bar{t}}, -c_*; -Q)\right] \tag{6.22}$$

In Fig. 6.10, we show the $F_{q\bar{q}}(c^*|A_{\rm FB})$ templates corresponding to $A_{\rm FB} = -1.0, 0, +1.0$ for both channels.

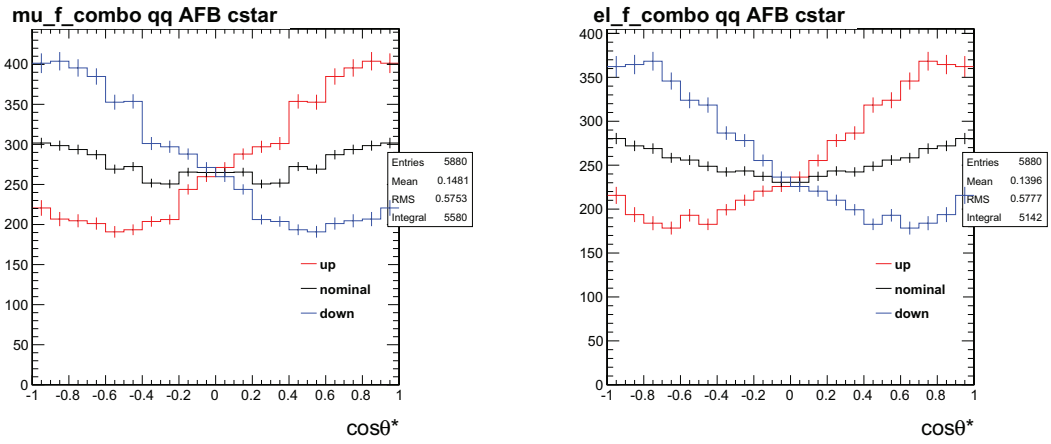

Figure 6.10: The distribution of MC simulated $q\bar{q} \to t\bar{t}$ events with A_{FB}= -1.0 (blue), 0 (black) and +1.0 (red), for $\mu + jets$(left) and $e + jets$(right)

Note here F_{gg} is the template consist of both $gg \to t\bar{t}$ and non-gg initiated $t\bar{t}$ events. The gg initiated events are symmetric in c_*, and they are incorporated using the same procedure that is applied to build $F_{q\bar{q}}$. In comparison, the non-gg initiated part of F_{gg} is not symmetrized in order to preserve the residual forward-backward asymmetry in the qg initiated $t\bar{t}$ events. This guarantees the A_{FB} fit from data only reflects the asymmetry in $q\bar{q} \to t\bar{t}$ process, as desired.

Next, we produce the up/down templates representing the relative abundance of $q\bar{q} \to t\bar{t}$ in all signal $t\bar{t}$ events, denote as $R_{q\bar{q}}$ in Eq. [6.9]. Per the design of Theta Framework, instead of using $R_{q\bar{q}}$ as parameter directly, we introduce a different parameter, $\mathrm{SF_{q\bar{q}}}$ which is a scale factor on the normalization of the $q\bar{q}$ templates. The

nominal value of $\mathrm{SF}_{\mathrm{q\bar{q}}} = 1$. We then have templates of $F_{q\bar{q}}$ and F_{gg} as follows:

$$F_{q\bar{q}}(\boldsymbol{x}; Q|\mathrm{SF}_{\mathrm{q\bar{q}}}) = \mathrm{SF}_{\mathrm{q\bar{q}}} * F_{qs}(\boldsymbol{x}; Q) \tag{6.23}$$

$$F_{gg}(\boldsymbol{x}; Q|\mathrm{SF}_{\mathrm{q\bar{q}}}) = \frac{N_{t\bar{t}} - \mathrm{SF}_{\mathrm{q\bar{q}}} N_{q\bar{q}}}{N_{t\bar{t}} - N_{q\bar{q}}} F_{gg}(\boldsymbol{x}; Q) \tag{6.24}$$

Where $N_{t\bar{t}}$ and $N_{q\bar{q}}$ are nominal number of events in signal $t\bar{t}$ process and gg process. The above equations implicitly constrain $N_{t\bar{t}}$ to be a constant for any value of $\mathrm{SF}_{\mathrm{q\bar{q}}}$, which is implied in the original formalism of our statistical model in Eq. [6.9]. Note here in Eq. [6.23] we scale symmetric $q\bar{q}$ templates rather than the one with non-zero A_{FB} as in Eq. [6.21] to get the up/down templates for $\mathrm{SF}_{\mathrm{q\bar{q}}}$. This because we want to model the change of distribution shape and normalization due to A_{FB} and $\mathrm{SF}_{\mathrm{q\bar{q}}}$ separately, although they are correlated in predicting the expected number of events for every bin.

In addition, we note that $F_{q\bar{q}}$ and F_{gg} are the only templates depend on $\mathrm{SF}_{\mathrm{q\bar{q}}}$, and it has no effect on F_{bkg}. $\mathrm{SF}_{\mathrm{q\bar{q}}}$ is directly measured from the fitting, and $R_{q\bar{q}}$ is related to $\mathrm{SF}_{\mathrm{q\bar{q}}}$ via the following equation:

$$R_{q\bar{q}} = \mathrm{SF}_{\mathrm{q\bar{q}}}\, R^0_{q\bar{q}} = \frac{N^{fit}_{q\bar{q}}}{N^{fit}_{t\bar{t}}} \tag{6.25}$$

In our analysis we use the post-fit counts, $N^{fit}_{q\bar{q}}$ and $N^{fit}_{t\bar{t}}$ to calculate the $R_{q\bar{q}}$.

Similarly, we introduce a scale factor for each background process, SF_{bkg_j} that corresponds to R_{bkg_j} defined in Eq. [6.9]. The corresponding templates are defined as follows:

$$F_{bkg_j}(\boldsymbol{x}; Q|SF_{bkg}) = SF_{bkg_j}\, F_{bkg_j}(\boldsymbol{x}; Q) \tag{6.26}$$

$$F_{gg}(\boldsymbol{x};Q|SF_{bkg_j}) = \frac{N_{t\bar{t}} - (SF_{bkg_j} - 1)\, N_{bkg_j}}{N_{t\bar{t}}}\, F_{gg}(\boldsymbol{x};Q) \tag{6.27}$$

$$F_{q\bar{q}}(\boldsymbol{x};Q|SF_{bkg_j}) = \frac{N_{t\bar{t}} - (SF_{bkg_j} - 1)\, N_{bkg_j}}{N_{t\bar{t}}}\, F_{q\bar{q}}(\boldsymbol{x};Q) \tag{6.28}$$

From now on, we will use R_{bkg_j} exclusively, instead of usng SF_{bkg_j}, for simplicity and consistency with the original formalism of our model described in Section.[6.1.2].

Finally, the up/down templates associated with the systematic uncertainties are produced by applying alternative re-weighting factors $w_{\pm}$ on MC templates, which correspond to $\pm 1\sigma$ variation from nominal templates.

In Fig. 6.11 we show $F_{gg}(\boldsymbol{x}|\mathrm{SF}_{\mathrm{other\_bkg}})$ and $F_{\mathrm{other\_bkg}}(\boldsymbol{x}|\mathrm{SF}_{\mathrm{other\_bkg}})$ templates for μ+jets channel with $\mathrm{SF}_{\mathrm{other\_bkg}} = 0.2, 1.0, 1.8$, in three projected directions of templates. It shows for the "up" templates, that is $\mathrm{SF}_{\mathrm{other\_bkg}} = 1.8$ (the normalization of "other_bkg" process being 1.8 times the nominal value), the total events of gg/qg process become fewer than its nominal value, while "other_bkg" template is scaled up by 1.8 times, as we expected.

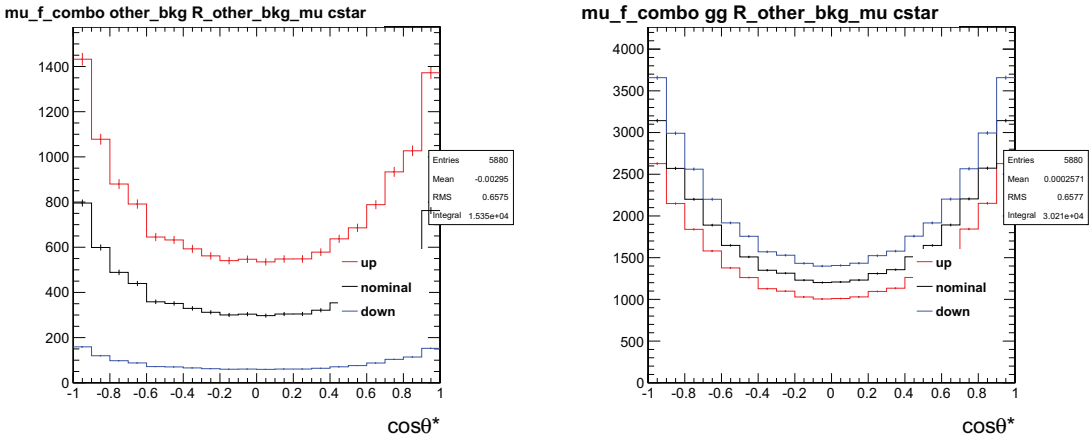

Figure 6.11: The $c*$ projection of F_{gg} (left) and $F_{\text{other\_bkg}}$ (right) templates with $\text{SF}_{\text{other\_bkg}} = 0.2$ (blue), 1.0 (black) and 1.8 (red)

6.3.4 Lepton channel combination

In this analysis, we divide the observed data into four parts (in Theta, they are called "Observable"), depending on the final state lepton flavor (e or μ) and type of lepton charge (positive or negative), and fit each of the four parts individually. However, in our model, the parameters A_{FB} and $R_{q\bar{q}}$ are independent of final states. As a result, we perform the simultaneous template fit to find the best A_{FB} and $R_{q\bar{q}}$ that describe the data.

The basic idea of combined fit is very simple. Instead of minimizing negative log likelihood as defined in Eq. [6.19] for all four observables, we minimize the sum of the

NLL, as defined below:

$$NLL_{total}(\boldsymbol{n}^{Data}) = \sum_{Q=\pm 1} NLL(\boldsymbol{n}^{Data}; e, Q|A_{\rm FB}, R_{q\bar{q}}, \boldsymbol{\theta}_e) + \sum_{Q=\pm 1} NLL(\boldsymbol{n}^{Data}; \mu, Q|A_{\rm FB}, R_{q\bar{q}}, \boldsymbol{\theta}_\mu) \tag{6.29}$$

Note that fit takes into the correlations of all four observables via template morphing. We build the up/down templates for each parameter θ_i that reflects the proper correlation. For example, change in $A_{\rm FB}$ will and only will affect the distribution of $q\bar{q} \to t\bar{t}$ process for all four both $e + jets$ and $\mu + jets$ final states. It will not affect distributions of any other processes. The correlation between $e\mu$ channels can be seen from Fig.[6.10].

Unlike the common parameter $A_{\rm FB}$ and $R_{q\bar{q}}$, we model the normalizations of background processes, such as $\rm R_{WJets}$, $\rm R_{other\_bkg}$ and $\rm R_{QCD}$, separately for $e + jets$ and $mu + jets$ channels. So we introduce two nuisance parameters for each type of background process, one for $e + jets$ channel, another for $\mu + jets$ channel. For instance, we introduce $\rm R_{WJets\_el}$ and $\rm R_{WJets\_\mu}$ and build two sets of un-correlated templates, as shown in Fig. 6.12

A final note is on the set of templates for same lepton flavor, but different charge type, such as $F_{q\bar{q}}(\boldsymbol{x}; e, Q > 0|A_{\rm FB})$ and $F_{q\bar{q}}(\boldsymbol{x}; e, Q < 0|A_{\rm FB})$. We assume they are always correlated. Therefore, most of the templates we show are charge summed for visualization purposes, while in template fit, the charge separated templates are used for calculating likelihood.

More details of all parameters are listed in Table.[6.3]

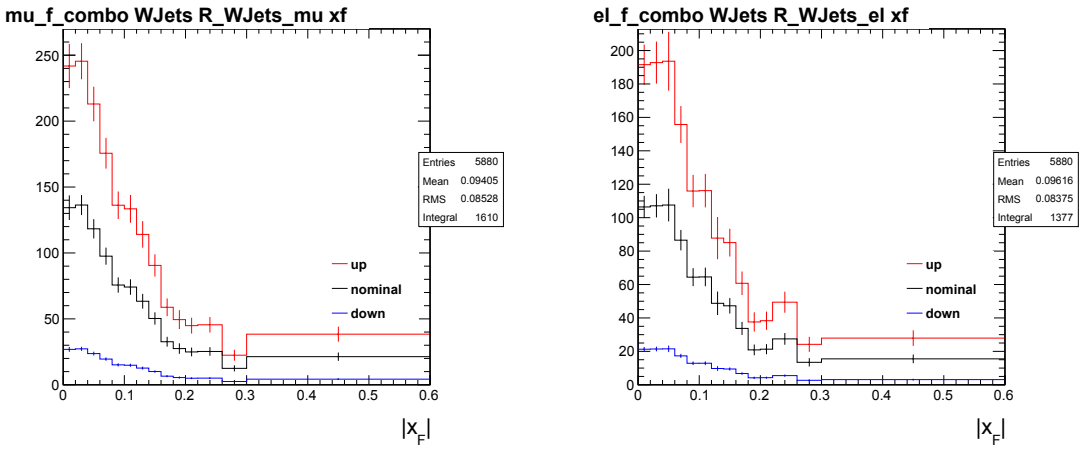

Figure 6.12: The $|x_F|$ projection of $F_{WJets}(\boldsymbol{x}; e|\mathrm{R}_{\mathrm{WJets\_el}})$ (left) and $\mathrm{F}_{\mathrm{WJets}}(\boldsymbol{x}; \mu|\mathrm{R}_{\mathrm{WJets\_}\mu})$ (right) templates with $\mathrm{R}_{\mathrm{WJets\_el}}/\mathrm{R}_{\mathrm{WJets\_}\mu} = 0.2$ (blue), 1.0 (black) and 1.8 (red)

6.3.5 Priors

As described in Section.[6.3.1] the likelihood also include the prior distribution for each parameter. In addition, since the template morphing is based on the interpolation of the up/down/nominal templates, we also need to keep track of the choice of up/down templates corresponding to each parameter. We summarize this information in Table.[6.3]

Parameter	Template Type	Prior	down	central	up	channel
A_{FB}	shape	flat	-1.0	0.0	1.0	both
$\mathrm{R}_{\mathrm{q\bar{q}}}$	shape	flat	0.2	1.0	1.8	both
$\mathrm{R}_{\mathrm{WJets\_}\mu}$	shape	flat	0.2	1.0	1.8	μ+jets
$\mathrm{R}_{\mathrm{other\_}\mu}$	shape	flat	0.2	1.0	1.8	μ+jets
$\mathrm{R}_{\mathrm{WJets\_e}}$	shape	flat	0.2	1.0	1.8	e+jets
$\mathrm{R}_{\mathrm{other\_e}}$	shape	flat	0.2	1.0	1.8	e+jets
$\mathrm{R}_{\mathrm{QCD\_e}}$	rate	log-normal	0.8	1.0	1.2	e+jets
Lumi	rate	log-normal	-0.045	0.0	0.045	both
Systematics	shape	Gauss	-1σ	0.0	1σ	depends

Table 6.3: Type and prior for all parameters. Flat prior means uniform prior distribution. Gauss prior means the prior distribution is a Normal distribution with $\mu = 0$,$\sigma = 1$. For nuisance parameters associated with shape based systematic uncertainties, we assume the up/down templates correspond to 1σ away from nominal values in the prior distributions. The up/down value for $\mathrm{R}_{\mathrm{process}}$ is relative to the nominal value. The corresponding templates are produced according to Eq. 6.23 and 6.26

6.4 Sensitivity Studies

6.4.1 Gluon Polarization Study

To tune the event weighting to use the Powheg and MagGraph samples listed in Table 5.3, generator-level $q\bar{q} \to t\bar{t}(j)$ events are fit to a distribution function derived from Eq. 6.4,

$$f_{\text{gen}}(\alpha; M, c_*) = \frac{1 + \beta^2 c_*^2 + (1-\beta^2) + \alpha\,(1-\beta^2 c_*^2)}{2\left[2 - \frac{2}{3}\beta^2 + \alpha\left(1 - \frac{1}{3}\beta^2\right)\right]}. \tag{6.30}$$

to determine best values for α. The Powheg fit yields the surprising value $\alpha = -0.129 \pm 0.010$ indicating that Powheg generates $q\bar{q} \to t\bar{t}$ events with a steeper-than-tree-level angular distribution. The presence of real longitudinal gluon polarization would manifest itself as a positive value for α. Note that the effect of positive or negative α is accounted in the definition of $A_{FB}^{(1)}$. The goodness of fit can be demonstrated by applying the weight f_{gen}^{-1} to each event and plotting the resulting $|c_*|$ distributions for $\alpha = 0$ and $\alpha = -0.129$ as shown in Fig. 6.13(a-b). The $\alpha = 0$ "unweighting" shows a monotonic increase of about 8% from smallest to large $|c_*|$ bin suggesting that the generated events are more strongly peaked at large $|c_*|$ than naive tree-level expectations. Using $\alpha = -0.130$ removes the effect and leads to a maximum bin to bin variation of 1.7%. To test this further, the procedure is repeated by dividing the sample into 0-(extra)jet and 1-jet subsamples. The effect of "negative gluon polarization" is seen more strongly in the 0-jet sample with a best fit of $\alpha = -0.256 \pm 0.011$ as shown

in Fig. 6.13(c-d). In the 1-jet sample, the presence of real longitudinal gluon polarization increases the best fit to $\alpha = 0.143 \pm 0.019$ and is shown in Fig. 6.13(e-f). The same procedure is performed on a sample of $q\bar{q} \to t\bar{t}(j, jj, jjj)$ events generated by MadGraph5. A similar pattern is observed but the results, summarized in Table 6.4, are not identical. The Powheg and MadGraph5 predictions for the forward-backward asymmetry are also listed in Table 6.4. It is clear that the virtual NLO corrections contained in Powheg but not MadGraph5 are large and important.

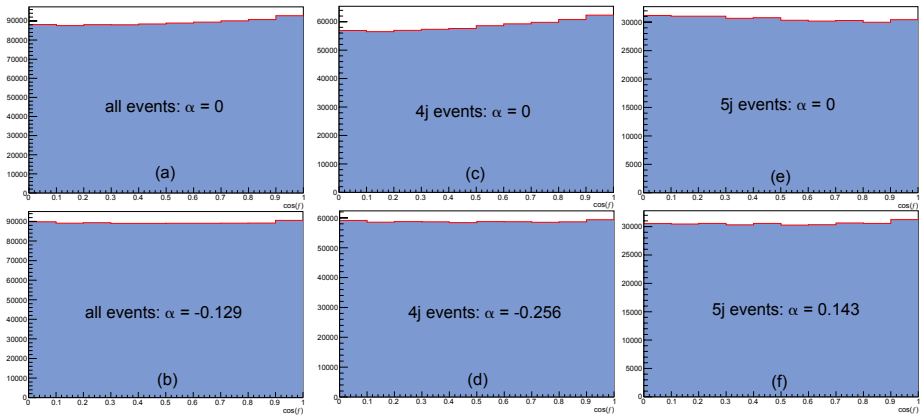

Figure 6.13: The "unweighted" $|c_*|$ distributions (events weighted by f_{gen}^{-1}) distributions of Powheg $q\bar{q} \to t\bar{t}(j)$ events for longitudinal gluon polarizations $\alpha = 0$ [(a), (c), (e)] and best fit values [(b), (d), (f)]. The distributions are shown for samples containing: all events (a-b), 0 extra jets (c-d), and 1 extra jet (e-f).

We can also fit for α as a parameter that dependent on $t\bar{t}$ invariant mass [43]. This allows for a more accurate description of the gluon longitudinal polarization based on the NLO MC simulation. We performed a binned likelihood fit of $c*$ distribution for

Sample	α	A_{FB}	A_{FB}^{gg}	$R_{q\bar{q}}$
Powheg(hvq)	$-0.129(10)$	$+0.0356(15)$	$+0.0058(11)$	0.066
MadGraph5	$-0.173(7)$	$-0.0283(27)$	$-0.0026(11)$	0.093

Table 6.4: The best fit values for the longitudinal gluon polarization α for samples of Powheg(hvq) and MadGraph5 events. The Powheg full NLO and MadGraph5 partial NLO expectations for the t-quark forward-backward asymmetry, the residual forward-backward asymmetry of the "gluon-gluon" sample from $q(\bar{q})$-g initial states, and the accepted $q\bar{q}$ event fractions are also listed. Note that the "gg" asymmetries are smaller than the $q\bar{q}$ asymmetries by an order of magnitude.

simulated $q\bar{q} \to t\bar{t}$ events before any selection is applied. We divide simulated events by the range of β, and fit these events to get β dependent α values. We then use the α acquired this way to make the asymmetric templates f_{qa} as described in Eq. 6.8.

The fit distribution and comparison to NLO MC simulated distributions are shown in Fig. 6.14. All the simulations are generated with proton-proton $\sqrt{s} = 13$ TeV in the figures.

6.4.2 Closure Test

The statistical power of the technique was investigated by simulating and fitting 2000 pseudo experiments of similar number of events in Data. We scan over a range

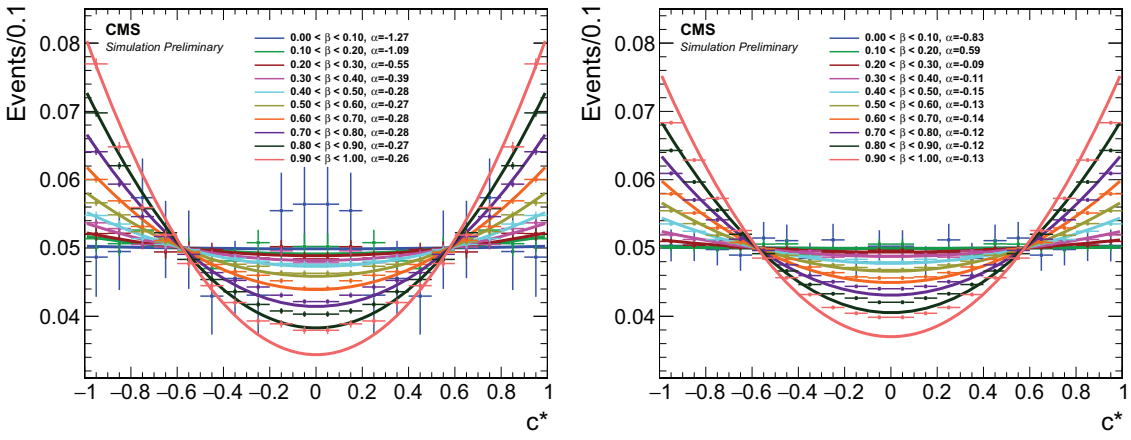

Figure 6.14: Fit comparison of $c*$ for simulated $q\bar{q} \to t\bar{t}$ events generated by aMC@NLO (left) and Powheg (right) generators.The best fit values for α are shown in the legend. Simulation distribution is shown as cross, while best fit distribution is shown as solid lines.

of values of A_{FB} and $R_{q\bar{q}}$, for every parameter value we generate 2000 pseudo experiments based on the statistical model described in Eq.6.16, then fit the pseudo experiment with the same templates that generate pseudo-data. We than estimate the mean and spread of the fit results of all experiment by fitting with a Gaussian distribution.

From the mean and standard deviation of fit value corresponding to every input value of parameters, we construct a Neyman band, which we use to extrapolate the confidence interval given the fit value of parameters from Data fit. We take the half of 68% confidence interval as the statistical uncertainty of the template fit, which is indicated as dashed red lines in Fig. 6.15, The estimated statistical uncertainties are listed below:

- $\sigma_{A_{FB}} = 0.50$

- $\sigma_{R_{q\bar{q}}} = 0.006$

An example distribution of pseudo experiments fit results for A_{FB} and $R_{q\bar{q}}$ is shown in Fig. 6.16. The Neyman construction is shown in Fig. 6.15. From these plots we find the template fit has very small bias and the confidence interval extrapolated this way is close to the statistical uncertainty we get from THETA.

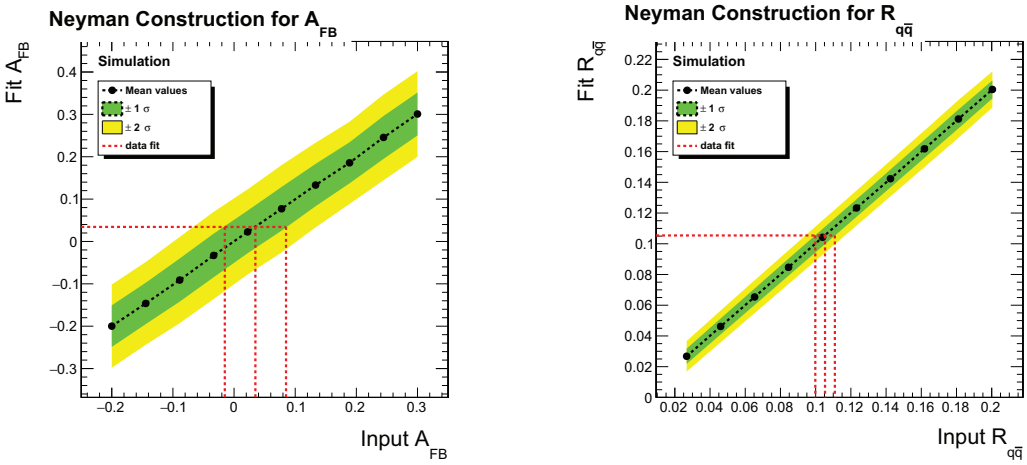

Figure 6.15: Neyman construction for A_{FB}(left) and $R_{q\bar{q}}$ (right). The dashed red line indicate the extrapolated fit result and the $\pm 1\sigma$ value given the measured value.

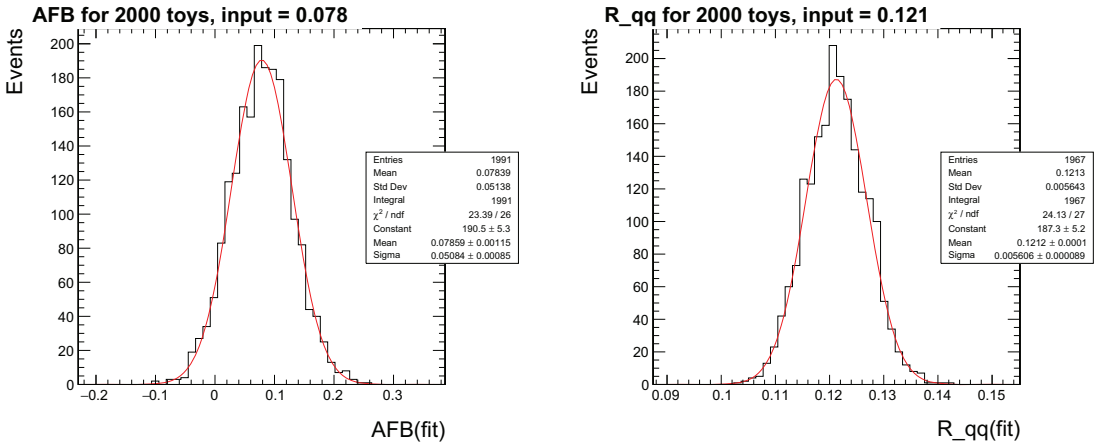

Figure 6.16: Fit parameter distribution of 2000 pseudo experiments for A_{FB}(left) and $R_{q\bar{q}}$ (right).

6.5 Corrections and Systematic Uncertainties

The detector simulation does not account for a number of known detector and experimental effects. Standard CMS correction factors are applied to the simulated events to compensate for these deficiencies. In addition, there are uncertainties associated with theoretical models underlying the event generation in both matrix element and parton showering stage. In this section we describe various corrections and associated systematic uncertainties related to our analysis.

6.5.1 Experimental Uncertainties

6.5.1.1 Jet Energy Scale

Jet energy scales are a set of scale factors that correct the 4-momentum of jets reconstructed from CMS detector response to the particle level jet momentum. The corrections are applied sequentially in different stages which handle different aspects. The L1 Pile-up correction removes energy coming from pile-up events and is applied to both data and MC. The L2/L3 MC-truth correction which corrects the p_T and η of reconstructed jets to the particle level ones, is applied to both data and MC as well. Finally, L2/L3 residual corrections handle the differences in jets between MC and data.

We then estimate the systematic uncertainty by adjusting the jet energy scale factor depending on the p_T and η of jet. The amount of change in JES is according to the dedicated measurements [34].

The templates corresponding to $\pm 1\sigma$ from nominal value of JES for $gg \to t\bar{t} \to \mu + jets$ are shown below in Fig. 6.17. It shows that JES changes both the normalization and shape of this template. It turned out that JES is one of the dominate systematic uncertainties.

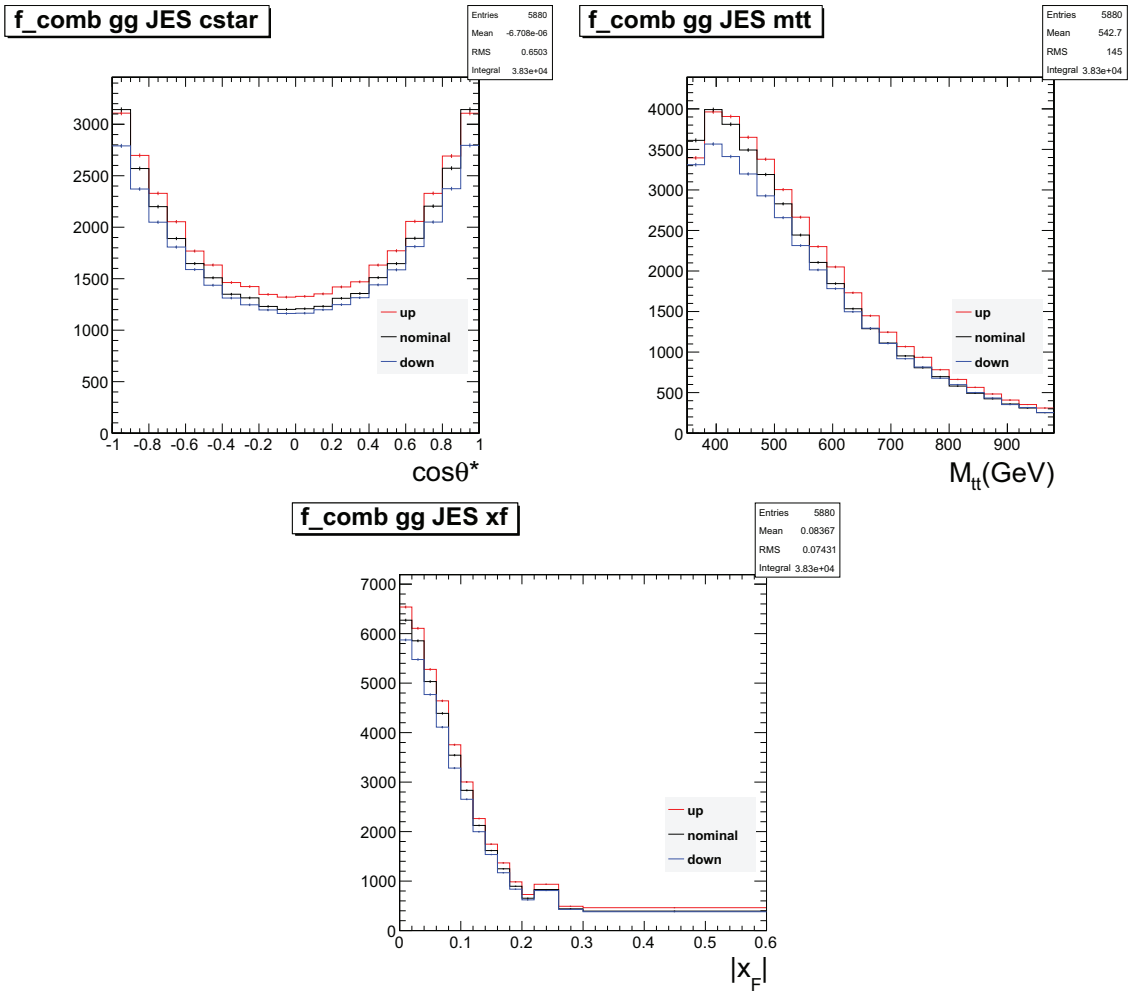

Figure 6.17: The distribution of MC simulated $gg/qg \to t\bar{t} \to \mu + \text{jets}$ events with $\text{SF}_{\text{JES}} = -1\sigma$ (blue), 0 (black) and $+1\sigma$ (red)

6.5.1.2 Jet Energy Resolution

Measurements show that the jet energy resolution (JER) in data is worse than in the simulation and the jets in MC need to be smeared to describe the data. We use scaling method to correct the transverse momentum of a reconstructed jet, p_T, by a facor w_{JER}, defined below:

$$w_{JER} = 1 + (\text{SF}_{\text{JER}} - 1)\frac{p_T - p_T^{ptcl}}{p_T} \tag{6.31}$$

where p_T^{ptcl} is the transverse momentum of jet clustered from generator-level particles, and SF_{JER} is the scale factor measured from data and MC comparison in dedicated analysis[34] and listed in Table 6.5.

We evaluated the systematics by adjusting SF_{JER} up and down as listed above to produce two more versions of templates for each MC sample. The effects of the JER and JES systematics on $t\bar{t}$ templates are also shown below.

The templates corresponding to $\pm 1\sigma$ from the nominal value of JES for $gg \to t\bar{t} \to \mu + jets$ are shown below in Fig. 6.18. It can be seen that JES changes the shape of this template, especially in c^* and $M_{t\bar{t}}$ distributions.

$\|\eta\|$ range	down	central	up
0.0-0.5	1.053	1.079	1.105
0.5-1.1	1.071	1.099	1.127
1.1-1.7	1.092	1.121	1.150
1.7-2.3	1.162	1.208	1.254
2.3-2.8	1.192	1.254	1.316

Table 6.5: Jet Energy Resolution scale factors and uncertainties for different $|\eta|$ range.

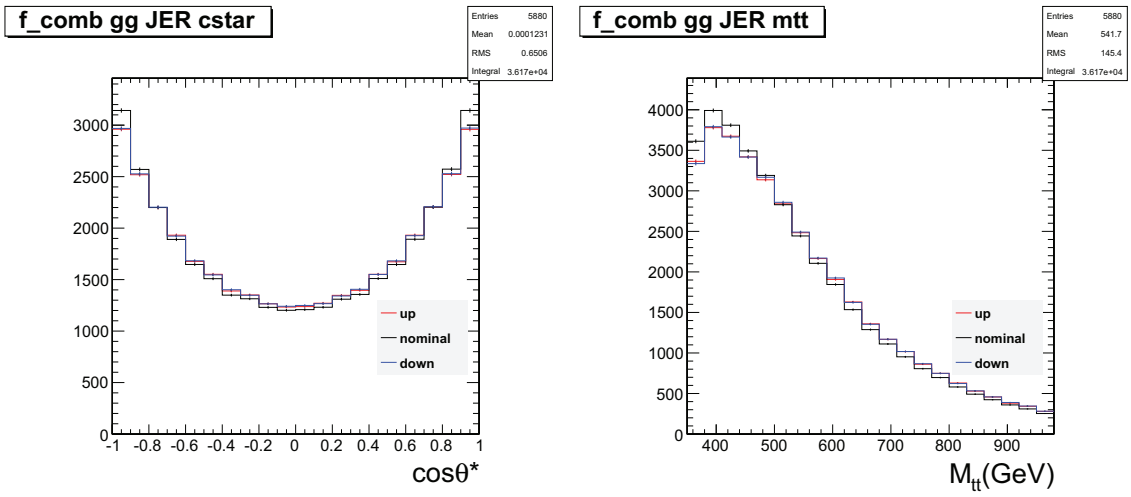

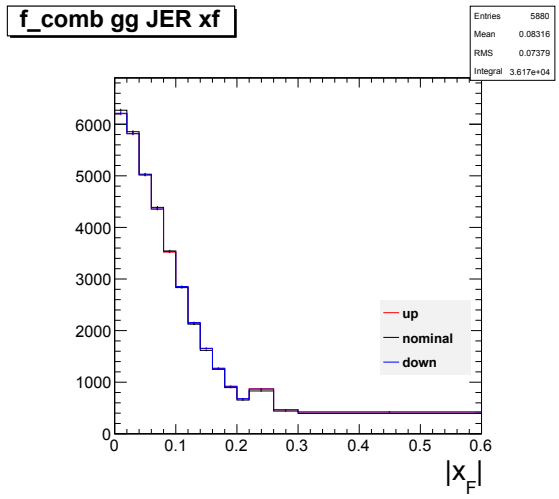

Figure 6.18: The distribution of MC simulated $gg/qg \to t\bar{t} \to \mu + \text{jets}$ events with $w_{JER}=$ -1σ (blue), 0 (black) and $+1\sigma$ (red)

6.5.1.3 Pileup Reweighting

All simulated samples are reweighted to reflect the distribution of pileup events observed in data by applying a scale factor that depends upon the number of reconstructed pileup events. The scale factor is calculated for each bin by dividing the estimated number of true interactions in the 2012 dataset by the number of true interactions in the simulated samples. Pileup estimates for data are obtained from the pileup JSON file provided by the Physics Validation Team after taking into account the appropriate HLT path. The number of true interactions in simulation is shown on the bottom left of Fig. 6.19 and the number of measured interactions in data is shown on the bottom right, illustrating the discrepancy.

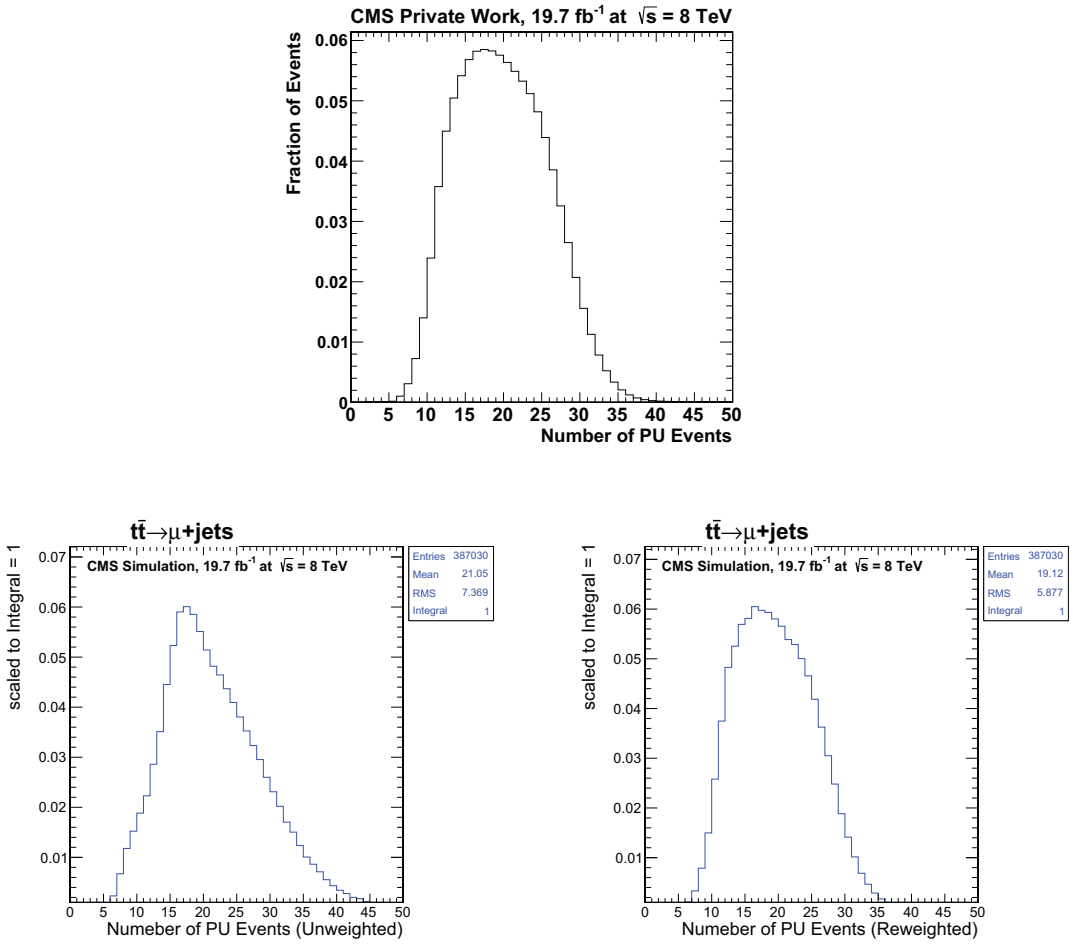

Figure 6.19: The distribution of simulated primary interactions in MC simulated $t\bar{t} \to \mu + \text{jets}$ events before (bottom left) and after (bottom right) applying PU reweighting. The reference PU distribution from 2012 collision data in the top middle shows the discrepancy intended to be corrected for.

The effect of applying the reweighting brings the two measured pileup distributions much closer into agreement as illustrated in Fig. 6.20. It shows the pileup in both simulation and data after reweighting. In this figure the signal and background

simulations have all been scaled according to their luminosities and cross sections, and the total distribution has been normalized to the data.

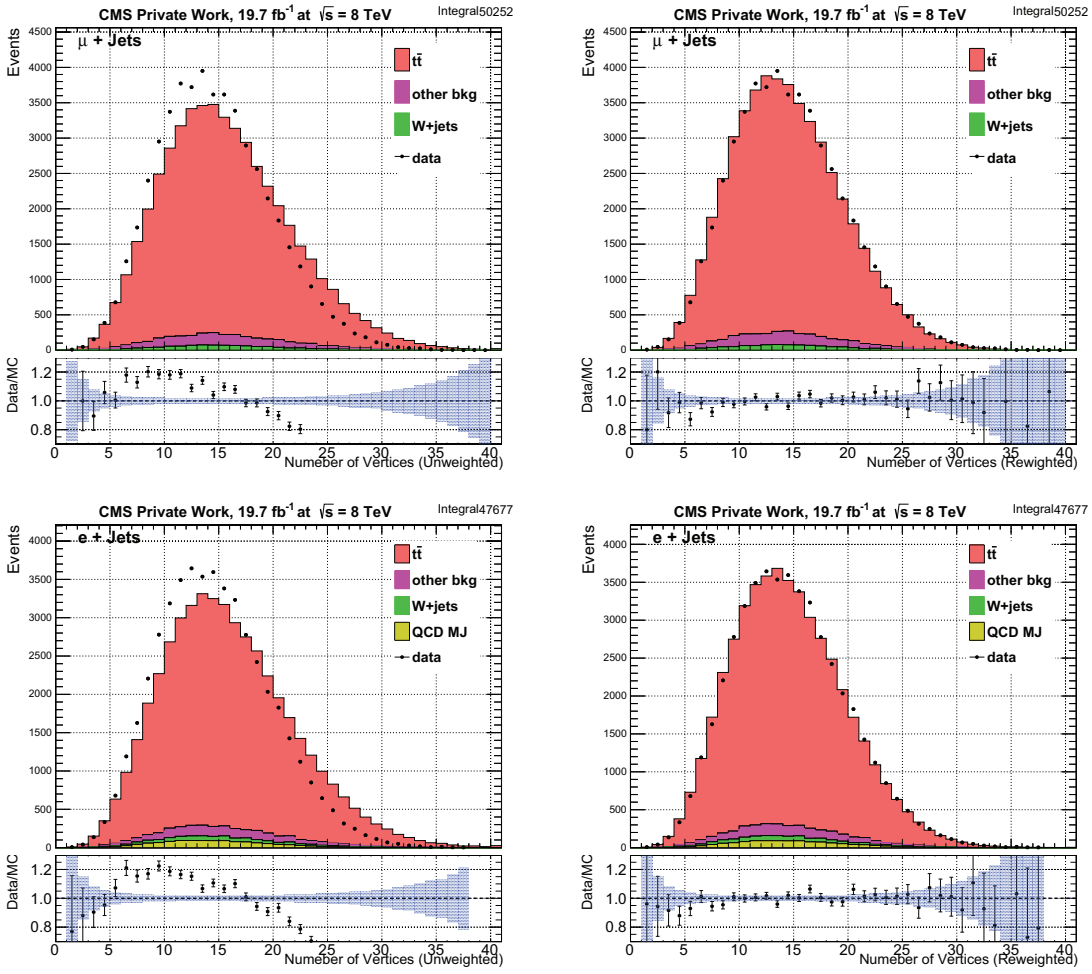

Figure 6.20: Measured pileup in simulation and data before reweighting (left) and after reweighting (right). The signal and background samples have been rescaled according to their luminosities and cross sections, and the entire distribution has been normalized to data. The simulated samples are pictured as stacked filled histograms, and the data are pictured as blue data points. The top figures are from μ+jets channel, and bottom figures are from e+jets channel.

The systematic uncertainty associated with PU re-weighting mainly originates from the uncertainty of total cross-section of min-bias events and luminosity of bunch crossing. We applied 5% uncertainty on the number of primary interactions of data to produce up and down weights for PU. Using the new weights we get the PU systematic templates for the fit.

6.5.1.4 b-tagging Efficiency

In our event selection, a jet is tagged as a b-jet if it passes a cut on its CSV discriminator value. However, the efficiency for a real b-jet to be tagged as a b quark is different in simulation and data, and so is the probability for a non-b-jet to be misidentified as a b quark. A scale factor is applied to simulated events to correct for this discrepancy.

The scale factor (SF) is defined as the ratio of b-tagging efficiency for data and MC. It is a function of jet flavor, p_T and η. The b-tagging efficiency for a jet of flavor f in the (i, j) bin of (p_T, η) is as follows:

$$\varepsilon_f(i,j) = \frac{N_f^{b-tagged}(i,j)}{N_f^{total}(i,j)} \tag{6.32}$$

Note that the b-tagging efficiency can be different for each MC sample. The weight applied for each event is then chosen as $w = \frac{P(data)}{P(MC)}$ where the probability of a given event in the MC distribution is

$$P(MC) = \prod_{i=tagged} \varepsilon_i \prod_{j=not\,tagged} (1 - \varepsilon_j) \tag{6.33}$$

and the corrected probability for the distribution in data is

$$P(data) = \prod_{i=tagged} SF_i \varepsilon_i \prod_{j=not\ tagged} (1 - SF_j \varepsilon_j) \tag{6.34}$$

Muon Trigger, ID, and Isolation Efficiencies

Muon trigger, ID, and isolation efficiences are corrected by applying three scale factors, each depend on the reconstructed number of primary vertices in the event as well as muon η and p_T.

Electron ID Efficiency

We applied scale factors to correct for the difference of electron cut-based ID efficiency between data and MC. The scale factors are measured in [41], which is from the following data and MC samples using Tag-and-Probe Method:

- Data: DoubleElectron Run2012A+B
- MC: DYJetsToLL-MadGraph (Summer12)

The SF measurement select opposite-sign di-electrons events, where the tag electron passes tight electron cut-based ID and matched to the one leg of the trigger, and another electron is used as probe. The scale factors are measured in bins of (p_T, $|\eta|$) and is applied event by event as the MC/data weight.

In systematic evaluations, we introduce a nuisance parameter with Gaussian prior distribution in the likelihood definition. The up and down templates are produced

by applying the corresponding scale factors, instead of the central scale factors, for each event.

Electron Trigger Efficiency

We apply SF to correct the `HLT_Ele27_WP80` trigger efficiency of MC to Data. The scale factors are measured by comparing MC simulation to 22Jan2013 ReReco Data, using tag and probe method[21].

Similarly to Electron ID efficiency SF discussed above, we applied trigger efficiency correction to MC and introduce a nuisance parameter in systematic evaluations.

QCD Modeling and Background Composition

Due to the high cross section and wide variety of event types resulting from multijet QCD processes, Monte Carlo simulations cannot be generated with sufficient luminosity to provide a reasonable approximation of this background shape. Therefore, a data-driven method has been implemented to estimate the shape of the QCD background.

The nature of the method is to build template distributions from each of the existing simulated samples (both signal and background) in a sideband of the lepton isolation variable. The sideband used for muons is $0.13 < \mathrm{PF_{iso}}/p_T < 0.20$ and the sideband used for electrons is defined as $0.2 < \mathrm{PF_{iso}}/p_T < 1.2$. These sideband regions are inversions of the lepton selection cuts and are designed to provide a sample

enriched with multijet QCD events.

In the muon+jets channel with Run2012A-D data, it was found that only 485 events were selected in the lepton isolation sideband. Additionally, all of these events could be accounted for by the events selected from the existing signal and background simulations, indicating that QCD multijet contribution to the background is negligible in this channel. Therefore we do not consider QCD multijets background in μ+jets channel.

On the other hand, QCD multijets process is not negligible for $e + jets$ channel. We estimate the distribution of QCD process by using the distribution of observed data events in the lepton selection sideband region. This assumes that the distribution of QCD events is similar regardless of if the fake electron is isolated or non-isolated. In addition, we estimate the event rate for QCD process in signal region by using ABCD method, described in Section. 5.1.4. We then introduce a nuisance parameter R_{QCD} with a log-normal prior, so the data-driven QCD background can be scaled. The width of the prior distribution of R_{QCD} is chosen as the percentage uncertainty estimated from ABCD method.

6.5.2 Theoretical Uncertainties

Generator Uncertainties

As described in Section. 5.1.2, although we choose to use aMC@NLO to generate $t\bar{t}$ events for signal modeling, we can use POWHEG event generator for alternative signal modeling. To see the impact of this type of signal modeling systematics, a specific version of templates is created from the POWHEG generated samples, and the fit is performed.

To understand the potential impact of switching signal modeling, the comparison of A_{FB} templates from $q\bar{q} \to t\bar{t}$ process with aMC@NLO and POWHEG generator is shown in Fig. 6.21. Only μ+jets templates are shown for illustrative purpose. Note that the A_{FB} templates built from these two generators are significantly different, especially at large c_r region, whereas they are are very similar in smaller c_r regions. This fact has non-negligible impact to the fitted A_{FB}.

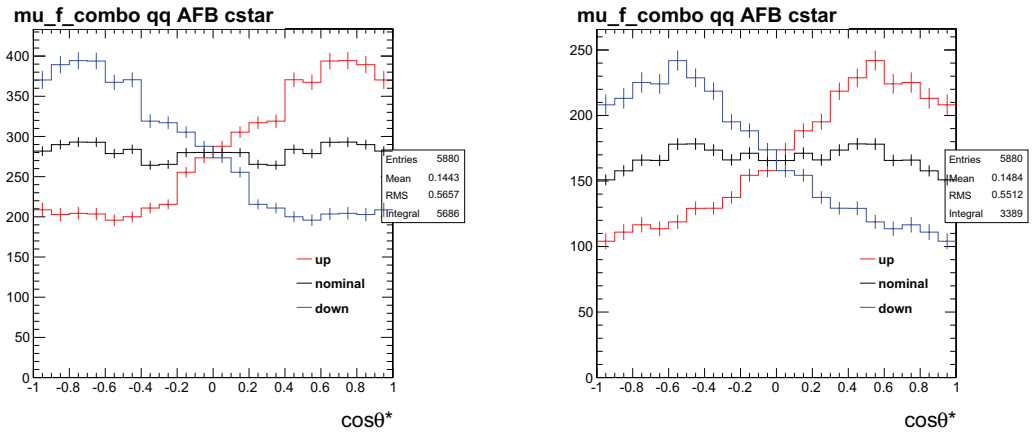

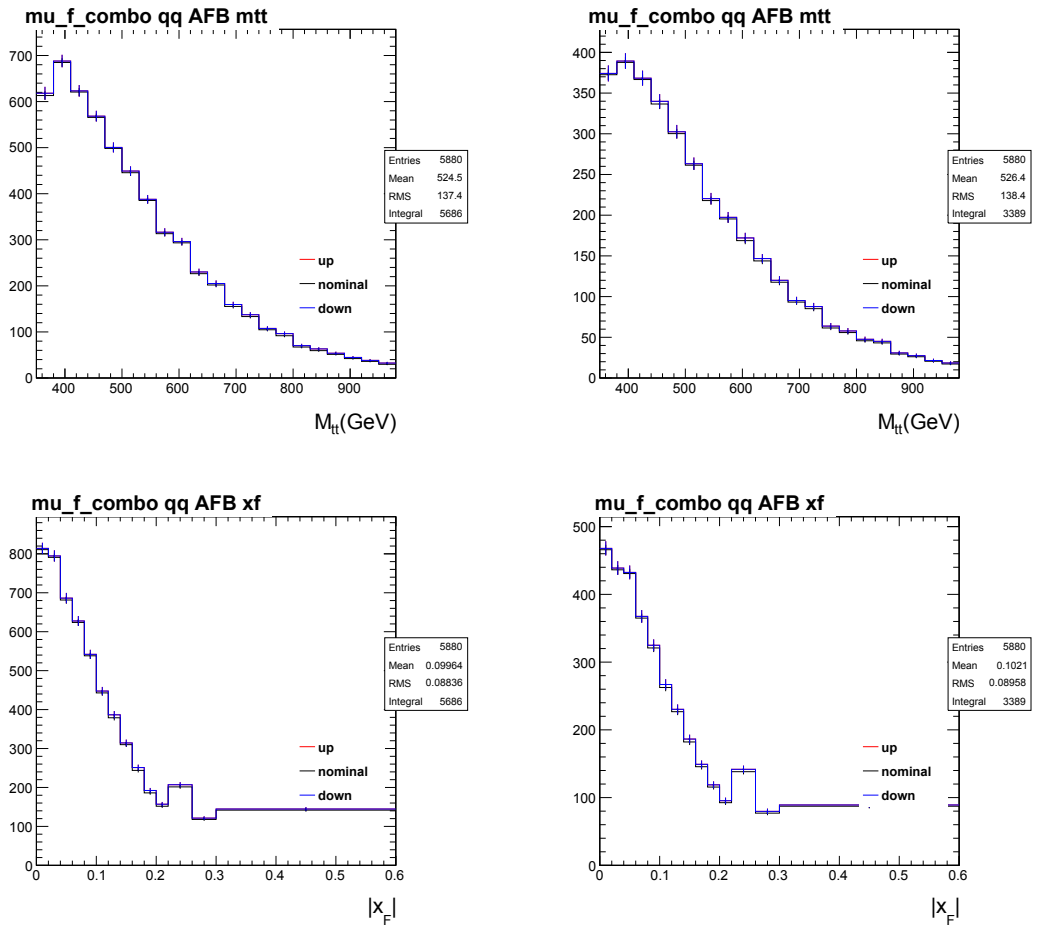

Figure 6.21: The comparison of A_{FB},$M_{\mathrm{t\bar{t}}}$,x_{F} templates from aMC@NLO (left) and POWHEG (right), for $q\bar{q} \to t\bar{t}$ events in μ+jets channel.

Top p_T Reweighting

The normalized differential top-quark-pair cross section analysis in the CMS Top Group found a persistent inconsistency between the shapes of the individual top-quark p_T distributions in simulation and data, while the NNLO approximated calculation [35] provides a reasonable description. Therefore, an individual top-quark p_T de-

pendent event scale factor has been derived to correct this shape. The scale factors recommended to use with 8 TeV data for lepton plus jets events are

$$\text{weight} = \sqrt{e^{0.318-0.00141(p_{T_t}+p_{T_{\bar{t}}})}} \tag{6.35}$$

Here, p_{T_t} and $p_{T_{\bar{t}}}$ are the generator-level transverse momenta of the individual top quark and anti-quark respectively. Note that, the application of this event scale factor does not conserve the $t\bar{t}$ cross section and this change in total cross section must be removed when renormalizing the $t\bar{t}$ samples by luminosity and cross section to derive expectations of R_{bk} and $R_{q\bar{q}}$. The value of this event scale factor for semileptonic events is pictured in Fig. 6.22 as a function of c_{r}, x_{r}, and M_{r}. It shows that top p_T reweighting is correlated with c_r and $M_{t\bar{t}}$ for $t\bar{t}$ events. As a result, applying the reweighting changes the distribution of $t\bar{t}$ events.

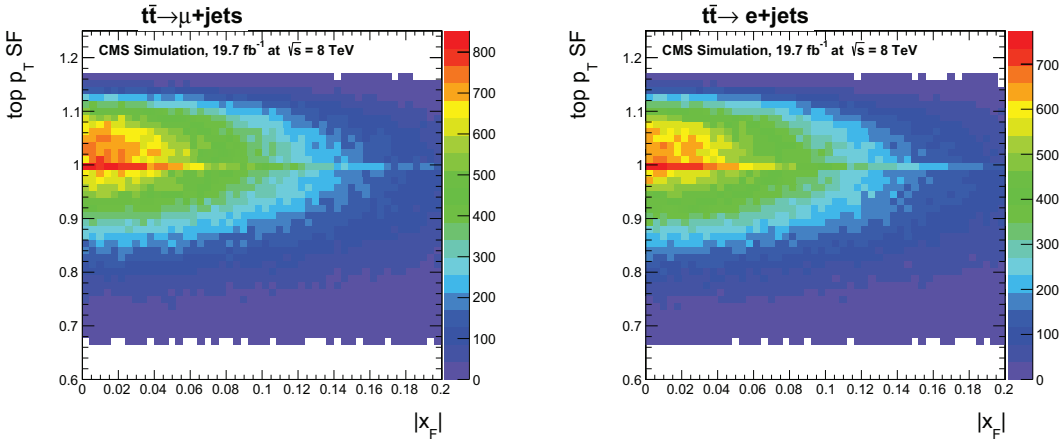

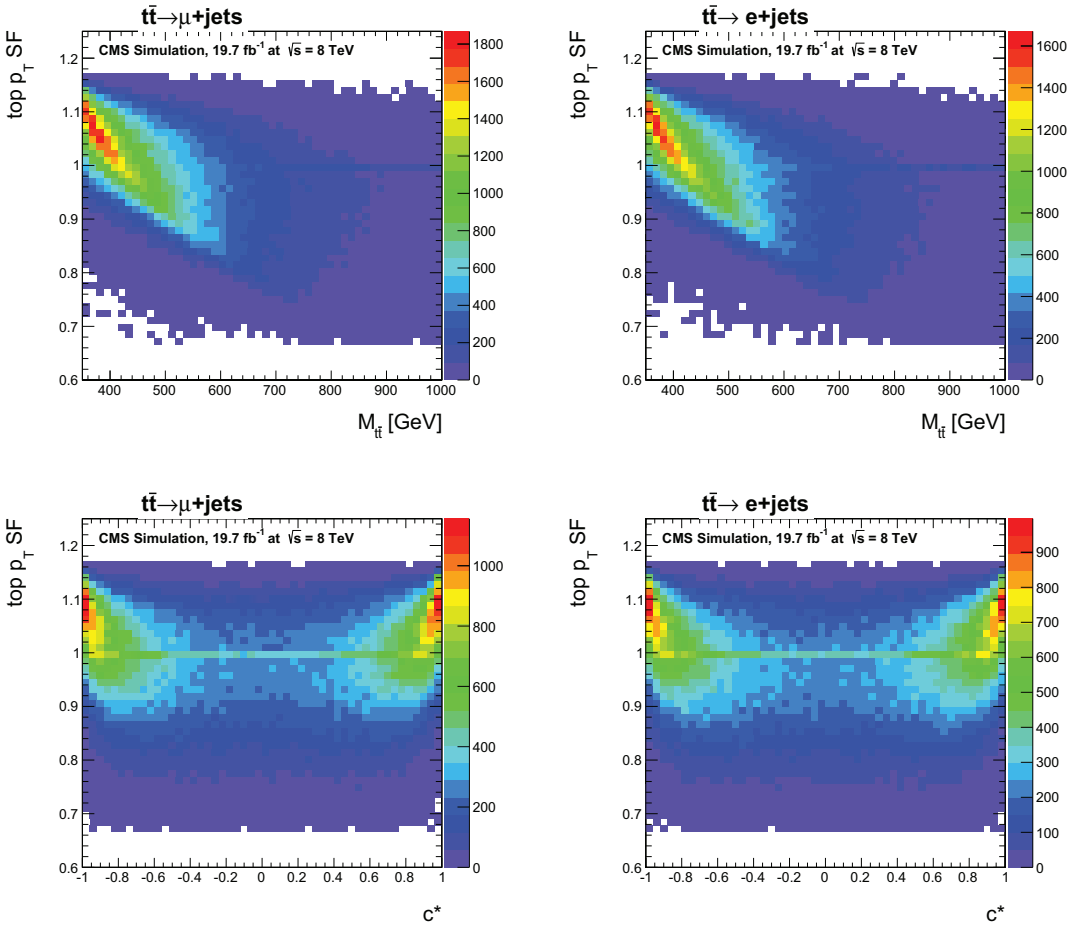

Figure 6.22: The top p_{T} reweighting event scale factor as a function of c_{r} (top), x_{r} (middle), and M_{r} (bottom) for a sample of aMC@NLO simulated semileptonic $\mathrm{t\bar{t}}$ events. The left figures are from μ+jets channel, the right figures are from e+jets channel.

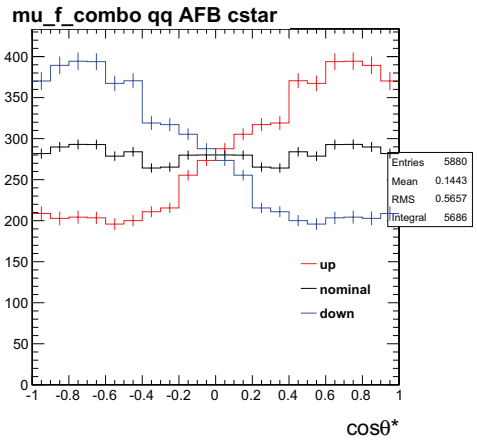
mu_f_combo qq AFB cstar
Entries 5880
Mean 0.1443
RMS 0.5657
Integral 5686
up
nominal
down
cosθ*

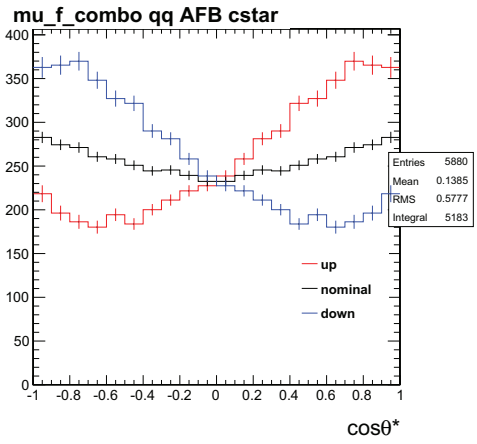
mu_f_combo qq AFB cstar
Entries 5880
Mean 0.1385
RMS 0.5777
Integral 5183
up
nominal
down
cosθ*

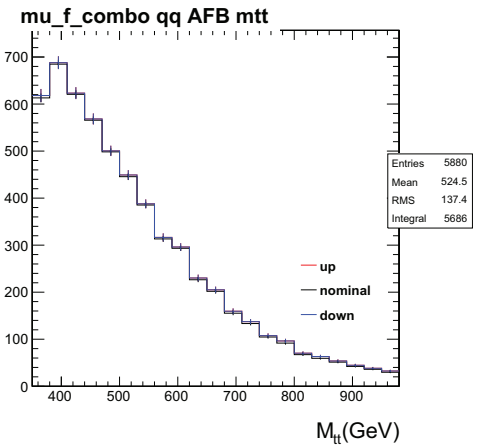
mu_f_combo qq AFB mtt
Entries 5880
Mean 524.5
RMS 137.4
Integral 5686
up
nominal
down
M_tt(GeV)

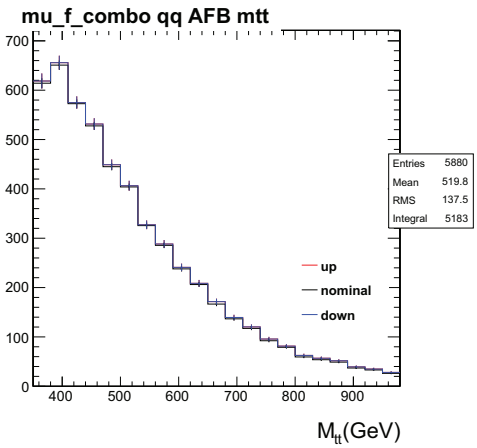
mu_f_combo qq AFB mtt
Entries 5880
Mean 519.8
RMS 137.5
Integral 5183
up
nominal
down
M_tt(GeV)

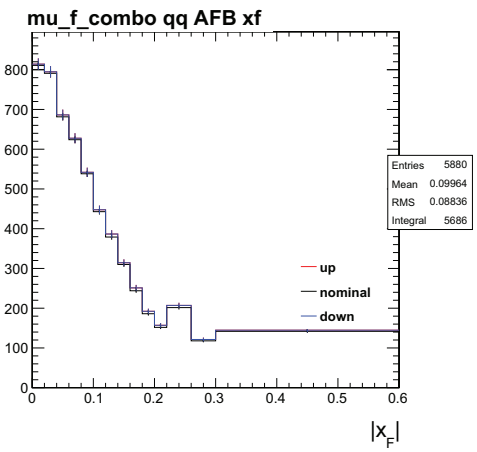
mu_f_combo qq AFB xf
Entries 5880
Mean 0.09964
RMS 0.08836
Integral 5686
up
nominal
down
|x_F|

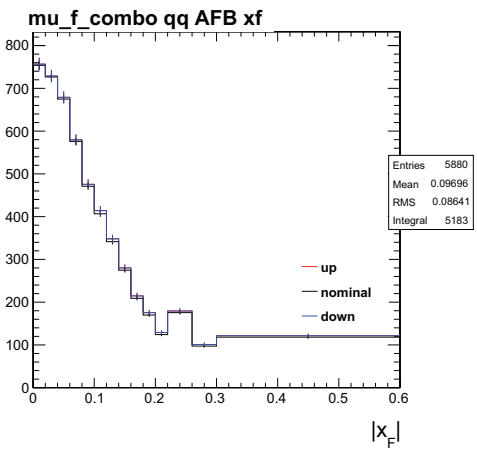
mu_f_combo qq AFB xf
Entries 5880
Mean 0.09696
RMS 0.08641
Integral 5183
up
nominal
down
|x_F|

Figure 6.23: The comparison of $A_{\rm FB}$, $M_{\rm t\bar{t}}$, $x_{\rm F}$ templates without(left) and with(right) top pT reweighting applied, for $q\bar{q} \to t\bar{t}$ events in μ+jets channel.

In subsequent template fit we don't apply top p_T re-weighting as a default, for our nominal fit. We estimate the systematic uncertainty associated with top p_T re-weighting by measuring the difference of central fit value of A_{FB} and $R_{q\bar{q}}$ with or without applying the top p_T weights. We found that top p_T re-weighting is a dominant systematic in this measurement.

Parton Distribution Functions

We estimate the systematic uncertainty from PDF of protons by producing up/down templates based on all alternative PDF sets for each MC sample. For example, for every event in our signal $t\bar{t}$ sample we take the PDF weights that are maximally below (w_-) and above (w_+) the value of nominal weight (w_0) to produce $w_{down} = \frac{w_-}{w_0}$ and $w_{up} = \frac{w_+}{w_0}$. Then we re-weight the nominal templates using these two set of weights to produce systematic templates for PDF uncertainty.

6.5.3 Evaluation method and uncertainty table

Once we have systematic templates corresponding to each of the uncertainty sources, we propagate the uncertainties to the measured parameters by taking the following approach.

As mentioned in Section 6.3 for every systematic uncertainty sources we introduce a nuisance parameter with Gaussian prior. The expected distribution can be interpolated from up, down and nominal templates provided. We first perform the template fit by fixing all systematics nuisance parameters to their nominal values. Then we allow each systematic nuisance parameter to float at a time, and take the difference between the new measured parameter value and nominal value as the systematic uncertainty from the respective source. Finally we add all systematic uncertainties in quadrature as the total systematic uncertainties.

The complete table of systematic uncertainties for both parameter of interest and other important nuisance parameters are listed below, in Table 6.6,6.7. From Table 6.7 we find out that the dominant sources of systematic uncertainties in A_{FB} measurements are jet energy correction, PDF and top pT re-weighting.

Systematics	A_{FB}	$R_{q\bar{q}}$	$R_{other\_bkg\_\mu}$	$R_{other\_bkg\_e}$	R_{WJets_μ}	R_{WJets_e}
Nominal	0.0343	0.1082	0.0728	0.0835	0.0061	0.0098
Nominal	0.0343	0.1082	0.0728	0.0835	0.0061	0.0098
B-Tagging Eff.	0.0349	0.1080	0.0726	0.0835	0.0062	0.0097
Lepton ID Eff.	0.0348	0.1087	0.0739	0.0837	0.0062	0.0098
Lepton Iso Eff.	0.0343	0.1082	0.0728	0.0836	0.0061	0.0098
Tracking Eff.	0.0345	0.1081	0.0730	0.0838	0.0062	0.0098
Trigger Eff.	0.0340	0.1084	0.0731	0.0834	0.0062	0.0098
JES	0.0151	0.1040	0.0894	0.1035	0.0100	0.0129
JER	0.0503	0.1069	0.0762	0.0867	0.0064	0.0101
PDF	0.0232	0.1094	0.0808	0.0877	0.0068	0.0098
top p_T	0.0447	0.1196	0.0887	0.1008	0.0072	0.0106
generator	0.0370	0.0742	0.0916	0.1125	0.0078	0.0110

Table 6.6: Central value of all fit parameters with one systematic nuisance parameter turned on at a time.

Systematics	$\sigma^{\text{sys}}_{A_{FB}}$	$\sigma^{\text{sys}}_{R_{q\bar{q}}}$	$\sigma^{\text{sys}}_{R_{other\_bkg\_\mu}}$	$\sigma^{\text{sys}}_{R_{other\_bkg\_e}}$	$\sigma^{\text{sys}}_{R_{WJets\_\mu}}$	$\sigma^{\text{sys}}_{R_{WJets\_e}}$
B-Tagging Eff.	2	<1	<1	<1	1	<1
Lepton ID Eff.	2	<1	2	<1	2	<1
Lepton Iso Eff.	<1	<1	<1	<1	<1	<1
Tracking Eff.	1	<1	<1	<1	1	1
Trigger Eff.	1	<1	<1	<1	1	<1
JES	56	4	23	24	63	32
JER	47	1	5	4	5	4
PDF	32	1	11	5	10	1
top p_T	30	11	22	21	17	9
generator	8	31	26	35	28	13
Total	86	33	43	47	72	36

Table 6.7: Systematic uncertainties of fit parameters from different sources, in percentage. The total systematics is calculated by adding the individual systematics in quadrature.

6.6 Results

The result of measuring A_{FB} and $R_{q\bar{q}}$ from 19.6 fb^{-1} of 8 TeV proton-proton collision data collected by CMS experiment in 2012 is given below. It is based on the binned likelihood fit of MC simulated templates (and Data driven QCD multijets template for e+jets) to 45321 mu+jets and 42923 e+jets data events.

- $A_{FB} = 0.035 \pm 0.050\,(\text{statistical}) \pm 0.029\,(\text{systemtics})$
- $R_{q\bar{q}} = 0.108 \pm 0.006\,(\text{statistical}) \pm 0.036\,(\text{systemtics})$

The expected distribution of observed data events for the best fit is compared with actual observed data in the figures below. Fig. 6.24 shows the combined event distribution, by summing over $e + jets$ and $\mu + jets$ channels and over lepton charge types. The Fig. 6.26 - Fig. 6.28 shows the individual post fit comparisons for all four observable, which are fit simuteneusly as described in Section. 6.3.4. The fit agrees with data reasonably well.

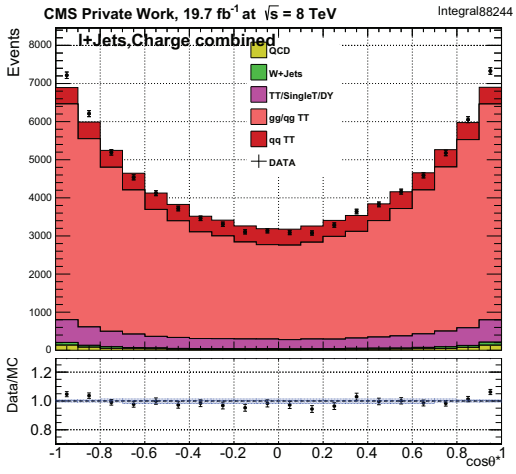

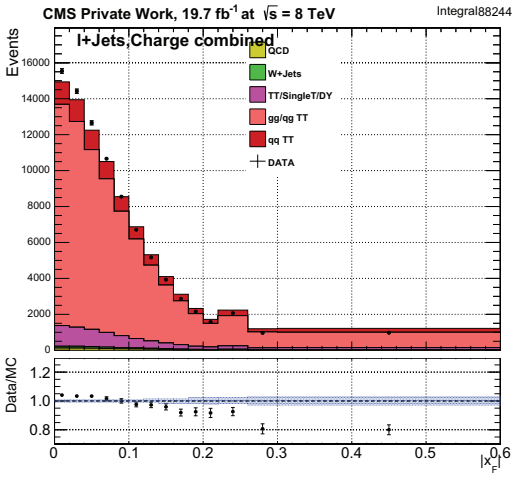

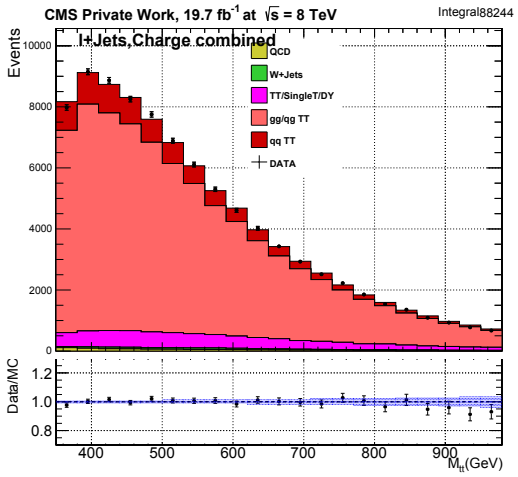

Figure 6.24: Post-fit plots of lepton and charge combined template after the fit (colored) and data (solid dots with error bar). All errors, including the shaded band in the Data/MC comparison plots, indicate Poisson error only.

In order to compare to the Standard Model prediction for A_{FB} and $R_{\mathrm{q\bar{q}}}$ we rely on the result from NLO event generators. SM prediction of A_{FB} is calculated based on the `POWHEG` generated $q\bar{q} \to t\bar{t}$ events at parton level, before applying selection, detector simulation and reconstruction. A factor of 1.15 is applied to include the QCD/EW interference effect that is not considered in `POWHEG` [14]. The SM prediction of $R_{\mathrm{q\bar{q}}}$ is calculated from the `aMC@NLO` generated semi-leptonic $\mathrm{t\bar{t}}$ events after all the selection, simulation and reconstruction.

We also compared our measurement of A_{FB} with the result of both D0 and CDF experiments of Tevatron. They measured A_{FB} in combined e/μ+jets channel, based on full Tevatron Data of proton anti-proton collision at 1.96 TeV. Although we are measuring A_{FB} at a different energy from Tevatron, the comparison is still useful as

the observable we measured is similarly defined in Tevatron.

The summary of the result in this thesis, the respective SM prediction, and the result in Tevatron is listed in Table 6.8. The comparison with Tevatron measured A_{FB} is also shown in the summary Figure, in Fig. 6.25.

	This Thesis	SM	Tevatron[6]	SM [25]
A_{FB}	$0.035 \pm 0.050 \pm 0.029$	0.041 ± 0.015	$0.128 \pm 0.021 \pm 0.014$	0.095 ± 0.007
$\mathrm{R}_{\mathrm{q\bar{q}}}$	$0.108 \pm 0.006 \pm 0.036$	0.132 ± 0.015	NA	NA

Table 6.8: Result of the measurements of this thesis, the Tevatron measurements, and the respective theoretical expectation given by Standard Model calculation. The $\mathrm{R}_{\mathrm{q\bar{q}}}$ has not been measured in Tevatron, so no result is listed in the table. For all experimental results, the first uncertainty is statistical and the second is systematic.

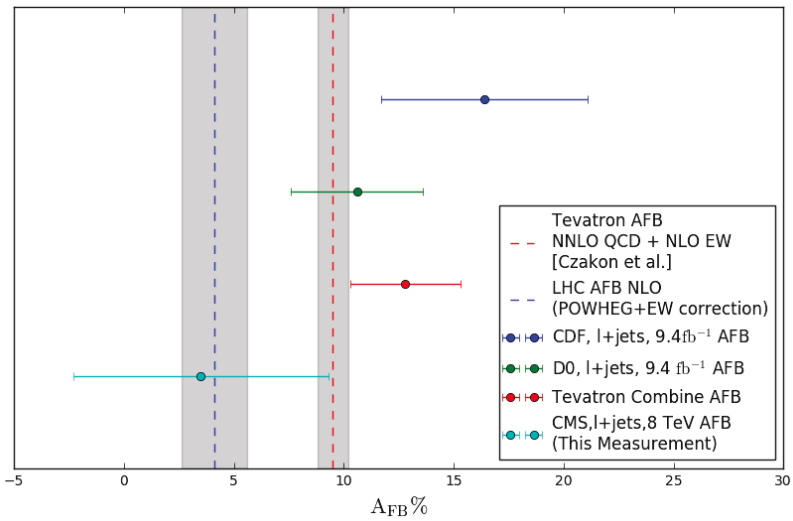

Figure 6.25: A summary of A_{FB} measurement. Tevatron results are taken from [6]

The measured A_{FB} and $\mathrm{R}_{\mathrm{q\bar{q}}}$ in this thesis are consistent with the expected value from SM. Compare with the A_{FB} measurement in Tevatron, we get competitive precision of A_{FB} measurements, despite significant dilution from gg initiated $\mathrm{t\bar{t}}$ events due to the nature of proton-proton collision in LHC.

In conclusion, we measured the Forward-Backward Asymmetry of $q\bar{q} \to t\bar{t}$ process using the l+4/5jets events from 8 TeV proton-proton collision in LHC, collected by CMS during 2012. We are able to measure A_{FB} with good accuracy, and found the result to be consistent from NNLO QCD calculation. In addition, we managed to measure the fraction of $\mathrm{q\bar{q}}$ initiated $\mathrm{t\bar{t}}$ events, which is a first attempt in CMS.

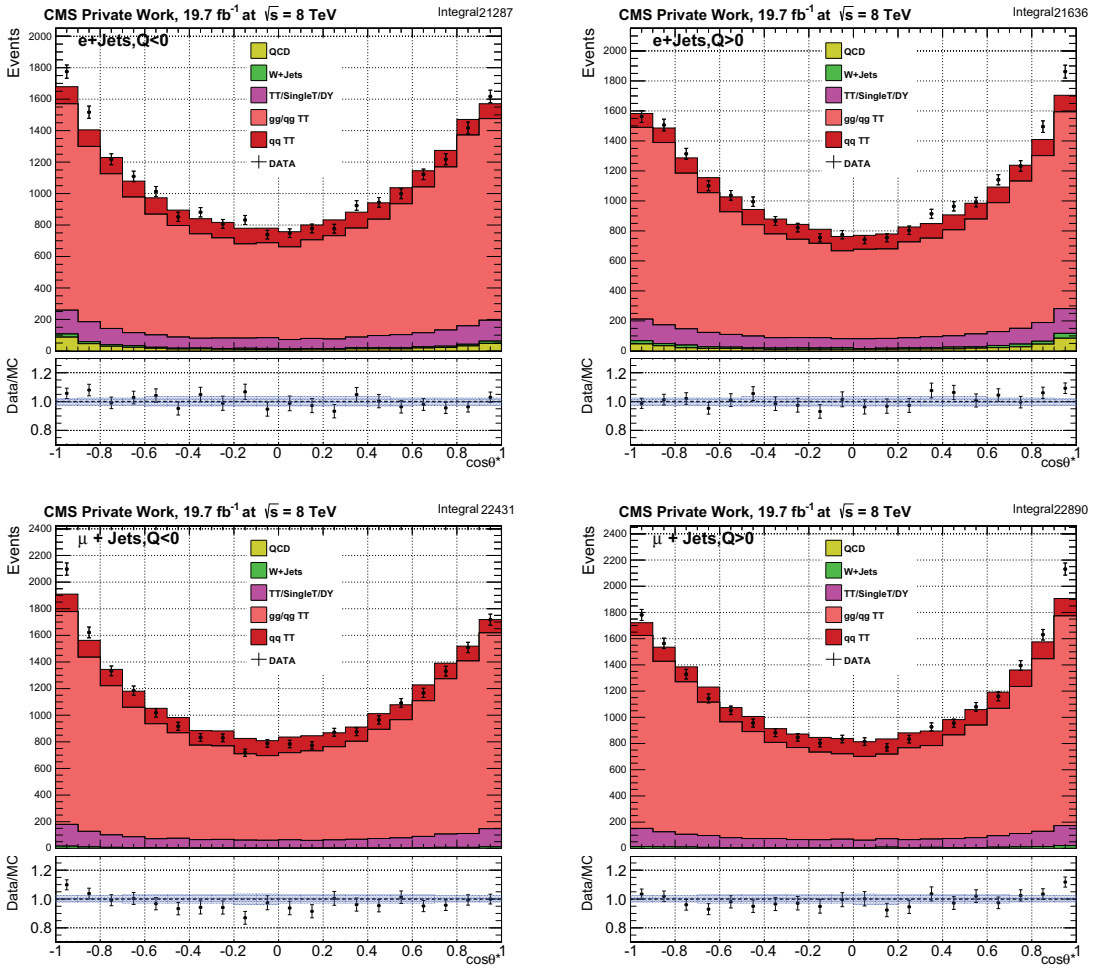

Figure 6.26: $c*$ projection of post-fit distribution of all four observable, as labeled in the figures. All errors, including the shaded band in the Data/MC comparison plots, indicate Poisson error only.

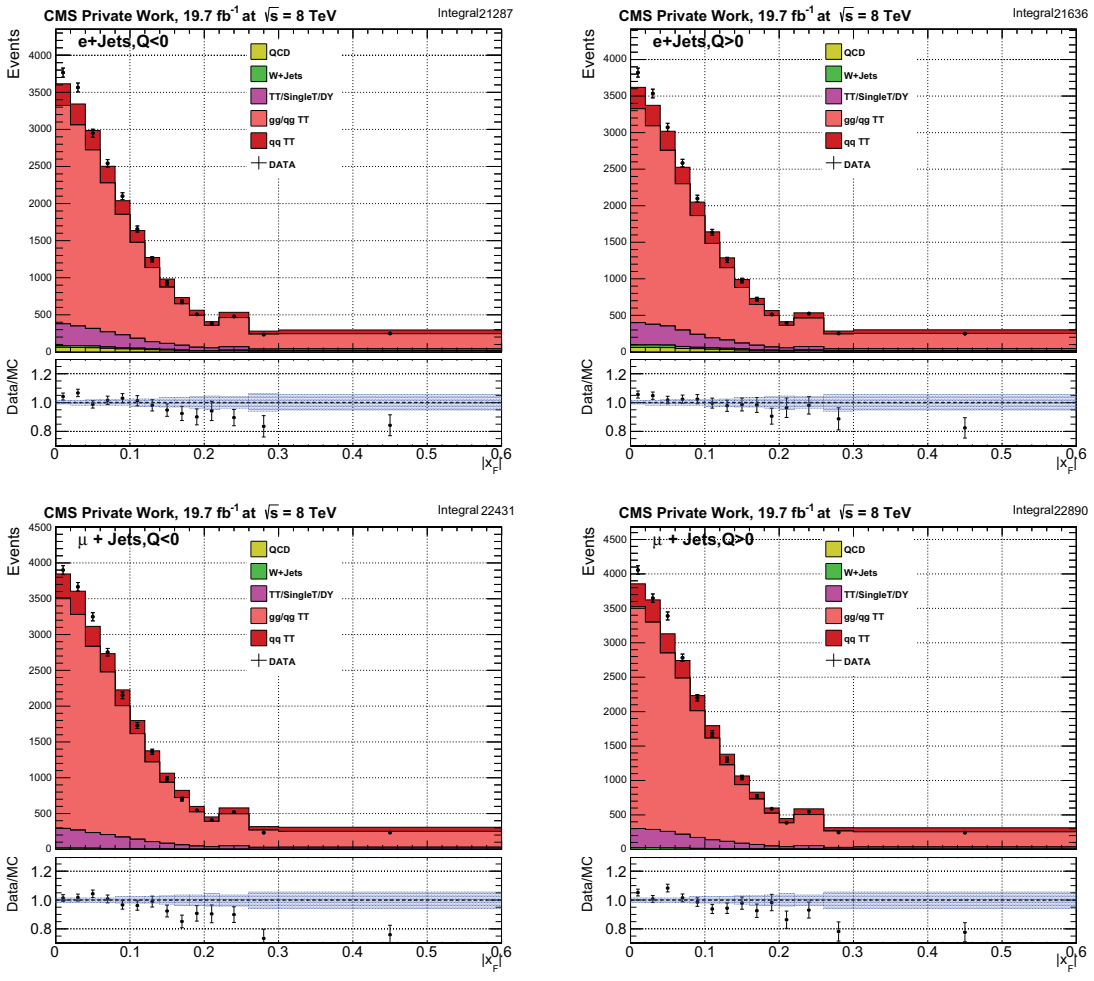

Figure 6.27: $|x_F|$ projection of post-fit distribution of all four observables, as labeled in the figures. All errors, including the shaded band in the Data/MC comparison plots, indicate Poisson error only.

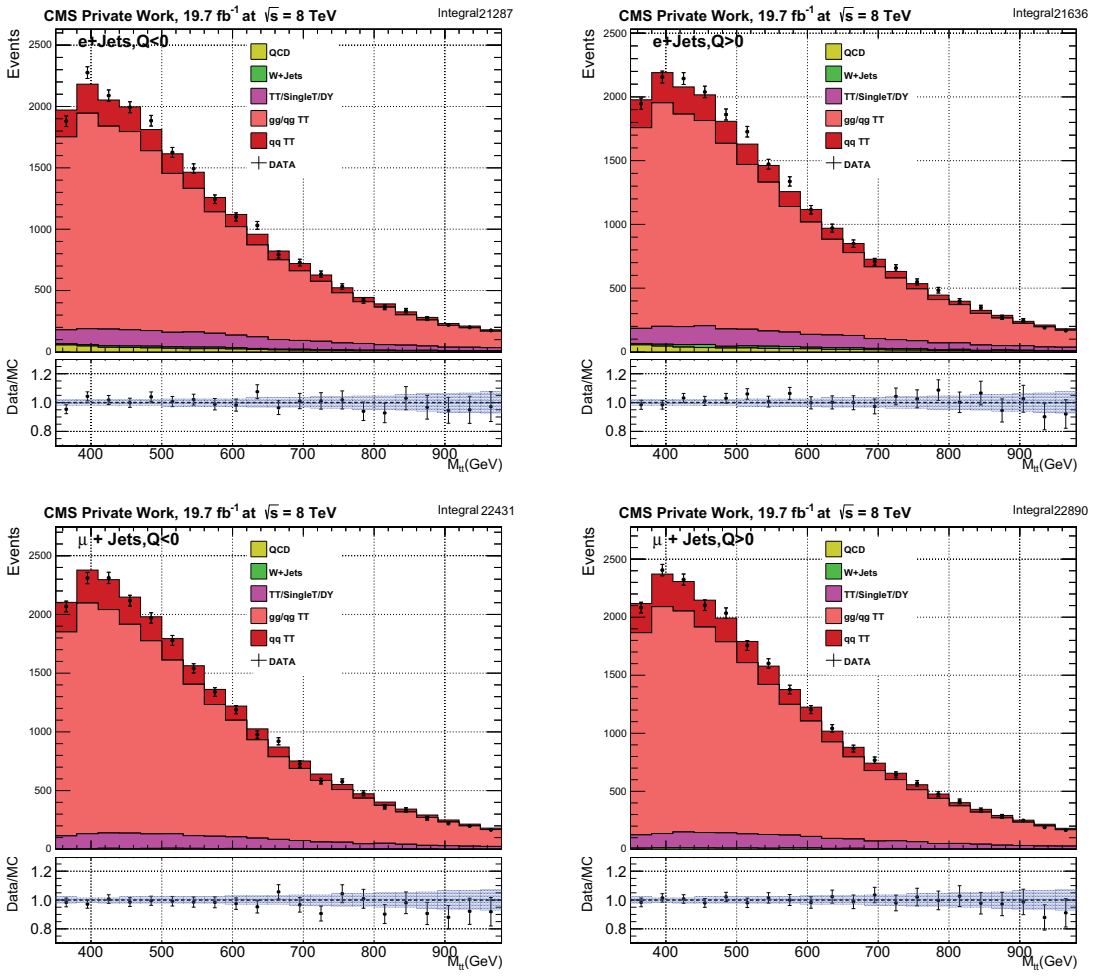

Figure 6.28: $M_{t\bar{t}}$ projection of post-fit distribution of all four observable, as labeled in the figures. All errors, including the shaded band in the Data/MC comparison plots, indicate Poisson error only.

Conclusion and Outlook

In this thesis the Foward-backward asymmetry in $t\bar{t}$ production at Large Hadron Collider is measured using 19.7 fb^{-1} of proton proton collision at 8 TeV. Only semileptonic channel of $t\bar{t}$ events are analyzed using the final states containing an electron or muon, four or five jets, where two jets are originated from bottom quarks.

A new template based measurement method is introduced in this thesis. Using this method, the parton level A_{FB} originated from $q\bar{q} \to t\bar{t}$ process is measured. In addition, the relative abundance of $q\bar{q} \to t\bar{t}$ process among all $t\bar{t}$ production processes, denoted as $R_{q\bar{q}}$ is measured simultaneously.

The measurement is performed via a maximum likelihood fit that simultaneously fit e+jets and μ+jets events. Both channels share common parameters of interest, A_{FB} and $R_{q\bar{q}}$, and have separate background process normalization estimation.

Both A_{FB} and $R_{q\bar{q}}$ are found to be consistent with theoretical prediction given by standard model, within the uncertainty of the measurement. The dominant uncertainty in A_{FB} measurement originates from the limited number of data events observed. The dominant uncertainty in $R_{q\bar{q}}$ is of the systematical origin.

One highlight of the measurement provided in this thesis is the direct measurement of A_{FB} from $q\bar{q} \to t\bar{t}$ process, allowing a closer comparison with the measurement of A_{FB} in proton anti-proton collision in Tevatron.

At the time of writing this thesis, the LHC Run2 has been extremely successful since its start in 2015. With a higher collision energy at 13 TeV indicating a larger cross section for $\mathrm{t\bar{t}}$ production (832 pb at 13 TeV vs 245 pb at 8 TeV), and a much larger integrated luminosity recorded by CMS so far (95 fb^{-1} compare with 19.7 fb^{-1}), about 14 times more $\mathrm{t\bar{t}}$ events are expected using the LHC Run2 data collected so far. As the measurement presented in this thesis is limited by the size of data, a similar measurement is expect to have a 3 times smaller statistical uncertainty, which will greatly benefit the precise test of SM in the matter of A_{FB}.

A challenge of measuring A_{FB} in LHC Run2 is the increase in the fraction of $\mathrm{t\bar{t}}$ events originated from the symmetric gluon-gluon fusion process (increases from 85% to 90%), which further dilute the expected charge asymmetry. Our approach, on the other hand, is less affected, as it managed to measure the A_{FB} from $q\bar{q} \to t\bar{t}$ process directly.

In conclusion, the template based A_{FB} measurement method proposed in this thesis is the first of its kind in CMS, and successfully measured the $\mathrm{t\bar{t}}$ A_{FB} using 8 TeV LHC data with competitive accuracy compared with previous measurements in CMS and Tevatron. It is a promising method that has the potential to surpass the precision of more traditional charge asymmetry measurements given LHC Run2 data.

Bibliography

[1] Particle-Flow Event Reconstruction in CMS and Performance for Jets, Taus, and MET. Technical Report CMS-PAS-PFT-09-001, CERN, Geneva, Apr 2009.

[2] Georges Aad et al. Measurement of the charge asymmetry in top-quark pair production in the lepton-plus-jets final state in pp collision data at $\sqrt{s} = 8\,\mathrm{T}eV$ with the ATLAS detector. *Eur. Phys. J.*, C76(2):87, 2016.

[3] Georges Aad et al. Measurements of the charge asymmetry in top-quark pair production in the dilepton final state at $\sqrt{s} = 8$?TeV with the ATLAS detector. *Phys. Rev.*, D94(3):032006, 2016.

[4] T. Aaltonen et al. Evidence for a Mass Dependent Forward-Backward Asymmetry in Top Quark Pair Production. *Phys. Rev.*, D83:112003, 2011.

[5] Timo Antero Aaltonen et al. Measurement of the forward?backward asymmetry of top-quark and antiquark pairs using the full CDF Run II data set. *Phys. Rev.*, D93(11):112005, 2016.

[6] Timo Antero Aaltonen et al. Combined Forward-Backward Asymmetry Measurements in Top-Antitop Quark Production at the Tevatron. *Submitted to: Phys. Rev. Lett.*, 2017.

[7] Victor Mukhamedovich Abazov et al. Forward-backward asymmetry in top quark-antiquark production. *Phys. Rev.*, D84:112005, 2011.

[8] Victor Mukhamedovich Abazov et al. Measurement of the forward-backward asymmetry in top quark-antiquark production in ppbar collisions using the lepton+jets channel. *Phys. Rev.*, D90:072011, 2014.

[9] J. A. Aguilar-Saavedra, W. Bernreuther, and Z. G. Si. Collider-independent top quark forward-backward asymmetries: standard model predictions. *Phys. Rev.*, D86:115020, 2012.

[10] Simone Alioli, Paolo Nason, Carlo Oleari, and Emanuele Re. A general framework for implementing NLO calculations in shower Monte Carlo programs: the POWHEG BOX. *JHEP*, 06:043, 2010.

[11] J. Alwall, R. Frederix, S. Frixione, V. Hirschi, F. Maltoni, O. Mattelaer, H. S. Shao, T. Stelzer, P. Torrielli, and M. Zaro. The automated computation of tree-level and next-to-leading order differential cross sections, and their matching to parton shower simulations. *JHEP*, 07:079, 2014.

[12] Johan Alwall, Michel Herquet, Fabio Maltoni, Olivier Mattelaer, and Tim

Stelzer. Madgraph 5: going beyond. *Journal of High Energy Physics*, 2011(6):128, Jun 2011.

[13] G. L. Bayatian et al. CMS physics: Technical design report. 2006.

[14] Werner Bernreuther and Zong-Guo Si. Top quark and leptonic charge asymmetries for the Tevatron and LHC. *Phys. Rev.*, D86:034026, 2012.

[15] Oliver Sim BrÃijning, Paul Collier, P Lebrun, Stephen Myers, Ranko Ostojic, John Poole, and Paul Proudlock. *LHC Design Report*. CERN Yellow Reports: Monographs. CERN, Geneva, 2004.

[16] Matteo Cacciari, Gavin P. Salam, and Gregory Soyez. The Anti-k(t) jet clustering algorithm. *JHEP*, 04:063, 2008.

[17] Qing-Hong Cao, David McKeen, Jonathan L. Rosner, Gabe Shaughnessy, and Carlos E. M. Wagner. Forward-Backward Asymmetry of Top Quark Pair Production. *Phys. Rev.*, D81:114004, 2010.

[18] Serguei Chatrchyan et al. Performance of CMS muon reconstruction in *pp* collision events at $\sqrt{s} = 7$ TeV. *JINST*, 7:P10002, 2012.

[19] Serguei Chatrchyan et al. Description and performance of track and primary-vertex reconstruction with the CMS tracker. *JINST*, 9(10):P10009, 2014.

[20] CMS. TOP Reference Selections and Recommendations (Run1).

[21] CMS. Electron Efficiency Measurement for Top Quark Physics at $\sqrt{s} = 8$ TeV. *CMS AN -2012/429.*, 2012.

[22] The CMS collaboration. Determination of jet energy calibration and transverse momentum resolution in cms. *Journal of Instrumentation*, 6(11):P11002, 2011.

[23] The CMS collaboration. Alignment of the cms tracker with lhc and cosmic ray data. *Journal of Instrumentation*, 9(06):P06009, 2014.

[24] John C. Collins and Davison E. Soper. Angular Distribution of Dileptons in High-Energy Hadron Collisions. *Phys. Rev.*, D16:2219, 1977.

[25] Michal Czakon, Paul Fiedler, and Alexander Mitov. Resolving the Tevatron Top Quark Forward-Backward Asymmetry Puzzle: Fully Differential Next-to-Next-to-Leading-Order Calculation. *Phys. Rev. Lett.*, 115(5):052001, 2015.

[26] Carsten Burgard David Galbraith. *ux-standard-model-of-the-standard-model.*

[27] Sayipjamal Dulat, Tie-Jiun Hou, Jun Gao, Marco Guzzi, Joey Huston, Pavel Nadolsky, Jon Pumplin, Carl Schmidt, Daniel Stump, and C. P. Yuan. New parton distribution functions from a global analysis of quantum chromodynamics. *Phys. Rev.*, D93(3):033006, 2016.

[28] Stefano Frixione and Bryan R. Webber. Matching nlo qcd computations and parton shower simulations. *Journal of High Energy Physics*, 2002(06):029, 2002.

[29] Martin Goerner and Peter Schleper. Differential Cross Sections for Top-Quark-Pair Production in the e/μ+Jets Final State at $\sqrt{s} = 8$ TeV in CMS, 2014.

[30] Moira I. Gresham, Ian-Woo Kim, and Kathryn M. Zurek. On Models of New Physics for the Tevatron Top A_{FB}. *Phys. Rev.*, D83:114027, 2011.

[31] David J Griffiths. *Introduction to elementary particles; 2nd rev. version*. Physics textbook. Wiley, New York, NY, 2008.

[32] Ulrich Husemann. Top-Quark Physics: Status and Prospects. *Prog. Part. Nucl. Phys.*, 95:48–97, 2017.

[33] Vardan Khachatryan et al. Inclusive and differential measurements of the $t\bar{t}$ charge asymmetry in pp collisions at $\sqrt{s} = 8$ TeV. *Phys. Lett.*, B757:154–179, 2016.

[34] Vardan Khachatryan et al. Jet energy scale and resolution in the CMS experiment in pp collisions at 8 TeV. *JINST*, 12(02):P02014, 2017.

[35] Nikolaos Kidonakis. NNLL threshold resummation for top-pair and single-top production. *Phys. Part. Nucl.*, 45(4):714–722, 2014.

[36] Henning Kirschenmann. Jets at cms and the determination of their energy scale. 2012.

[37] Kevin Kröninger, Andreas B. Meyer, and Peter Uwer. Top-Quark Physics at

the LHC. In Thomas Schörner-Sadenius, editor, *The Large Hadron Collider: Harvest of Run 1*, pages 259–300. 2015.

[38] Johann H. Kuhn and German Rodrigo. Charge asymmetry of heavy quarks at hadron colliders. *Phys. Rev.*, D59:054017, 1999.

[39] Johann H. Kuhn and German Rodrigo. Charge asymmetries of top quarks at hadron colliders revisited. *JHEP*, 01:063, 2012.

[40] Kevin Lannon, Fabrizio Margaroli, and Chris Neu. Measurements of the Production, Decay and Properties of the Top Quark: A Review. *Eur. Phys. J.*, C72:2120, 2012.

[41] Yurii Maravin Lovedeep Kaur Saini, Ilya Kravchenko. A study of efficiencies and scale factors for cut-based electron identification at CMS experiment using data from proton-proton collisions at $\sqrt{s}$ =8 TeV. . *CMS AN-2014/055*, 2014.

[42] Thomas Müller, Jochen Ott, and Jeannine Wagner-Kuhr. Theta : A framework for template based modelling and inference. *CMS-IN 2010-17*, 2010.

[43] Lei Feng Nick Eminizer and Morris Swartz. Template measurement of the $t\bar{t}$ forward-backward asymmetry AFB and anomalous chromoelectric and chromomagnetic moments in the semileptonic channel at $\sqrt{s} = 13$ TeV. *CMS-AN-2017-123*, 2017.

[44] K. A. Olive et al. Review of Particle Physics. *Chin. Phys.*, C38:090001, 2014.

[45] Michael E. Peskin and Daniel V. Schroeder. *An Introduction to quantum field theory*. Addison-Wesley, Reading, USA, 1995.

[46] Tilman Plehn. Lectures on LHC Physics. *Lect. Notes Phys.*, 844:1–193, 2012.

[47] Michael Russell. *Top quark physics in the Large Hadron Collider era*. PhD thesis, Glasgow U., 2017.

[48] TorbjÃűrn SjÃűstrand, Stephen Mrenna, and Peter Skands. Pythia 6.4 physics and manual. *Journal of High Energy Physics*, 2006(05):026, 2006.

[49] C. Weiser. A Combined Secondary Vertex Based B-Tagging Algorithm in CMS. *CMS internal analysis note*, 2006.

Vita

Education

- Ph.D., Experimental High Energy Physics, Johns Hopkins University, Baltimore, MD, January 2018
- B.Sc., Physics (SYSU - ENS Pairs special program), Sun Yat-sen University, Guangzhou, China, June 2011

Work Experience

- Research Assistant, Department of Physcis and Astronomy, Johns Hopkins University, September 2014 - November 2017
- Teaching Assistant, Department of Physcis and Astronomy, Johns Hopkins University, September 2011 - June 2014

Conferences and Workshops

- APS Division of Particle and Fields Meeting, Fermilab, Chicago, Poster Presentation, August 2017
- APS April Meeting, Presentation, Washington DC, January 2017
- CMS Data Analysis School, Workshops, Fermilab, January 2015

Publications

- "Measuring the $t\bar{t}$ forward-backward asymmetry using semi-leptonic final states at 8 TeV with the CMS detector", The CMS Collaboration, CMS internal preprint CMS-AN-2017-275